COMPUTATIONAL EXPLORATION OF THERMODYNAMIC PROPERTIES OF POROUS AND LAYERED MATERIALS

A Dissertation
Presented to
The Academic Faculty

by

Hakan Demir

In Partial Fulfillment
of the Requirements for the Degree
Doctor of Philosophy in the
School of Chemical and Biomolecular Engineering

Georgia Institute of Technology
August 2016

COMPUTATIONAL EXPLORATION OF THERMODYNAMIC PROPERTIES OF POROUS AND LAYERED MATERIALS

Approved by:

Dr. David S. Sholl, Advisor
School of Chemical and Biomolecular Engineering
Georgia Institute of Technology

Dr. William J. Koros
School of Chemical and Biomolecular Engineering
Georgia Institute of Technology

Dr. Krista S. Walton
School of Chemical and Biomolecular Engineering
Georgia Institute of Technology

Dr. Seung Soon Jang
School of Materials Science and Engineering
Georgia Institute of Technology

Dr. Christopher W. Jones
School of Chemical and Biomolecular Engineering
Georgia Institute of Technology

Date Approved: May 17, 2016

To my family

ACKNOWLEDGEMENTS

Firstly, I would like to thank my advisor Dr. David S. Sholl for his guidance about my scientific and personal development. I appreciate not only his efforts to persuade me towards improving my research and skills but also the time he allocated to me whenever I asked for, even during the times he had very little time. I can confidently say that he has been a great role model for me both in terms of scientific excellence and good character. Over the past years, I have felt very happy and also lucky to work with a real intellectual and gentleman as David. I hope I can convey the things I have learned from him to the people I would be working with in the future.

I would also like to express my gratitude to Dr. Jeffery A. Greathouse, Dr. Krista S. Walton, Dr. Panchapakesan Ganesh, Dr. Marie V. Parkes, Dr. Stephanie L. Teich-McGoldrick, Dr. Mark D. Allendorf, Dr. Chad L. Staiger, Dr. John J. Perry IV, Dr. Michael A. Susner, Dr. Alex Belianinov, Dr. Albina Borisevich, Dr. Qian He, Dr. Marius Chyasnavichyus, Dr. Douglas L. Abernathy, Dr. Michael A. McGuire and Dr. Petro Maksymovych for their valuable suggestions and collaboration in the projects I have worked on. I appreciate the fundings from Sandia National Laboratories, TDA Research and Oak Ridge National Laboratory which have made this PhD work possible. I am also thankful to Dr. Christopher W. Jones, Dr. William J. Koros, Dr. Seung Soon Jang and Dr. Krista S. Walton for providing their insights and comments as my PhD committee members.

Since the first moment I spent in my research group, I have always felt comfortable in the group and this is obviously because of the friendly atmosphere created by all group

members. Therefore, I would like to thank former and current group members Dr. Hanjun Fang, Dr. Taku Watanabe, Dr. Melissa J. Lucero, Dr. Jason Gee, Dr. Ambarish Kulkarni, Dr. Rohan Awati, Dr. Emmanuel Haldoupis, Dr. Daniel Wei, Dr. Kelly Nicholson, Dr. Nita Chandrasekhar, Dr. Dieh Teng, Dr. Liwei Li, Dr. Sung Gu Kang, Dr. Mohamad Kassaee, Dr. Salah Boulfelfel, Dr. Xiaowa Nie, Dr. Rongshun Zhu, Dr. Veronika Walkosz, Dr. Xuerong Shi, Dr. Ji Zang, Dr. Thomas Manz, Dr. Joshua D. Howe, Timothy van Heest, Seung Won Choi, Ben Chun, Jeffrey Camp, Dalar Nazarian, Ross Verploegh, Ken Onubogu, Jaeyub Chung, Namory Keita, Jongwoo Park, Ying Wu, Omar Knio, Wenqin You, Yang Lui, Rebecca Han, Mayank Agrawal, Chu Han, John Findley, Krishna Jayachandrababu, Brandon Plaisance, Jungseob So, Lalit Darunte, Souryadeep Bhattacharyya, and Dr. Dai Tang for creating such an environment.

Last but not least, I would like to thank my family for supporting me throughout my entire life. Without their continuous support and love, I would have not been able to pursue or complete my PhD.

Hakan Demir, April 2016

TABLE OF CONTENTS

LIST OF TABLES

LIST OF FIGURES

NOMENCLATURE

DFT	Density-Functional Theory
GCMC	Grand-Canonical Monte Carlo
MOF	Metal-organic framework
PCP	Porous coordination polymer
PCN	Porous coordination network
FF	Force field
CSD	Cambridge Structural Database
CoRE	Computation Ready, Experimental
P_s	Spontaneous electric polarization
E	External electric field
LDA	Local density approximation
GGA	Generalized gradient approximation
PW91	Perdew-Wang
PBE	Perdew-Burke-Ernzerhof
VASP	Vienna Ab Initio Simulation Package
PAW	Projector augmented wave
MP2	Møller−Plesset
vdW	Van der Waals
LJ	Lennard-Jones
PUC	Periodic unit cell
BDC	Benzene dicarboxylate
IAST	Ideal Adsorbed Solution Theory

NEMO	Non-empirical model potential
SAPT	Symmetry-Adapted Perturbation Theory
DDEC	Density-derived electrostatic and chemical
MUSIC	Multipurpose simulation code
MD	Mean deviation
MAD	Mean absolute deviation
RDF	Radial distribution functions
BSSE	Basis set superposition error
LCD	Largest cavity diameter
PLD	Pore limiting diameter
ICSD	Inorganic crystal structure database
TPS	Transition metal thio/selenophosphate
DOS	Density of states
T_s	Spinodal decomposition temperature
PFM	Piezoresponse Force Microscopy
EDS	Energy-dispersive X-ray spectroscopy

SUMMARY

Noble gases are relatively rare gases, however, they have been used in many areas. Currently, separation of noble gases are achieved by fractional distillation at cryogenic temperatures and materials that can separate them around room temperature are investigated. One of the promising class of materials is metal-organic frameworks due to their high surface area, pore volume and tunability. In this thesis, ab-initio based force fields were developed for Ar and Xe adsorption in six different MOFs to predict adsorption properties and compare this non-empirical approach to the experimental results and generic force field (FF) simulations. Using three DFT functionals (PBE-D2, vdW-DF, and vdW-DF2) in periodic models of M-MOF-74 (M= Co, Ni, Zn, Mg), ZIF-8 and Cu-BTC, first principles based FFs are derived. Selective separation of contaminants from ambient air is another crucial field since some of those contaminants can be detrimental to health. In this thesis, a water-stable MOF, UiO-66, is computationally functionalized with more than 30 functional groups using cluster and periodic systems and binding energies of NH_3, H_2S, CO_2 and H_2O are calculated to rank the functionalized UiO-66 materials for selective separation of contaminants in humid air conditions. Finally, the phase stability and transitions of 2-D layered ferroelectric materials, $CuInP_2Q_6$ (Q=S, Se), are investigated. The phase transition of $CuInP_2Se_6$ is studied using DFT calculations and phonon theory to identify instabilities at zone center and boundaries of the structure while possible spinodal decomposition regions of $Cu_xIn_yP_2S_6$ are determined with respect to Cu concentration by combining DFT calculations with thermodynamic relations.

CHAPTER 1

INTRODUCTION

This work involves computational approaches and calculations focusing on porous and layered materials. In the next sections, an overview of these materials is presented.

1.1 Nanoporous Materials

Porous materials have been crucial for the applications of gas storage/separation, catalysis, sensing etc. due to their high surface area and volume. According to IUPAC, they can be classified as in Table 1.[1]

Table 1. Porous Materials Classification.

Classification	**Pore Size (nm)**
Macroporous	Pore Size > 50
Mesoporous	2 < Pore Size < 50
Microporous	Pore Size < 2

In the literature, the word "nanoporous" may involve both microporous and mesoporous materials. The existence of micropores in a structure can lead to very high surface areas (more than 1000 m^2/g). Micropores are the main reason for the adsorption at lower pressures.[1] Another way of classifying porous materials relies on the ordered or disordered structure of the material giving amorphous and crystalline class of materials.[2] Amorphous materials do not possess an ordered crystal structure, thus uniform pore sizes, however they

can have a wide range of pore sizes.[1] On the other hand, crystalline materials have ordered structure making both atomistic modeling and molecular sieving easier.[3] One class of nanoporous, crystalline materials is metal-organic frameworks (MOFs) which has become an important subject for both experimental and computational research groups especially after the 1990's.[4] A general overview of MOFs is described in the next section.

1.2 Metal-Organic Frameworks

MOFs are nanoporous crystalline materials comprised of metal ligand complexes connected to organic linkers through coordination bonds. The presence of strong coordination bonds results in well-ordered structures.[5] MOFs generally possess high surface area (beyond 6000 m^2/g), tunable, high porosity and decent structural stability.[6, 7] One example MOF structure is shown in Figure 1, where the Co-MOF-74 structure is depicted oriented along its pore channels.

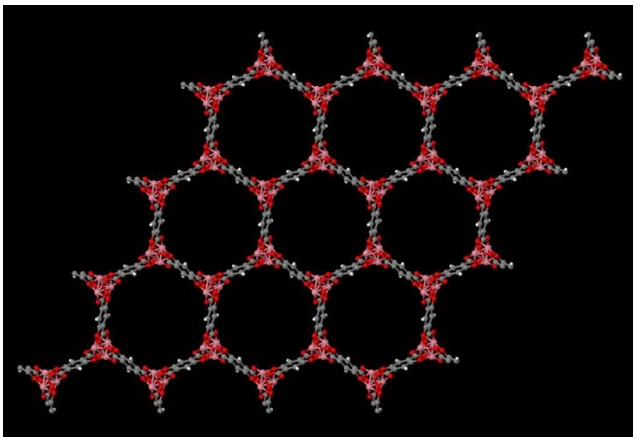

Figure 1. Periodic structure of Co-MOF-74 along *c* axis. (Oxygen, cobalt, carbon, and hydrogen are shown in red, pink, gray, and white, respectively.).

In the literature, MOFs can also be referred as porous coordination polymer (PCP) or porous coordination network (PCN) since during early work on these materials there was no commonly accepted definition.[8] One of the intriguing properties of the MOFs that deserves investigation is the possible open-metal sites (coordinately unsaturated metal sites) in the structure. Open metal sites can be formed during the synthesis procedure when the metal-bound water molecules are removed from the structures by heating the sample. They are able to interact with adsorbate molecules strongly which can have big effect on MOF applications.[9] Several instances of MOFs having open metal sites are MOF-74[10], Cu-BTC[11], and MIL-101[12].

The number of possible MOFs is theoretically almost infinity since there are many different metals and organic linkers that can be combined.[6] Such combinations can adjust pore size, pore connectivity, gas affinities etc.[13-17] Since MOFs have a very wide structural and chemical diversity, they are promising candidates for sensing[18], drug delivery[19], catalysis[20] etc. There have been many MOF studies specifically focusing on methane, hydrogen, carbon dioxide, and noble gas adsorption and separation. [21-25]

Currently, there are more than 7000 MOFs synthesized[26] and more than 100,000 hypothetical MOFs[27]. There are crystal structure databases such as Cambridge Structural Database (CSD)[28] and Computation Ready, Experimental (CoRE)[29] MOF database which have been used to screen materials for different purposes such as light gas, noble gas separation.[30-33] Since it is not feasible to perform experiments for thousands of structures, computational approaches are crucial to investigate adsorption and structural properties to guide experimental efforts.

1.3 Ferroic Materials

Ferroic is a generic term used to describe properties such as ferroelectricity, ferromagnetism, and ferroelasticity, which are characterized by electric (polarization-electric field), magnetic (magnetization-magnetic field) and elastic (strain-stress) hysteresis, respectively, where structural properties change below a critical phase transition temperature.[34, 35] Ferroic structures have symmetries that are subgroups of a parent structure since they are formed by small deviations from the parent structure.[36]

Ferroelectric materials are insulating solids having a spontaneous electric polarization (P_s) in the absence of an external electric field (E) below the critical Curie temperature.[37, 38] They are formed through the displacement of ions from their centrosymmetric positions creating a net dipole moment and spontaneous polarization in the unit cell.[39] The dipoles create ferroelectric domains that may have sizes in the order of nanometers to millimeters.[40] An important feature of ferroelectric materials is the ability to switch between two or more ferroelectric states with the application of an external electric field.[37] The critical electric field to switch the polarization is defined as coercive field.[41] Ferroelectric materials go through spontaneous symmetry breaking and have multistable equilibrium states. At high temperature, the material becomes paraelectric[42] (P_s =0) and the multistability disappears.[38, 39] Landau-Devonshire theory describes the phase switching of ferroelectrics by expressing the free energy difference between the two phases involved as a function of polarization (P)

$$\Delta G = \frac{1}{2}\alpha P^2 + \frac{1}{4}\xi P^4 + \frac{1}{6}\zeta P^6 \tag{1.1}$$

where α, ξ, and ζ denote phenomenological coefficients.[43]

Ferroelectricity was first discovered in Rochelle salt in 1921 and subsequently in KH_2PO_4 in 1935. Around that time, it was thought that ferroelectricity was correlated with hydrogen bonding. However, in 1944, ferroelectricity in $BaTiO_3$ was observed proving this opinion wrong. This was an important finding which led to other ferroelectricity studies in perovskite type systems.[44] In addition, $BaTiO_3$ was the first ferroelectric material having multiple ferroelectric phases. It also showed chemical and mechanical stability together with ferroelectricity at room temperature. In the subsequent years, more ferroelectrics such as $KNbO_3$, $KTaO_3$, $LiNbO_3$, $LiTaO_3$, and $PbTiO_3$ etc. were synthesized.[45] Currently, there are more than 700 ferroelectric materials, most of which do not have hydrogen bonding or oxides, for instance GeTe, $SrAlF_5$, SbSI etc.[46]

Ferroelectrics are a subclass of pyroelectrics, which belong to piezoelectric materials. Pyroelectrics are the materials where a temperature change induces an electric charge while in piezoelectrics an applied stress creates an electric potential.[47] While all ferroelectric materials are pyroelectric and all pyroelectric materials are piezoelectric, the opposite does not hold.[46] For instance, quartz has piezoelectricity but not pyroelectricity while AlN, GaN, and ZnO possess both piezoelectricity and pyroelectricity but not ferroelectricity.[47] Another group of materials having ferroelectric properties is ferrielectrics, which have antiferroelectricity along one axis and ferroelectricity along another axis at a given temperature.[48]

In crystallography, out of 32 point groups, 21 are noncentrosymmetric classes lacking spatial-inversion symmetry. 20 of those noncentrosymmetric groups possess piezoelectricity while 10 out of those 20 classes exhibit both piezoelectricity and

pyroelectricity. A subgroup of the latter 10 classes can also have ferroelectricity if the polarization is switchable.[49, 50]

Switchable spontaneous polarization enables ferroelectric materials to be used as non-volatile memory where information can be stored and retained during power interruption.[51] This means electronic devices will not have to be booted up after each time they are shut down. Moreover, ferroelectric random access memories possess fast write speed, high read/write cycle stability and low-power consumption which make them promising candidates for storing data.[52] However, one drawback of them is their low storage density compared to another type of non-volatile memory, i.e. flash memory.[53] Ferroelectric materials have also been used as capacitors, piezoelectric transducers, actuators, and pyroelectric sensors.[54-57]

The term antiferroelectricity was introduced in 1951 which is defined as a state where chains of atoms are spontaneously polarized in a particular direction and neighboring chain of atoms are polarized in the antiparallel direction. Thus, the structure does not possess a spontaneous macroscopic polarization. However, when it is exposed to electric field, the antiparallel dipoles can be re-aligned as parallel leading to an electric field-induced antiferroelectric-ferroelectric phase transition. This phenomenon causes double-hysteresis loops in the relation of electric field with respect to electric polarization. Together with the drastic change in polarization, several other properties, namely linear dimensions and optical properties, also alter significantly.[58] Antiferroelectrics can be classified into different groups such as perovskite, pyrocholore, liquid crystal etc.[43] Examples of antiferroelectric materials are $PbZrO_3$[59], $PbHfO_3$[60], $NaNbO_3$[61], and

$NH_4H_2PO_4$[62] etc. Antiferroelectric materials can be used for various purposes including high-energy capacitors, cooling devices, high-strain actuators, and pyroelectric detectors.[43]

1.4 Thesis Summary

The main aims of this work are developing and applying computational approaches to predict adsorption properties of various metal-organic frameworks and determining phase stabilities/instabilities of $CuInP_2Q_6$ (Q=S, Se) materials using different computational methodologies. In Chapter 2, various computational methods that are used in the subsequent chapters are introduced. In Chapter 3, ab-initio based force field development for noble gas adsorption in metal-organic frameworks is described together with their prediction performances compared to experiments and a generic force field, UFF. A combination of classical and quantum mechanical approaches is used to derive force fields. We derive a force field development algorithm and apply it to develop Lennard-Jones type classical force fields which are comprised of dispersion and polarization effects. The applied methodology provides insights into the prediction powers of PBE-D2, vdW-DF and vdW-DF2 based force fields for noble gas adsorption in M-MOF-74 (M=Co, Ni, Zn, Mg), ZIF-8 and Cu-BTC.

In Chapter 4, the study of selective adsorption of air contaminants in humid conditions using functionalized metal-organic frameworks is discussed using different DFT functionals and the more accurate MP2 level of theory calculations. First, we start with the calculations for the cluster models. Then, comparisons of DFT functionals with MP2 calculations in cluster systems are obtained to decide on the DFT functional to be used in periodic systems. We show the effect of incorporation of functional groups into UiO-66 framework on adsorption affinities of NH_3, H_2S, CO_2 and H_2O using both cluster

and periodic models. We rank the relative adsorption affinities of NH_3, H_2S, CO_2 over H_2O in clusters and periodic systems to show the effect of confinement on material rankings.

In Chapter 5, the subject of the study moves from porous materials to ferroic materials. We use DFT level calculations and thermodynamic relations to determine the phase stability/instability regions of $Cu_xIn_yP_2S_6$, having excess Cu, over the copper concentration range. Our approach determines the copper concentration range where a spinodal decomposition is thermodynamically favorable. By combining DFT data with the phonon theory, we also show the instability of centrosymmetric $CuInP_2Se_6$ structure, the motions causing the instability and the pathway to obtain a stable structure. We also discuss the effect of possible disorders in the structure on vibrational DOS plots and compare them with the experimental neutron DOS. Lastly, the effect of increased layer gap on the stability of the structure is shown with energy profiles.

In Chapter 6, we discuss the key conclusions, possible opportunities and challenges in the area of atomistic simulations of metal-organic framework and ferroelectric materials.

CHAPTER 2

COMPUTATIONAL METHODOLOGY

In this chapter, we briefly describe the theoretical approaches used in the projects namely quantum mechanical, classical simulation methods and phonon theory. Firstly, we summarize the quantum mechanical approach, Density Functional Theory (DFT), used to obtain first principles based properties of materials. Then, we describe the Grand Canonical Monte Carlo (GCMC) method used to predict adsorption characteristics of an adsorbate in an adsorbent. Finally, phonon theory is reviewed introducing some of the concepts used in phase transitions of ferroelectric materials.

2.1 Density Functional Theory

DFT is a commonly used quantum mechanical method that describes interactions between electrons determining structural properties.[63] There are many resources introducing DFT and elaborating on its details.[64-69] In this section, a general overview of DFT method and DFT functionals is given.

The roots of DFT go back to 1920's when Erwin Schrödinger introduced Schrödinger equation which is the foundation of quantum chemical calculations.[70] The Schrödinger equation can be solved exactly for simple problems namely particles in a box, harmonic oscillator etc. However, the situation gets more challenging as systems get more complex where many electrons interact with many nuclei. For such systems, starting from the time-independent Schrödinger equation, $H\psi = E\psi$, the equation can be written as

$$\left[-\frac{\hbar^2}{2m}\sum_{i=1}^{N}\nabla_i^2+\sum_{i=1}^{N}V(\boldsymbol{r}_i)+\sum_{i=1}^{N}\sum_{j<i}U(\boldsymbol{r}_i,\boldsymbol{r}_j)\right]\psi=E\psi \tag{2.1}$$

where m denotes electron mass. The terms in the square brackets represent kinetic energy of electron i, the interaction energy between electron i and the ensemble of atomic nuclei, and the interaction energy between electrons, respectively. Although the electron wave function ψ can be approximated as the product of individual wave functions of N electrons, $\psi_i(r)$, the challenging part of solving this problem is the fact that an individual electron wave function cannot be obtained without considering others as well. Therefore, approximations should be made to be able to solve this equation for many-body problems.[71]

DFT relies on two theorems which are established in 1960's. The first theorem, which was established by Hohenberg and Kohn, postulates that the ground state energy is a unique functional of the electron density. This means the Schrödinger equation can be solved by determining a function with three variables (i.e. x, y, z), electron density, which is much easier than using wave functions with 3N variables, N being number of electrons. The second theorem states that the true electron density is the one minimizing the energy of the overall functional. The true electron density could be found by varying it until the energy of the true functional is minimized. However, the true functional is unknown which made Kohn and Sham to convert the Schrödinger equation into a set of equations, the Kohn-Sham equations, describing interactions of single electrons as

$$\left[-\frac{\hbar^2}{2m}\nabla^2+V(r)+V_H(r)+V_{XC}(r)\right]\psi_i(r)=\varepsilon_i(r)\psi_i(r) \tag{2.2}$$

where $V(r)$, $V_H(r)$, and $V_{XC}(r)$ denote the electron-nuclei interaction potential, Hartree potential, and exchange-correlation contribution, respectively. Still, V_{XC} is unknown and should be approximated. Mainly, there are two ways of approximating it, local density

approximation (LDA) and generalized gradient approximation (GGA). LDA utilizes solely the local electron density to determine the unknown exchange-correlation functional. GGA approach involves more information, the local electron density and the local electron density gradient, to define the exchange-correlation functional. It should be noted that although LDA includes less information, it does not mean that it always gives less accurate results compared to GGA. There are different approaches of incorporating information from electron density gradient and thus, there are many different GGA functionals derived. Among those, Perdew-Wang functional (PW91)[72] and Perdew-Burke-Ernzerhof (PBE)[73] are the two most commonly used ones.[71] One of the shortcomings of standard DFT functionals is they do not describe the long-range dispersion energies.[74, 75]

To account for the long-range dispersion interactions, dispersion corrected DFT functionals such as semi-empirically corrected DFT-D2[76] and nonempirically corrected vdW-DF[77] and vdW-DF2[78] functionals have been proposed. For DFT-D2, Grimme et al. proposed an empirical dispersion correction term added to Kohn-Sham energy

$$E_{DFT-D} = E_{KS-DFT} + E_{disp} \tag{2.3}$$

The dispersion term is expressed as

$$E_{disp} = -s_6 \sum_{i=1}^{N_{at}-1} \sum_{j=i+1}^{N_{at}} \frac{C_6^{ij}}{R_{ij}^6} f_{dmp}(R_{ij}) \tag{2.4}$$

where s_6, N_{at}, C_6^{ij}, R_{ij} and f_{dmp} represent global scaling factor, number of atoms in the system, dispersion coefficient for atomic pair i-j, interatomic distance between atoms i and j and a damping function for small atomic distances, respectively. The dispersion coefficient, C_6^{ij}, can be determined using

$$C_6^{ij} = \sqrt{C_6^i C_6^j} \tag{2.5}$$

where C_6^i and C_6^j are C_6 parameters for individual atoms i and j.

For the vdW-DF methods, the correlation energy is separated into local and nonlocal energies and the total exchange-correlation energy is defined as

$$E_{xc} = {E_x}^{GGA} + E_c^0 + E_c^{nl} \tag{2.6}$$

where ${E_x}^{GGA}$, E_c^0, and E_c^{nl} represent GGA exchange energy, local and nonlocal correlation energies, respectively. Here, E_c^0 is treated with LDA and E_c^{nl} corresponds to the long-ranged electron correlation effects giving rise to van der Waals interactions. The only difference between vdW-DF variants is exchange energy. In vdW-DF and vdW-DF2 methods, revPBE[79] and PW86[80, 81] exchange functionals are used, respectively.

Besides GGA type functionals, a hybrid meta-GGA functional, M06-2X, is also used in this thesis for cluster calculations. M06-2X is a member of M06 functional family with 54% Hartree-Fock exchange involving medium-range dispersion effects.[82, 83] It has been mainly suggested for main-group thermochemistry and noncovalent interactions. The full details about its derivation can be found in Zhao et al's work.[83]

In this dissertation, all plane wave DFT calculations are done by *Vienna Ab Initio Simulation Package* (VASP)[84-86]. The projector augmented wave (PAW) method[87, 88] is used to describe the interactions between core and valence electrons. Cluster calculations are done using GAUSSIAN 09.[89] More calculations details can be found in the respective chapters.

2.2 Second-Order Møller−Plesset (MP2) perturbation theory

MP2[90] is a wave-function based quantum chemical method beyond Hartree-Fock theory that can approximate all van der Waals (vdW) interactions namely electrostatics, dispersion, and induction effects.[91] Prior to the introduction of DFT, it was computationally the least expensive way to consider electron correlation effects in electronic structure calculations. Still, it is more advantageous than DFT for cases where dispersion interactions and charge-transfer are crucial.[92] However, it has been reported that MP2 can overestimate dispersion effects.[91, 93] There have been efforts to improve the accuracy of standard MP2 theory by incorporation of dispersion corrections, spin scaling, orbital optimization, and explicit correlation which are summarized elsewhere.[94]

One other disadvantage of standard MP2 theory is it is computationally applicable for systems having up to 100 valence electrons beyond which is possible if there is high molecular point group symmetry.[95] There are different approaches to lower the computational cost of standard MP2 theory which are described elsewhere.[94] In this thesis, standard MP2 theory is used.

2.3 Grand Canonical Monte Carlo

The atomistic simulation method used to describe adsorption properties of an adsorbate in a material is Grand Canonical Monte Carlo (GCMC) which mimics an experimental adsorption study where a bulk gas is equilibrated with adsorbed gas in the adsorbent. In the grand canonical ensemble (μ, V, and T ensemble), the temperature, volume, and chemical potential are constant. At the equilibrium conditions, the adsorbed and bulk phase have equal chemical potentials. The pressure in the bulk gas reservoir is related to the chemical potential of adsorbed phase and can be obtained from an equation

of state.[96] As long as the temperature and chemical potential of the bulk gas are known, the equilibrium adsorbate loading in the material can be found. In a typical GCMC simulation, there are three kinds of moves, thermal equilibration, insertion and deletion. The thermal equilibration move can be translation and/or rotation for a rigid adsorbate molecule while for nonrigid molecules it also involves change in intramolecular degrees of freedom. In the insertion move, a molecule is inserted at a random site in the adsorbent with a random orientation. In the deletion move, a randomly chosen molecule is removed.[96] For rigid molecules, the total potential energy of the system is comprised of intermolecular (nonbonded) interactions only which are generally expressed with a Lennard-Jones (LJ) 12-6 potential

$$U(r_{ij}) = 4\varepsilon_{ij}\left[\left(\frac{\sigma_{ij}}{r_{ij}}\right)^{12} - \left(\frac{\sigma_{ij}}{r_{ij}}\right)^{6}\right] \tag{2.7}$$

where r_{ij}, ε_{ij}, and σ_{ij} denote separation distance, well depth, LJ size for the atom pairs i and j, respectively. Generally, the unlike-pair interactions are defined by Lorentz-Berthelot combining rules[97]

$$\sigma_{ij} = (\sigma_{ii} + \sigma_{jj})/2 \tag{2.8}$$

$$\varepsilon_{ij} = \sqrt{\varepsilon_{ii}\varepsilon_{jj}} \tag{2.9}$$

Practically, in the GCMC simulations, the number of adsorbed gas molecules per unit cell of the adsorbent is calculated at a specific temperature and pressure. One difference between the output of a real adsorption experiment and a GCMC simulation is that in the experiments, the quantity measured is amount of excess adsorbed gas molecules while in a GCMC simulation the quantity calculated is the absolute amount of adsorbed gas molecules. The relation between these two quantities are as follows[24]

$$N_{total} = N_{excess} + \rho_{gas} V_p \tag{2.10}$$

where N_{total}, N_{excess}, ρ_{gas}, and V_p refer to absolute adsorbed amount of gas, excess adsorbed amount of gas, bulk gas density at simulation conditions and pore volume determined typically by helium insertion method, respectively. Helium void fractions can be calculated using Widom insertions of helium at room temperature. Beside the adsorbate loading, the other important quantity that can be calculated from a GCMC simulation is isosteric heat of adsorption, Q_{st}, using[24]

$$Q_{st} = RT - \frac{\langle NV \rangle - \langle N \rangle \langle V \rangle}{\langle N^2 \rangle - \langle N \rangle^2} \tag{2.11}$$

where R, T, $\langle\rangle$, N, and V correspond to gas constant, temperature, ensemble average, number of adsorbed gas molecules, and total potential energy of the adsorbed gas molecules. More details about GCMC including the statistical mechanical foundation of it is described in detail elsewhere.[98]

2.4 Phonon Theory[99]

Although atoms are considered to reside at particular sites in the lattice, at a finite temperature, the atoms vibrate around the equilibrium positions with a magnitude dependent on the temperature. Due to crystallographic symmetries, the thermal vibrations can be investigated as collective modes of ion motions. These modes can be considered as collective excitations which are similar to electronic states in terms of being excited and populated. These collective excitations are defined as phonons.

Mathematically, the phonons can be described by harmonic approximation. Assume that at zero temperature, the ion positions in the material are defined by the vectors

$$\boldsymbol{R}_{ni} = \boldsymbol{R}_n + \boldsymbol{t}_i \tag{2.12}$$

where $\boldsymbol{R}_n$, and $\boldsymbol{t}_i$ are Bravais lattice vectors, ion positions in one periodic unit cell (PUC) with the condition of $|\boldsymbol{t}_i| < |\boldsymbol{R}_n|$ for all non-zero lattice vectors. Here, *n* and *i* runs over all the PUCs of the crystal and all ions in the PUC, respectively. At finite temperature, the ionic deviation from zero temperature position can be defined

$$\boldsymbol{S}_{ni} = \delta \boldsymbol{R}_{ni} \tag{2.13}$$

The system's potential energy can be described with a Taylor series expansion in terms of $\boldsymbol{S}_{ni}$. The zeroth order term, being a constant, is taken to be zero for convenience, while the first order term is zero since the system is assumed to be in equilibrium at zero temperature. The only term involved in the potential energy expression is second order term since higher order terms are considered to be negligible. With this approximation, the potential energy V is

$$V = \frac{1}{2} \sum_{n,i,\alpha;m,j,\beta} \frac{\partial^2 E}{\partial R_{ni\alpha} \partial R_{mj\beta}} S_{ni\alpha} S_{mj\beta} \tag{2.14}$$

where total energy E relies on all the atomic coordinates $\boldsymbol{R}_{ni}$. The subscript α (or β) denotes the cartesian coordinates of $\boldsymbol{S}_{ni}$ (α = x, y, z in 3D). Definitions of m and j are the same as those of n and i, respectively. In this expression, the force-constant matrix is defined as

$$F_{ni\alpha,mj\beta} = \frac{\partial^2 E}{\partial R_{ni\alpha} \partial R_{mj\beta}} \tag{2.15}$$

which turns V into

$$V = \frac{1}{2} \sum_{n,i,\alpha;m,j,\beta} F_{ni\alpha,mj\beta} \, S_{ni\alpha} S_{mj\beta} \tag{2.16}$$

The force-constant matrix has a dimension size of d × ν × N where d, ν, and N represent the space dimensionality (the number of values for α), the number of ions in a PUC, and

the number of PUCs in the crystals, respectively. The following equality can be obtained from the definitions of the harmonic approximation of the potential energy and the force-constant matrix.

$$\frac{\partial^2 V}{\partial S_{ni\alpha}\partial S_{mj\beta}} = F_{ni\alpha,mj\beta} = \frac{\partial^2 E}{\partial R_{ni\alpha}\partial R_{mj\beta}} \tag{2.17}$$

Newton's third law implies

$$\frac{\partial V}{\partial S_{ni\alpha}} = \sum_{m,j,\beta} F_{ni\alpha,mj\beta}\, S_{mj\beta} = \frac{\partial E}{\partial R_{ni\alpha}} \tag{2.18}$$

where the leftmost term is the negative of the α component of the total force on ion i. The equation of motions for ions can be written as

$$M_i \frac{d^2 S_{ni\alpha}}{dt^2} = -\frac{\partial E}{\partial R_{ni\alpha}} = -\sum_{m,j,\beta} F_{ni\alpha,mj\beta}\, S_{mj\beta} \tag{2.19}$$

using Eq. (2.18). Assume the solution of the equation of motion is

$$S_{ni\alpha}(t) = \frac{1}{\sqrt{M_i}} \tilde{u}_{ni\alpha} e^{-i\omega t} \tag{2.20}$$

where ω represents oscillation frequency. Plugging Eq. (2.20) into Eq. (2.19) gives

$$\omega^2 \tilde{u}_{ni\alpha} = \sum_{m,j,\beta} F_{ni\alpha,mj\beta} \frac{1}{\sqrt{M_i M_j}} \tilde{u}_{mj\beta} \tag{2.21}$$

A portion of this expression can be defined as the dynamical matrix

$$\widetilde{D}_{ni\alpha,mj\beta} = \frac{1}{\sqrt{M_i M_j}} F_{ni\alpha,mj\beta} \tag{2.22}$$

Thus, the equation of motion becomes the following eigenvalue equation

$$\sum_{m,j,\beta} \widetilde{D}_{ni\alpha,mj\beta}\, \tilde{u}_{mj\beta} = \omega^2 \tilde{u}_{ni\alpha} \tag{2.23}$$

$$\widetilde{\boldsymbol{D}} \cdot \tilde{\boldsymbol{u}} = \omega^2 \tilde{\boldsymbol{u}} \tag{2.24}$$

By solving this eigenvalue equation, the frequency and ionic displacement vectors can be obtained. However, since the dynamical matrix has the same dimension size as the force-constant matrix, d × ν × N, it is not possible to diagonalize the matrix when N → ∞. Recalling the dynamical matrix definition

$$\widetilde{D}_{ni\alpha,mj\beta} = \frac{1}{\sqrt{M_i M_j}} F_{ni\alpha,mj\beta} = \frac{1}{\sqrt{M_i M_j}} \frac{\partial^2 E}{\partial R_{ni\alpha} \partial R_{mj\beta}} \tag{2.25}$$

If both $R_{ni\alpha}$ and $R_{mj\beta}$ are shifted by the same lattice vector $\boldsymbol{R}'$, the second derivative of the energy with respect to positions should be the same due to the translational invariance property of hamiltonian operator. Therefore, the dynamical matrix should rely on the vector difference, $\boldsymbol{R}_n - \boldsymbol{R}_m$ and not on n and m

$$\widetilde{D}_{ni\alpha,mj\beta} = \widetilde{D}_{i\alpha,j\beta}(\boldsymbol{R}_n - \boldsymbol{R}_m) \tag{2.26}$$

The ionic displacement vectors can be defined as

$$\tilde{u}_{ni\alpha} = u_{i\alpha} e^{i\boldsymbol{k}\cdot\boldsymbol{R}_n} \tag{2.27}$$

while the dependence of dynamical matrix on the wave-vector $\boldsymbol{k}$ can be shown as

$$D_{i\alpha,j\beta}(\boldsymbol{k}) = \sum_{\boldsymbol{R}} \widetilde{D}_{i\alpha,j\beta}(\boldsymbol{R}) e^{-i\boldsymbol{k}\cdot\boldsymbol{R}} = \sum_{n} e^{-i\boldsymbol{k}\cdot\boldsymbol{R}_n} \frac{1}{\sqrt{M_i M_j}} \frac{\partial^2 V}{\partial S_{ni\alpha} \partial S_{mj\beta}} \tag{2.28}$$

Using Eqs. (2.26), (2.27), and (2.28) in Eq. (2.23) gives

$$\sum_{j,\beta} D_{i\alpha,j\beta}\,(\boldsymbol{k}) \tilde{u}_{j\beta} = \omega^2 u_{i\alpha} \tag{2.29}$$

$$\boldsymbol{D}(\boldsymbol{k}) \cdot \boldsymbol{u} = \omega^2 \boldsymbol{u} \tag{2.30}$$

The size of $\boldsymbol{D}(\boldsymbol{k})$ is d × ν which is a feasible size to get solutions for values of $\boldsymbol{k}$.

The general solution for the displacement of ion j is

$$\boldsymbol{S}_{n,j}(t) = \sum_{l,\boldsymbol{k}} c_{\boldsymbol{k}}^{(l)} \frac{1}{\sqrt{M_j}} \hat{\boldsymbol{e}}_{\boldsymbol{k}j}^{(l)} e^{i(\boldsymbol{k}\cdot\boldsymbol{R}_n - \omega_{\boldsymbol{k}}^{(l)} t)} \tag{2.31}$$

where $c_{\boldsymbol{k}}^{(l)}$, and $\hat{\boldsymbol{e}}_{\boldsymbol{kj}}^{(l)}$ correspond to amplitude of oscillation, and set of d components of displacements of ion j in d dimensions. l can take d $\times$ ν values.

CHAPTER 3

DEVELOPMENT AND APPLICATION OF AB-INITIO FORCE FIELDS FOR NOBLE GAS ADSORPTION IN MOFS*

3.1 Introduction

Energy efficient storage and separation of gases have been an important challenge in industry.[5, 100] Various works investigated the separation of CH_4/H_2, CO_2/N_2, CH_4/N_2, CO_2/H_2 and CO_2/CH_4 gas mixtures.[101-106] However, similar investigations for noble gas storage and separation have not been extensively made. Although noble gases are not abundantly found in the nature, they have many uses such as lighting, lasers, carrier gas, leak testing, propellant, and medical operations.[33, 107-109] Besides existing in the air naturally, they can also be generated by fission, decay of fission products, and isotope production.[110] One current industrial challenge is separating radioactive Kr from Xe which is conventionally done using energy-intensive cryogenic processes. An alternative to this process is using porous materials for adsorption of noble gases around room temperature which is more energy efficient. Earlier studies have demonstrated that zeolites can be selective adsorbents for noble gases however they do not have high capacities.[111]

---

* Results described in this chapter have been published previously in Hakan Demir, Jeffery A. Greathouse, Chad L. Staiger, John J. Perry IV, Mark D. Allendorf and David S. Sholl, "DFT-based force field development for noble gas adsorption in metal organic frameworks", Journal of Materials Chemistry A, 2015, 3, 23539–23548

Since MOFs have more structural versatility than zeolites, investigation of MOFs with better adsorption/separation properties is crucial. Experimentally, there have been a number of studies comparing MOFs and conventional porous materials. Mueller et al.[112] performed Kr/Xe (94% / 6%) breakthrough experiments in Cu-BTC at 55°C, 40 bar and found out that Xe adsorption in Cu-BTC is almost twice of that in activated carbon. Thallapally et al.[110] studied Xe/Kr separation at noncryogenic temperatures with Ni-MOF-74, MOF-5, and activated charcoal. They have found Ni-MOF-74 to be better than MOF-5 and activated carbon for Xe adsorption and also exhibit higher Xe/Kr selectivity than activated carbon. In Fernandez et al.'s work[107], Kr and Xe adsorption is studied in FMOFCu and FMOFZn. In FMOFCu, adsorption selectivity of Xe/Kr can be adjusted above or below 1 by adjusting temperature. Kr adsorption becomes more favorable below 0°C with hindered Xe diffusion inside the pore channels owing to reduced pore flexibility at low temperatures. Liu et al.[111] investigated Xe and Kr adsorption/separation in ppm levels at room temperature using Ni-MOF-74 and Cu-BTC. It is observed that Ni-MOF-74 can separate 400 ppm Xe from a gas mixture having 40 ppm Kr with a Xe/Kr selectivity of ~7. Dorcheh et al.[113] studied pure Kr, and Xe adsorption-desorption in COF-102, ZIF-8, MFU-4l, and Cu-BTC. They have identified the latter two materials as promising materials for Kr, and Xe adsorption/separation. In Pawsey et al.'s study[114] Xe adsorption is measured in IRMOF-1, -2, -3, and -6 around room temperature from 0.1 to 1 bar. They have seen Henry's law behavior in the pressure range studied and identified preferential Xe binding sites near carboxylate and Zn_4O groups in the cage corners using ^{129}Xe nuclear magnetic resonance spectroscopy.

One of the earliest noble gas GCMC simulations is performed by Greathouse et al.[115] who investigated Ar, Kr, and Xe adsorption in IRMOF-1. They have used a hybrid FF which includes interactions between Zn, O atoms, and benzene dicarboxylate (BDC) linkers and assumed MOF structure to be semiflexible where BDC linkers are rigid. Their simulation results for Xe at 292 K are in agreement with the experimental data at low pressures while at higher pressures simulations start to underpredict the experiments. Dubbeldam et al.[116] simulated Ar adsorption in IRMOF-1 in GCMC using flexible MOF structure where simulations overpredict experimental data. This is thought to be because of discrepancies between experimental sample and perfect structure used for simulation. Their simulation study also identified adsorption sites at both low and room temperature which agree with experimental results. Ryan et al.[117] investigated Xe/Kr separation with eight MOFs having various topologies, pore sizes, linkers, and metal atoms where they concluded that small pores are needed to selectively adsorb xenon over krypton with strong adsorption sites. Among the materials studied, MOF-505 is identified as the best material in terms of its high adsorption capacity and selectivity. Sikora et al.[118] generated over 100,000 hypothetical MOFs and screened them for Xe/Kr separation. For high Xe/Kr selectivity, it is suggested have pores with similar sizes to a xenon atom and approximate uniform tubes. Gurdal et al.[109] investigated adsorption of Xe/Kr and Xe/Ar mixtures in various classes of MOFs using both GCMC and Ideal Adsorbed Solution Theory (IAST). For all nine MOFs studied at 10 bar, 298 K, IAST predictions are shown to have decent agreement with GCMC simulations. In van Heest et al.'s work[33], more than 3000 MOFs are screened for Ar/Kr, Kr/Xe, and Xe/Rn separation and top performers are identified. IAST is demonstrated to be able to predict binary selectivities unless there is not any

inaccessible pore. Materials that favored adsorption of smaller adsorbates are also found whose performance get better as temperature decreases.

While modeling nonbonded interactions for charge neutral adsorbates, generally only dispersion (vdW) interactions are considered. However, besides dispersion, polarization may also have significant contribution to gas adsorption in MOFs. Meek et al.[108] studied the polarization effect on gas (N_2, Ar, Kr, Xe, and Rn) adsorption in IRMOF-2 functionalized with –F, -Cl, -Br, and -I groups and observed higher gas uptake as linker polarizability increases. Maurin et al.[119] worked on adsorption of nonpolar (Ar, CH_4) and quadrupolar (CO_2, N_2) species on siliceous faujasite. They have revealed a roughly linear relationship between differential heat of adsorption at low coverage and adsorbate polarizability. Another work of Maurin et al.[120] which is about N_2 and Ar adsorption on ion-exchanged X-faujasites revealed that presence of extra-framework ions increased polarization and differential enthalpy of adsorption at zero coverage. Cirera et al.[121] used polarizable FFs for both adsorbate and adsorbent to study water adsorption on MIL-53 (Cr) and determined that hydrogen bond formation is affected by polarization. In Dzubak et al.'s work[16], first-principles based polarizable FFs are derived for CO_2 and N_2 adsorption on Mg-MOF-74 with NEMO (non-empirical model potential) decomposition technique to partition MP2 energies into four components, repulsion, dispersion, electrostatic, and dispersion. Using derived FF, they have seen good agreements with experimental data for CO_2, and N_2 adsorption in Mg-MOF-74 especially at low pressures. Moreover, they have tested the transferability of the FF in Mg_2(dobpdc) and MOF-5 for CO_2 adsorption and observed that simulations agree well with the experiments principally at low pressures. McDaniel et al.[122] also developed ab-initio based FFs for CO_2 adsorption in ZIF-8 and ZIF-

71 by separating the interaction energies into different terms (exchange, electrostatic, dispersion, and polarization) using Symmetry-Adapted Perturbation Theory (SAPT) energy decomposition method. They have shown the accuracies of their derived FFs by illustrating the agreement between experimental and simulated isotherms for both ZIFs. In their FFs, the polarization contribution is insignificant for both ZIFs.

Many computational studies take advantage of generic FFs, namely UFF[123], DREIDING[124], OPLS-AA[125] etc. or their mixed combinations. Although they bring ease of performing simulations, they are not parameters derived specifically for MOFs or zeolites. Since the accuracy of FFs affects the acceptance or rejection of a move[98], inaccurate FFs may lead to incorrect gas adsorption results. Thus, there have been various efforts to modify the generic FFs to have good agreement with experimental adsorption data. Fairen-Jimenez et al.[126] modified UFF parameters in two different ways to investigate CH_4 and CO_2 adsorption in ZIF-8. For one of the modified UFF parameter sets (UFF+), only ε values are adjusted while for the other modified UFF parameter set (UFF*) both ε and σ are changed. It is shown that UFF* parameters leads to considerable differences between simulation and experiment while UFF+ parameters are able to describe both CH_4 and CO_2 adsorption compared to experiments. Moreover, UFF+ parameters are found to be transferable for CH_4 adsorption in ZIF-20. Perez-Pellitero et al.[127] scaled down UFF parameters and obtained good agreement with experimental N_2, CO_2, and CH_4 isotherms for ZIF-8 at 303 K using modified UFF parameters. In Li et al.'s work[128], it is demonstrated scaled DREIDING parameters lead to good description of H_2 adsorption in organic crystal TTB.

Although predictions of generic FFs can be sufficient for initial screening of materials, they are not quantitatively accurate for many adsorbate-adsorbent combinations. Deriving FFs based on experimental data is also not a very good idea, since experimental data may be limited and those FFs are very unlikely to predict adsorption characteristics of new materials. This shows the importance of developing FFs based on ab-initio methods to predict adsorption properties. An extensive review about FF development has been published by Fang et al.[129]

In the literature, most of the FF development works are based on cluster models of adsorbents but recently more studies with periodic adsorbent models have started emerging. Kulkarni et al.[130] used periodic models to develop alkane FFs in MIL-47 (V) which has been shown to have good predictions of loading and heats of adsorption. Furthermore, transferability of those FFs are tested in MIL-53 (Cr) and validated. Gee et al.[131] developed DFT-based FFs to describe adsorption of C_8 cyclic hydrocarbons in a few MOFs without any open metal site (DMOF-1, IRMOF-1, MIL-47, and UiO-66). The performance of derived FFs has slightly outperformed that of generic FF, DREIDING. Haldoupis et al.[132] derived ab-initio based FFs to predict CO_2 adsorption in M-MOF-74 (M=Co, Cu, Mn, and Ni) and observed good agreement between simulations and experiments at low pressures, but the simulations start to overpredict the experiments as the pressure increases. In Kim et al.'s work[133], MP2-based FFs are developed to describe CO_2 adsorption in zeolites and M-MOF-74 (M=Fe, and Mg) and methane adsorption in zeolites. It is shown that the derived FFs are able to accurately predict adsorption in both MOFs and zeolites. Prakash et al.[134] derived ab-initio based FFs to describe CH_4, H_2, and N_2 adsorption in ZIF-95 and ZIF-100. It is demonstrated that using derived FFs the

predictions are in agreement with the experiments for CH_4 adsorption at room temperature in ZIF-95 and ZIF-100. The simulations predicted ZIF-100 to have higher H_2 uptake than ZIF-95 while it is vice versa for CH_4 adsorption.

The size of the adsorbent model selected rules the accessible quantum chemical level for FF development. Although coupled-cluster theory, i.e. CCSD (T), can give the most accurate results, it cannot be applied to the systems except very small clusters owing to its huge computational cost. Similarly, MP2 method is also limited to clusters although bigger systems can be investigated compared to CCSD (T). DFT is a decently accurate and computationally accessible method which can be used to study periodic systems. As described in Chapter 2, the standard DFT is not good at describing dispersion interactions. To accommodate dispersion effects more accurately, the dispersion-corrected DFT functionals have been used in many studies. For example, Rana et al.[75] investigated CO_2 enthalpies in Cu-BTC and M-MOF-74 variants (M=Co, Mg, and Ni) using different DFT functionals namely LDA, GGA, PBE-D2 and five different vdW functionals. They demonstrated that vdW-DF functionals have the most accurate predictions of adsorption enthalpies and GGA functional predictions have big discrepancies compared to experimental enthalpies of adsorption. Poloni et al.[135] examined adsorption characteristics of CO_2 in Mg-MOF-74 and Ca-BTT with PBE, PBE-D2, and five different vdW-DFT functionals. The adsorption enthalpies of CO_2 in Mg-MOF-74 acquired using PBE-D2, vdW-DF and vdW-DF2 are in good agreement with experiments. Comparing experimental CO_2-MOF bond distances with simulations, vdW-DF and vdW-DF2 predictions are found to be the best. Fang et al.[136] derived a transferable PBE-D2 based FF that can describe CO_2 adsorption in siliceous CHA, DDR, and MFI zeolites where there is a good agreement

between simulations and experiments in terms of adsorption isotherms and heats of adsorption at zero coverage.

3.2 FF Development

In this work, only the non-bonded interactions are modeled since the MOF structures are assumed to be rigid. The FF parameters are developed solely for adsorbate-adsorbent interactions and parameters for adsorbate-adsorbate interactions are taken from van Heest et al.[33]. The non-bonded interactions are described by the summation of two terms, vdW and polarization

$$E_{FF}(R_{ij}) = E_{vdW} + E_{pol} = s_{12}\sum \frac{C_{12}^{ij}}{R_{ij}^{12}} - s_6 \sum \frac{C_6^{ij}}{R_{ij}^6} - \frac{1}{2}\alpha E_f^2 \tag{3.1}$$

where R_{ij} defines the interaction distance between atoms i and j, s_{12} and s_6 are scaling factors, C_{12}^{ij} and C_6^{ij} are repulsive and attractive coefficients, α denotes atomic polarizability, and E_f is the induced electric field on an adsorbate atom by other atoms. The relationship between C_{12}^{ij} and C_6^{ij} is as follows

$$\frac{C_{12}^{ij}}{C_6^{ij}} = \frac{(R_o^i + R_o^j)^6}{2} \tag{3.2}$$

where R_o^i and R_o^j denote the vdW radii of atoms i and j. The values of C_6 and R_o are obtained from Grimme's work[76]. The vdW part of the FF is assumed to be classically described by 12-6 LJ potential

$$E_{LJ}(R_{ij}) = 4\varepsilon_{ij}\left[\left(\frac{\sigma_{ij}}{R_{ij}}\right)^{12} - \left(\frac{\sigma_{ij}}{R_{ij}}\right)^{6}\right] = \frac{A_{ij}}{R_{ij}^{12}} - \frac{B_{ij}}{R_{ij}^6} \tag{3.3}$$

The summation of inverse distances ($\sum \frac{1}{R_{ij}^{12}}$ and $\sum \frac{1}{R_{ij}^6}$) are obtained by using a $5 \times 5 \times 5$ model for ZIF-8, and Cu-BTC and a $5 \times 5 \times 10$ model for M-MOF-74 structures where

the adsorbate is placed around the center of the pore. Larger model sizes are not needed since the total inverse distances do not change significantly beyond the models used.

For the calculation of the induced electric field in the polarization term, the partial charges for the frameworks atoms are assigned by the density-derived electrostatic and chemical (DDEC) charge method[137-139] performing DFT calculations in single unit cells. Having obtained partial charges, the polarization energies are determined using a modified multipurpose simulation code (MUSIC)[140]. Backpolarization is not considered implying the partial charges are kept constant regardless of the adsorbate loading.

Eight different scaling factors are used for each adsorbate-adsorbent atom type and they are fitted with a constrained linear least-square method. To have physically relevant parameters, two constraint criteria are selected. Firstly, no ε parameter is allowed to be two orders of magnitude bigger than any other ε parameter. Secondly, no σ parameter is allowed to be larger than twice of any other σ parameter.

The FF development procedure is illustrated in Figure 2. The procedure starts with the generation of 300 random adsorbate configurations in the porous space by keeping a minimum distance of 2.8 Å between adsorbate and any other framework atom (R_{min}). It should be noted that smaller R_{min} values lead to many unfavorable sites. For all those random configurations, DFT adsorption energies are calculated and $E_{DFT} - E_{pol}$ is fitted to get initial ε and σ. These FF parameters are used to generate GCMC configurations which enables further sampling of the low energy region which is the most relevant region for the adsorption phenomena. After including DFT adsorption energies of GCMC configurations to the initial list of interaction energies, the LJ parameter fitting is done again with all configurations (random+GCMC) to obtain the final parameters. The fitting

qualities are assessed by mean deviation (MD) and mean absolute deviation (MAD) between DFT and FF energies. In some cases where the fitting is not satisfactory enough, a weighted fitting up to 0 kJ/mol is done to improve description of the lowest interaction energy region. Eventually, in all cases MAD values are around 2-3 kJ/mol which implies a very good description of DFT energies. The derived FF parameters are tabulated in Tables 7-12.

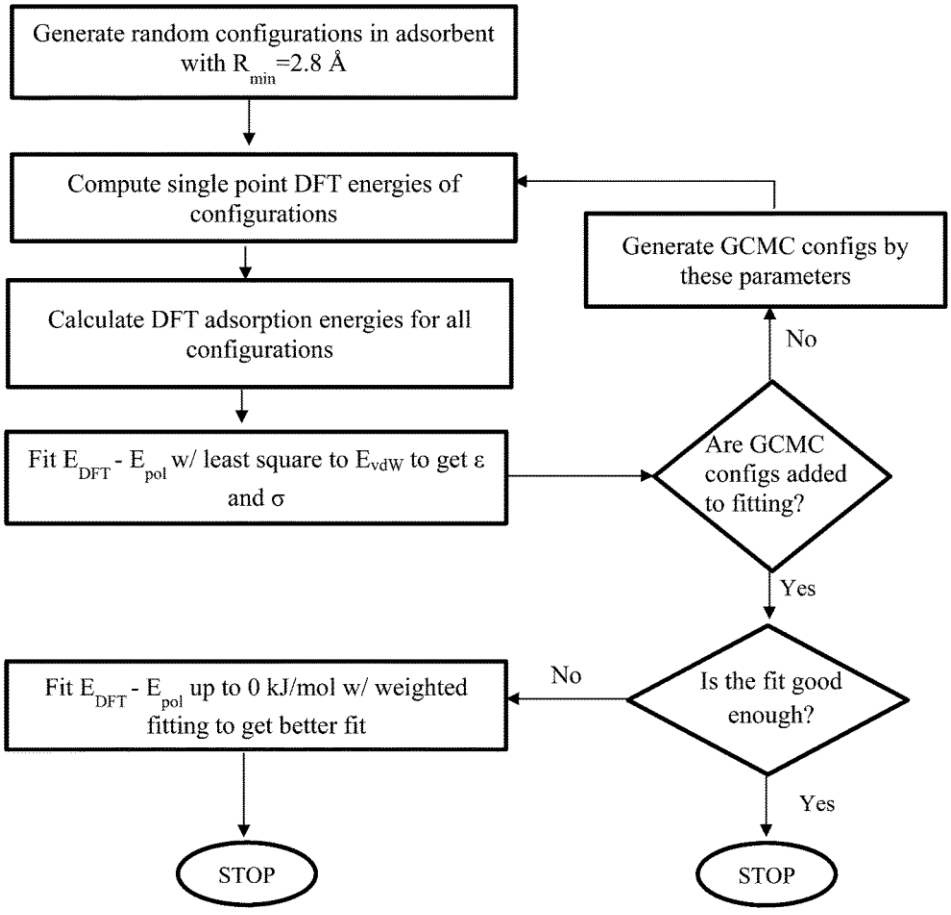

Figure 2. The schematic of FF derivation procedure.

3.3 Computational Methods

All DFT calculations are performed by VASP version 5.3.2 and all structures are fully optimized using PBE-D2, vdW-DF, vdW-DF2 functionals where *k*-space is sampled only at the Γ-point. Optimizations employ conjugate gradient method where the total energy and ionic force convergence criteria are 1×10^{-4} eV and 3×10^{-2} eV/Å, respectively. Both optimizations and single-point energy calculations are performed with a 400 eV kinetic energy cutoff. For the optimizations and partial charge assignments, the primitive cells of M-MOF-74 (54 atoms), ZIF-8 (138 atoms), and Cu-BTC (156 atoms) are utilized. The lattice parameters of the optimized and experimental structures are listed in Table 13. The experimental structures of Co-MOF-74, Mg-MOF-74, Ni-MOF-74, Zn-MOF-74, Cu-BTC are acquired from CoRE MOF database[29] with the REFCODES SATNOR, VOGTIV, LECQEQ, WOBHIF, FIQCEN, respectively. The ZIF-8 structure is retrieved from CSD with the REFCODE OFERUN and pymatgen[141] is used to get the primitive cell of it. The adsorption energies in M-MOF-74 structures are obtained using $1 \times 1 \times 2$ supercell of optimized primitive cells to reduce self-interaction effect of adsorbate atoms along the pore channel (*c* axis). For the calculation of binding energies, no entropic effect is included. Involving entropic effects may decrease the discrepancies between simulations and experiments.

In all GCMC simulations, frameworks are kept rigid during both isotherm and configuration generation. RASPA code[142] is used to generate isotherms where polarization effects are taken into account for all FFs in the pressure range of 10^{-6} to 20 bar, trying translation and insertion/deletion moves with equal probabilities. For M-MOF-74 (ZIF-8 and Cu-BTC), 10,000 (5,000) equilibration and 10,000 (5,000) production cycles are

employed where a cycle includes N steps, N being the amount of molecules with a minimum of 20 steps. LJ interactions are truncated at 12, 15, and 11.9 Å for M-MOF-74, Cu-BTC, and ZIF-8, respectively. No tail correction is included. Ab-initio based FFs are utilized with the structures optimized with the corresponding DFT functional but, for UFF isotherms, PBE-D2 optimized structures are used. Radial Distribution Functions (RDFs) for M-MOF-74 (Cu-BTC, and ZIF-8) are obtained from GCMC simulations with 15,000 (10,000) equilibration and production cycles. Density plots are acquired using 15,000 (10,000) equilibration and production cycles for M-MOF-74 (Cu-BTC, and ZIF-8). For density plots, 17, 15, and 15 Å cutoffs are selected for M-MOF-74 ($3 \times 3 \times 6$ supercell), Cu-BTC ($2 \times 2 \times 2$ supercell), and ZIF-8 ($3 \times 3 \times 3$ supercell), respectively. To generate GCMC configurations, initial FF parameters are employed in the original MUSIC code using 4×10^6 total steps with equal equilibration and production steps. All GCMC configurations are created at 100 bar and 303 K except for Xe-Cu-BTC system with vdW-DF2 energies (created at 1 bar and 303 K). The latter choice for Xe-Cu-BTC system is made to sample the low energy regions better which cannot be done good enough at 100 bar. The interaction energies corresponding to the GCMC configurations generated at 100 and 1 bar can be seen in Figure 35 of Appendix A. Duren's method[143] is used to determine the surface areas of optimized structures with a nitrogen probe molecule.

3.4 Experimental Methods

Cu-BTC and ZIF-8 materials are acquired as commercially available Basolite®-C300 and Basolite®-Z1200 and they are used in experiments without any modification. M-MOF-74 variants are prepared, activated and used for gas adsorption as reported earlier.[25, 144] Ar adsorption on Cu-BTC and ZIF-8 is done at 308 K and P = 0-20 bar while

Ar and Xe adsorption on M-MOF-74 variants are performed at 292 K and P = 0-1 bar.[25, 144] Experimental heats of adsorption are calculated using the Clausius-Clapeyron equation[145] at 273 and 292 K.

3.5 Results

The very first thing that is checked about the developed FFs is their accuracy compared to the DFT energies. This is discussed with Xe adsorption in Co-MOF-74 since polarization and other non-classical effects are more pronounced for Xe than Ar adsorption. The accuracies of other fitted FFs are similar to this case, therefore, they are not discussed. In Figure 3, the correlation between FF and DFT energies is shown for the adsorption of Xe in Co-MOF-74. The black data points represent randomly generated configurations while the red ones are generated from GCMC run using the initial FF fitted to the random configurations.

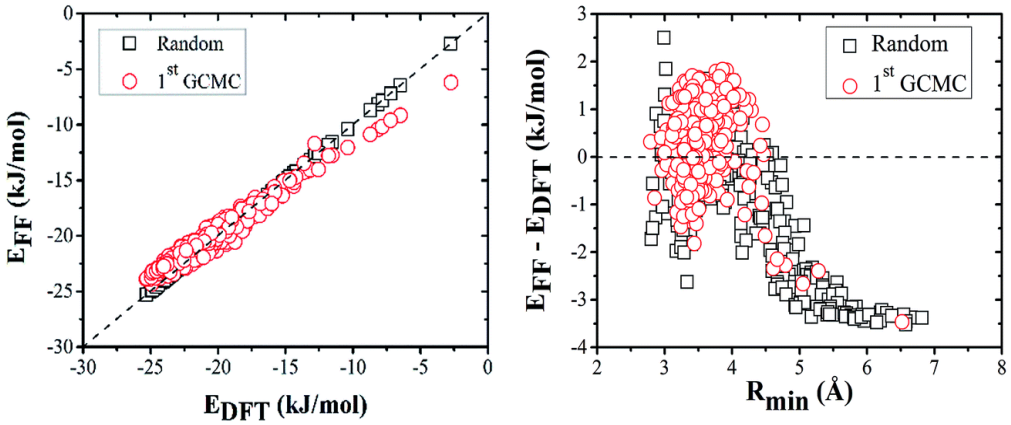

Figure 3. Correlation between vdW-DF2 and FF adsorption energies for Xe adsorption in Co-MOF-74.

It can be seen that the FF energies can describe the DFT energies very well over a large range of energies. For most of the configurations, the deviation between FF and DFT energies are less than 2 kJ/mol. The MD and MAD values calculated over the configurations used in fitting are -0.99 and 1.11 kJ/mol, respectively.

One important aspect of this study is incorporating the effect of polarization in the calculations which is not considered in most of the studies. In Figure 4, for Xe configurations in Ni-MOF-74, the absolute percentage of the polarization energy over total PBE-D2 adsorption energy is plotted.

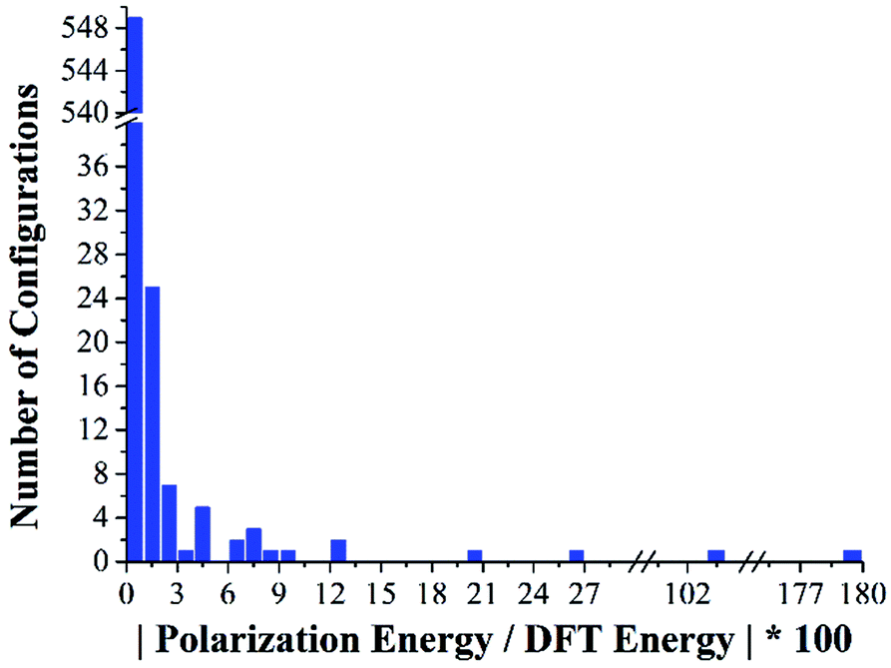

Figure 4. Histogram of effect of polarization energy compared to DFT energy for Xe-Ni-MOF-74.

Since the polarization energy relies on the atomic polarizability which gets enhanced as the adsorbate size increases, the effect of polarization energy in a Xe adsorption case is more than Ar adsorption. Thus, the polarization contribution plotted in

Figure 4 is one of the largest observed in the whole set of the calculations. For most of the the configurations, the polarization effect is very small and on average the absolute percentage of polarization over DFT energy is 1%. This implies the polarization effect is negligible for the FF development for noble gas adsorption in the MOFs studied.

After validating the accuracy of derived FFs, they are used to generate adsorption isotherms and heats of adsorption to be compared with experimental isotherms. The heat of adsorption plots can be found in Appendix A. Figure 5 illustrates the adsorption Ar and Xe isotherms for Co and Mg-MOF-74 at 292 K.

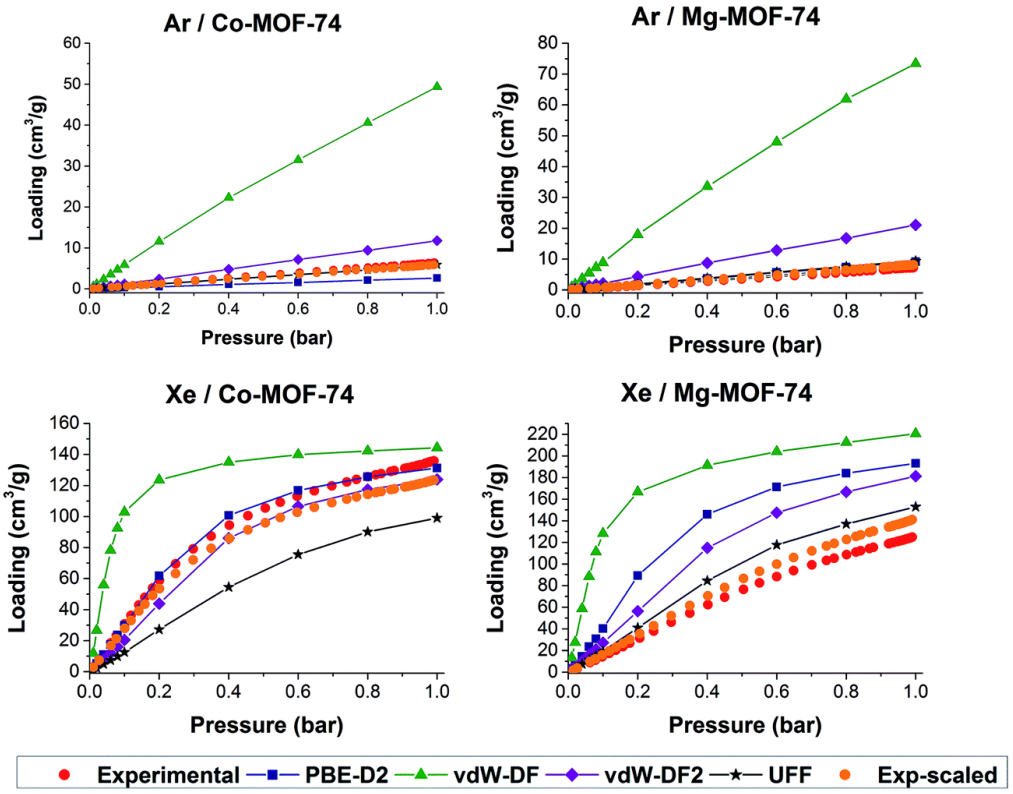

Figure 5. Ar and Xe adsorption isotherms for Co-MOF-74 and Mg-MOF-74 at 292 K.

The prediction of PBE-D2 based FF for Xe adsorption in Co-MOF-74 agrees well with the experimental data. Compared to PBE-D2 based FF, vdW-DF2 based FF predictions have bigger differences with respect to experimental isotherms, especially for Ar adsorption. Among all the derived FFs, vdW-DF based FFs have the worst predictions for both Ar and Xe at all pressures. In all cases, vdW-DF based FFs overpredict the experimental gas uptake significantly. Although UFF can predict Ar adsorption accurately, it underpredicts Xe adsorption. In many studies, the adsorption isotherms are scaled based on the ratio of simulated and experimental surface areas, if the difference between them are significant.[116, 146] Similarly, the scaled experimental isotherms are also plotted in Figure 5. This leads to better agreement between experimental and simulation data. PBE-D2 based FF and UFF can predict experiments well for Ar adsorption in Mg-MOF-74, however, vdW-DF and vdW-DF2 based FFs overpredict the experiments, especially the former significantly. For Mg-MOF-74, although all FFs overpredict the experimental Xe uptakes, UFF predictions are the best for both Xe and Ar adsorption. Although some of the DFT-based FFs can predict adsorption well in Co-MOF-74 (Ar and Xe) and Mg-MOF-74 (Ar), none of them can predict Xe-Mg-MOF-74 accurately. Since the experiments for Ar and Xe adsorption in Mg-MOF-74 are done by following the same procedures, prediction quality differences cannot be ascribed to experimental errors or sample qualities.

Similar to Figure 5, Figure 6 and 7 show the comparison between the experimental and simulated isotherms for Ni and Zn-MOF-74, Cu-BTC, and ZIF-8. Since the average discrepancies between simulated and experimental surface areas are 5% and 0.3% for Ni-MOF-74 and ZIF-8, the corresponding experimental isotherms are not scaled with the ratio of simulated to experimental surface areas.

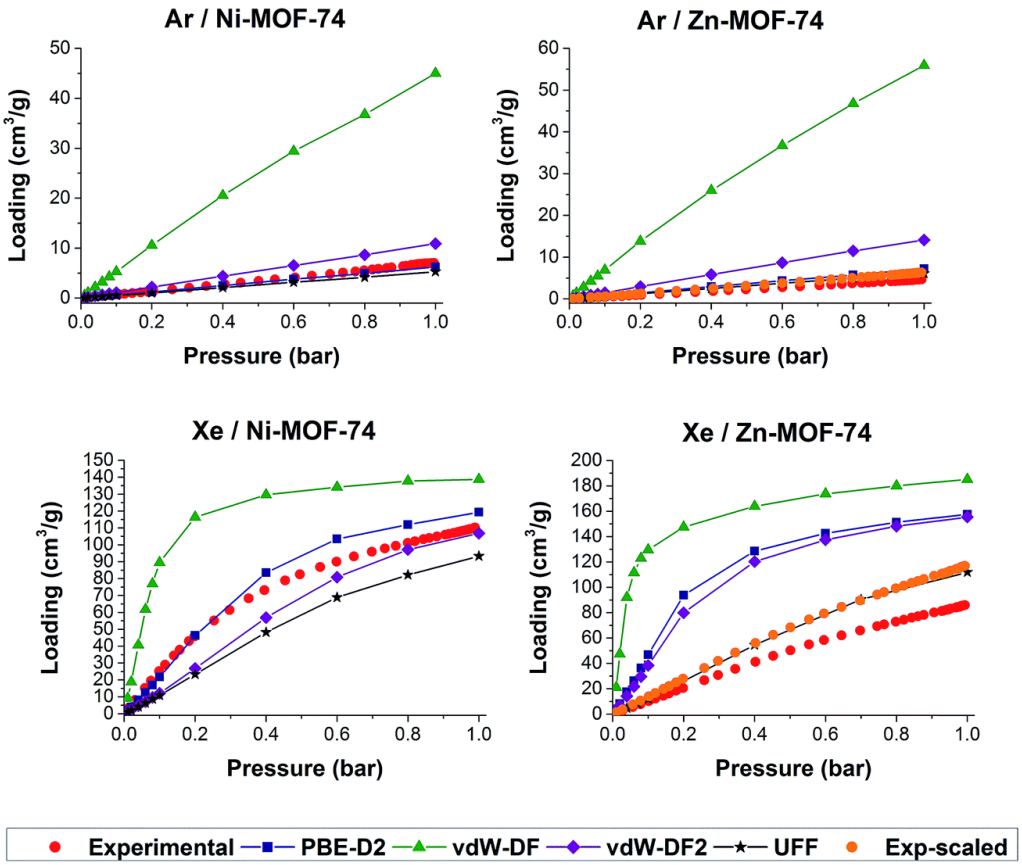

Figure 6. Ar and Xe adsorption in Ni-MOF-74 and Zn-MOF-74 at 292 K.

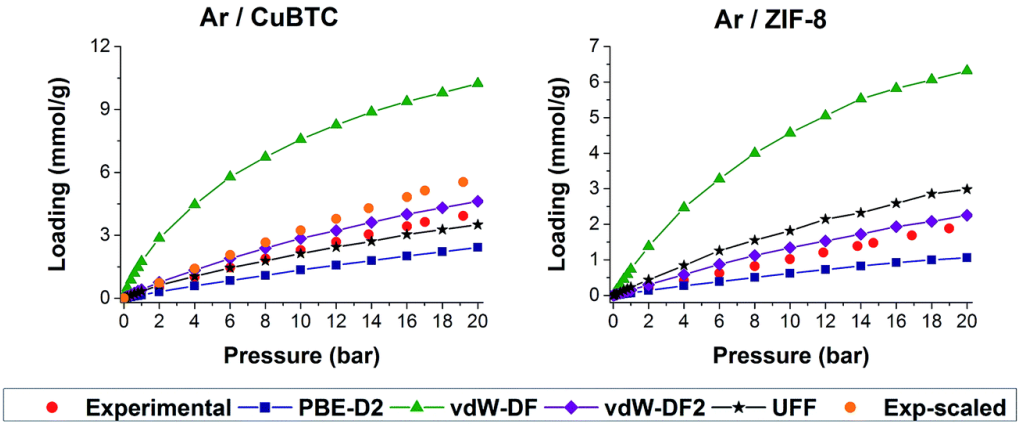

Figure 7. Ar adsorption in Cu-BTC and ZIF-8 at 292 K.

As it has been observed for Co and Mg variants of M-MOF-74, the vdW-DF based FF overpredicts the experimental isotherms significantly shown in Figure 6 and 7. The success of other ab-initio based FFs, PBE-D2 and vdW-DF2, varies depending on the system. It is observed that their predictions can be less than, almost equal to, or greater than experimental uptake. For Xe adsorption in Ni-MOF-74, PBE-D2 based FF leads to accurate prediction up to 0.4 bar after which it starts overpredicting. Although UFF underpredicts the Xe adsorption in Ni-MOF-74 considerably, its adsorption prediction for Ar-Ni-MOF-74 is in agreement with experimental data. Compared to scaled experimental isotherms of Ar and Xe adsorption in Zn-MOF-74 (scaling factor = 36%), UFF predictions have excellent agreements. On the other hand, DFT-based FFs generally overpredict experiments. The only exception is Ar-Zn-MOF-74 where PBE-D2 based FF predictions fall onto the experimental uptakes. As seen in Figure 7, vdW-DF2 based FF can predict the scaled experimental Ar uptakes in Cu-BTC up to 10 bar well. Still, it should be kept in mind that the scaling factor is considerably large (41%) for Cu-BTC. The UFF predictions are below the experimental loadings for Ar adsorption in Cu-BTC. Similar observations have been made in other works. Zang et al.[147] have used UFF to predict water adsorption in Cu-BTC and calculated very small water uptake which implies a considerably big underestimation of the experiments. In Rana et al's work[148], the combined UFF and DREIDING parameters also have led to underestimation of methane adsorption in Cu-BTC. Getzschmann et al.[149] have shown that using UFF parameters at 77 (87) K caused underprediction of experiments between 1×10^{-6} and 1×10^{-4} (1×10^{-5} and 1×10^{-4}) bar. Interestingly, below those pressures, experimental uptakes are overpredicted. In a wider range of pressure (0-200 bar), they have also shown simulations underpredicting the

experiments. The reason for failure of generic FFs to predict methane uptake accurately is considered as poor description of interactions between methane-open metal sites by Koh et al.[150] They have modified those interactions and predicted the experiments accurately. For ZIF-8, experimental Ar adsorption is predicted closely by vdW-DF2 based FFs while it is overpredicted by UFF.

Besides, investigating the performance of FFs case by case, the overall prediction quality of FFs is also determined by considering the normalized absolute differences in adsorption loadings at 1 bar between experiment and simulation. The details of this comparison can be found in Appendix A. The normalized absolute difference is obtained as follows

$$\Delta q = \frac{\left|\theta_{exp} - \theta_{calc}\right|}{\theta_{exp}} \tag{3.4}$$

where Δq, θ_{exp}, and θ_{calc} are normalized absolute adsorption difference, experimental loading at 1 bar, and calculated loading at 1 bar, respectively.

In Figure 8, the Δq value for each FF is plotted. On average, UFF predictions have the lowest deviation from experiments (0.341, meaning simulated loadings deviated by 34.1% from the experimental loadings, on average) and PBE-D2, and vdW-DF2 based FF predictions deviate slightly more, 0.370 and 0.765, respectively. The vdW-DF based FF predictions always overestimate the experimental loadings considerably giving the largest deviation (4.672). Taking into account the relatively large standard deviations in Δq, the overall prediction qualities of UFF, PBE-D2, and vdW-DF2 based FFs are similar. Since DFT-based FFs need both quantum chemical calculations and parameter fitting efforts, it can be concluded that using UFF is more advantageous. The details of absolute adsorption amount differences can be seen in Table 2.

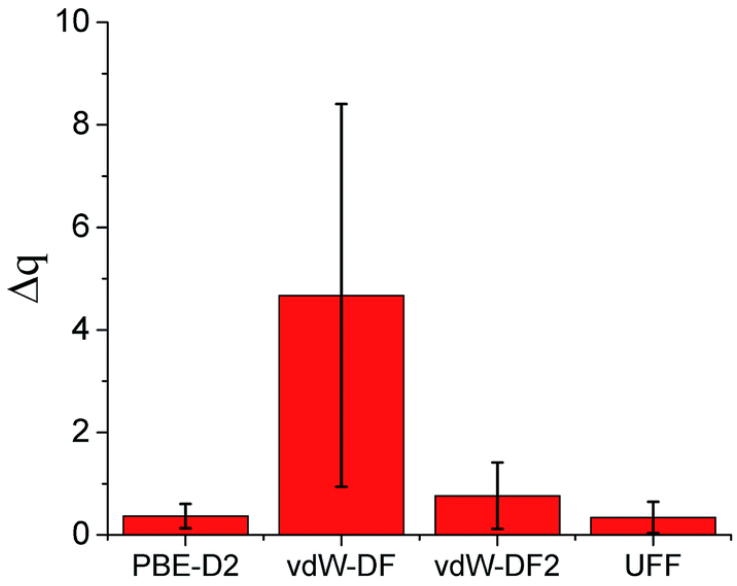

Figure 8. Averaged normalized absolute deviations of simulated loadings of FFs from experiments.

Table 2. Normalized absolute adsorption amount differences with respect to experiments at 1 bar.

1bar	**PBE-D2**	**vdW-DF**	**vdW-DF2**	**UFF**
Ar-Zn-MOF-74	0.551	11.013	2.030	0.312
Xe-Zn-MOF-74	0.791	0.964	0.613	0.222
Ar-Ni-MOF-74	0.116	5.400	0.550	0.246
Xe-Ni-MOF-74	0.082	0.259	0.031	0.154
Ar-Co-MOF-74	0.590	6.690	0.836	0.080
Xe-Co-MOF-74	0.034	0.062	0.088	0.271
Ar-Mg-MOF-74	0.268	9.174	1.917	0.298
Xe-Mg-MOF-74	0.548	0.768	0.453	0.225
Ar-ZIF-8	0.373	6.125	0.448	1.216
Ar-Cu-BTC	0.351	6.261	0.688	0.388
Average	**0.370**	**4.672**	**0.765**	**0.341**
St.dev	0.237	3.734	0.648	0.303

Heat of adsorption plots are given in Appendix A where the trends in the heat of adsorption values are similar to the trends in the loading values. However, there are two

exceptions: Ar adsorption in Mg and Ni-MOF-74. In these systems, the simulated heat of adsorption profiles are flat, while in Ni-MOF-74, the experimental heat of adsorption diminishes as the loading increases (by ~10 kJ/mol), and in Mg-MOF-74, the experimental heat of adsorption is enhanced up to 2 cm^3/g and then decreases. None of the FFs used in this study could reproduce these experimental observations in these two systems.

To identify the preferential adsorption sites, ensemble-averaged gas densities are acquired from GCMC simulations at different pressures. In Figure 9, Ar density plots in Cu-BTC obtained using PBE-D2 based FF and UFF are depicted. Since other DFT-based FFs lead to similar plots, they are not shown.

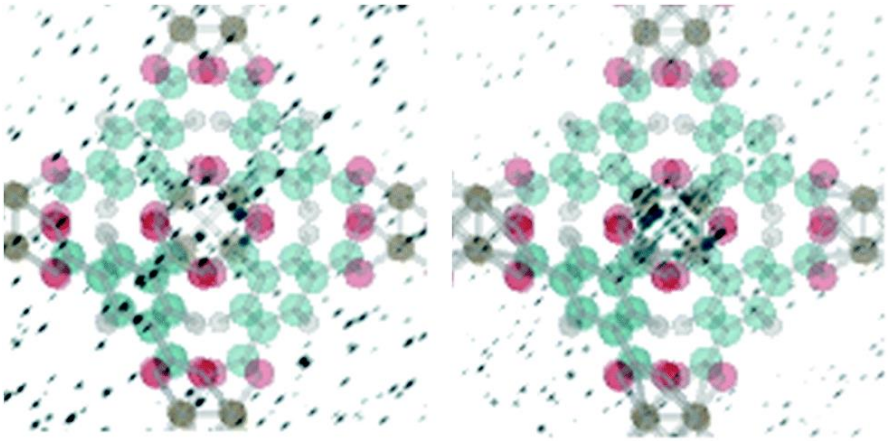

Figure 9. Ar density plots in Cu-BTC using PBE-D2 based FF (left) and UFF (right) at 0.01 bar and 308 K. (The framework is drawn transparent for clarity.)

PBE-D2 based FFs predict the strongest adsorption around the windows of the tetrahedral pocket and in the pocket. The occupation near the pocket windows is slightly more enhanced than that in the pockets. Moreover, there is notable adsorption in the main pores. The density plot obtained using UFF is similar to that of PBE-D2, however, the adsorption in the main pores is relatively less while the adsorption in the windows of the

pockets is more occupied than the pockets. Hulvey et al.[151] has used DREIDING parameters to study Ar adsorption in Cu-BTC and they demonstrated Ar adsorption to be between window and pocket sites. The density plots in this study are similar to those, however, the additional sites of adsorption are also observed.

In Figure 10, the main adsorption sites, pore corners, for Xe adsorption in Co-MOF-74 are shown. As the pressure is increased, the adsorption site distribution does not change significantly and pore corners remain to be the primary adsorption sites. Rana et al.[148] determined similar methane density plots in Co-MOF-74 using DREIDING parameters where corners of the pores are illustrated as the strongest adsorption sites. They have replaced the metal sites near the corners with carbon atoms and got similar density plots. This implies the reason for having strong adsorption sites near the corners is not the open metal sites but the geometry of the structure.

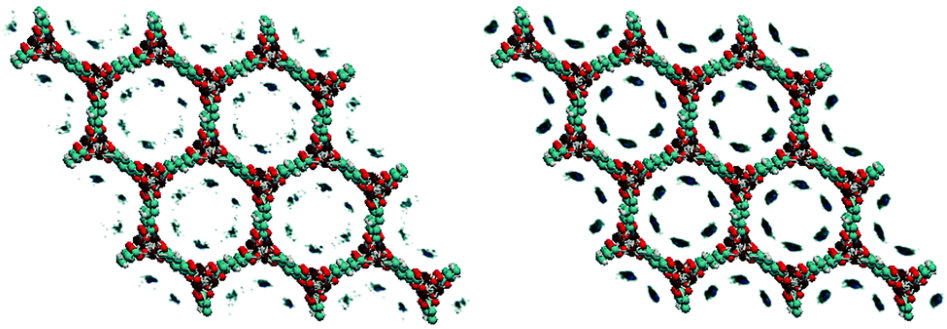

Figure 10. Xe density plots in Co-MOF-74 using PBE-D2 based FF at 292 K at 10^{-4} bar (left) and 10^{-3} bar (right).

In Figure 11, Xe density plot in ZIF-8 acquired at 308 K and 0.1 bar using PBE-D2 based FF is demonstrated where Xe occupies sites near cage windows and the cages

themselves. There is not an obvious preference of the former sites over the latter sites for Xe. Since the density plots obtained with other FFs are similar, they are not shown.

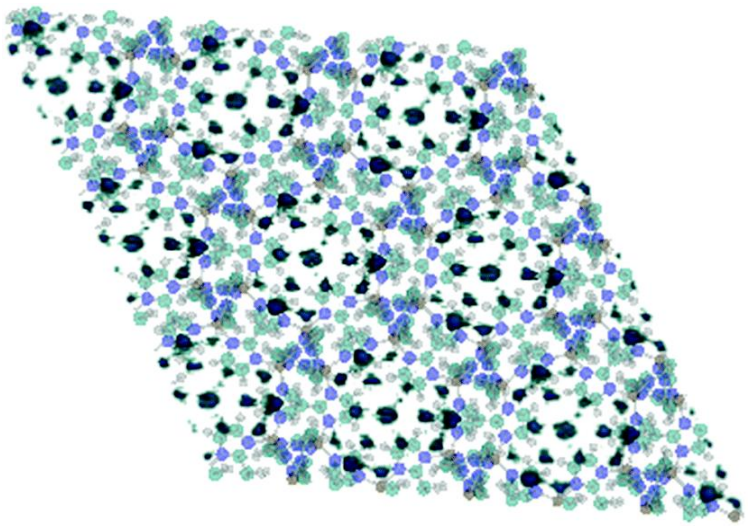

Figure 11. Xe density plots in ZIF-8 using PBE-D2 based FF at 308 K and 0.1 bar. (The framework is shown transparent for clarity.)

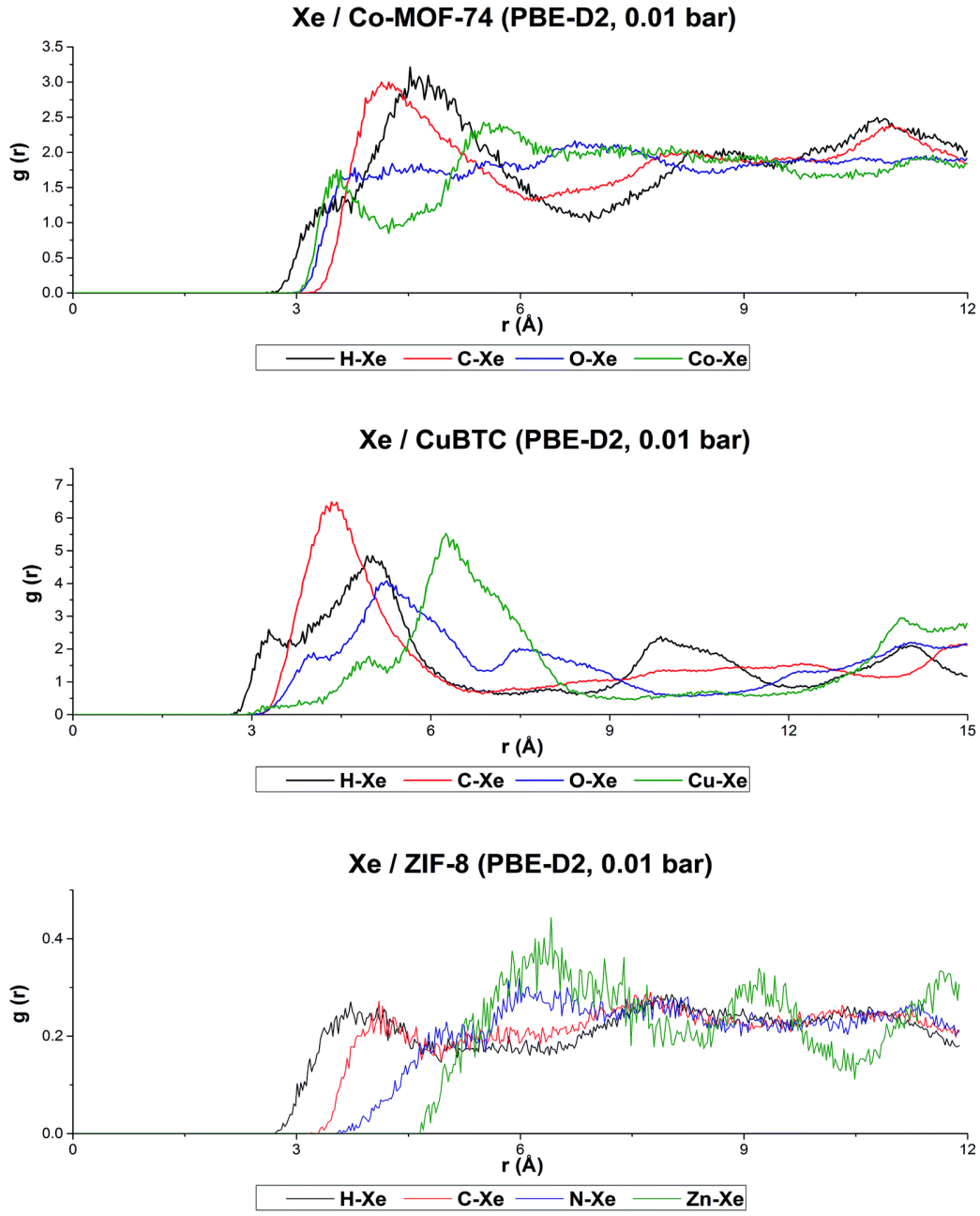

Figure 12. RDFs acquired with PBE-D2 based FFs for Xe adsorption in Co-MOF-74 (292 K, 0.01 bar), Cu-BTC (308 K, 0.01 bar), and ZIF-8 (308 K, 0.01 bar).

In Figure 12, RDFs for Xe-framework atoms are demonstrated for Co-MOF-74, Cu-BTC and ZIF-8 with PBE-D2 based FFs. Other RDFs are not shown since the conclusions are similar. In contrast to CH_4 adsorption in Cu-BTC[152], there is no preferential

Xe binding to the metal sites in any MOF, including the ones having open metal sites (Cu-BTC, and M-MOF-74). For M-MOF-74, Xe atoms are equidistant to different types of framework atoms. Although, the primary preferential adsorption sites are determined as sites near pore corners (metal atoms), adsorbates are not solely close to metals. For the case of Xe adsorption in Cu-BTC, it is found that Xe atoms are closer to ligand atoms than to metal atoms. This does not agree with the case of methane adsorption in Cu-BTC where methane strongly interacts with Cu atoms at close distances (~3 Å). For Xe adsorption in ZIF-8, adsorbates are farther away from Zn compared to other types of atoms which is due to the preferential adsorption near cages and windows but not near Zn atoms.

3.6 Conclusions

First principles based FFs are developed for Ar and Xe adsorption in MOFs based on the interaction energies of a combination of random and GCMC configurations. Non-bonded interactions are modeled as the summation of dispersion and polarization terms where the latter has very small contribution (~1%). The ab-initio based FFs can describe the DFT energies successfully with an average deviation of 2 to 3 kJ/mol at most. The experimental isotherms are compared with the ones generated with the DFT-based FFs and UFF. It has been observed that there are cases where a DFT-based FF can describe the experimental adsorption uptakes very well. However, none of them can describe the intermolecular interactions accurately for all adsorbate-adsorbent systems studied, implying none of them can be used to screen a large set of MOFs. By comparing the deviations of simulations from the experimental uptakes at 1 bar, UFF is determined to be the best FF in terms of prediction of loading while PBE-D2 based FF performance is slightly worse. In spite of a very good performance of vdW-DF2 based FFs in ZIF-8 and

Cu-BTC up to 20 bar, they do not have the same prediction qualities for M-MOF-74 in the low pressures (up to 1 bar). On average, vdW-DF2 based FFs are the third best FFs and vdW-DF based FFs had the worst performance of all overpredicting the experiments significantly. Due to standard deviations in performance of FFs, UFF, PBE-D2, and vdW-DF2 based FFs can be thought of having similar prediction qualities. The discrepancies between the experimental samples and the perfect structures used in the simulations can cause some of the deviations observed in this study, however, scaling the surface area of the structures does not make the deviations vanish for the whole pressure range.

CHAPTER 4

SELECTIVE CONTAMINANT REMOVAL FROM AMBIENT AIR WITH FUNCTIONALIZED UIO-66

4.1 Introduction

Air filtration is becoming a more important research topic because of increased environmental pollution of human activities. Basically, there are two approaches to enhance air quality, gas capture at the source before its release and contaminant capture from ambient air.[153] Adsorbent based solutions can be promising for both purposes. Conventionally, activated carbon is used for many separations since it has favorable interactions for organic species, however it is not good at capturing smaller and polar adsorbates.[154] Although zeolites can be found commercially in the market, they do not perform well in humid conditions, which leads researchers to search for better materials.[155]

MOFs are promising candidates for air filtration since they have high pore volume, surface area, and pore size tunability.[156-158] Contrary to conventional adsorbents, the chemistry in MOFs can be adjusted for/against a specific adsorbate by functional groups having various sizes, polarities, and affinities.[159-162] On the other hand, a disadvantage of MOFs compared to zeolites is their low thermal, hydrothermal, and chemical stabilities.[163-165] Since in a realistic scenario, air will be humid, the coadsorption of water and contaminants, where water adsorption may degrade the adsorbent, will be a serious issue that should be taken into consideration. Thus, ideally, an adsorbent should possess favorable chemistry for a toxic gas, high selectivity of that gas over water, and stability in humid air.[156]

Since toxic gases can have various chemical properties, adsorbents should ideally be functionalizable to enhance their interactions with particular species.[166] One of the widely studied MOFs is UiO-66 since it is readily functionalizable, regenerable[167, 168] and has high thermal[169, 170], mechanical[171, 172], water[167, 169], chemical stability[173-175]. The high thermal and chemical stability of it is attributed to Zr blocks, high coordination number of Zr, strong binding between inorganic blocks and the linker, and strong Zr-O bonds.[163, 170, 171, 176-182] It has been shown that UiO-66 can preserve its stability even after strongly acidic (pH=1) or basic (pH=14) environment treatments.[183]

There are many experimental studies demonstrating the incorporation of functional groups into UiO-66 involving amino, azide, halide, nitro, hydroxyl, methyl, and carboxylic acid.[163, 184-197] In Garibay et al.'s experimental work[189], UiO-66 is functionalized with naphthalene, –Br, $-NO_2$, and $-NH_2$ and their stabilities are tested. It is shown that the materials functionalized with the first two functional groups have similar stabilities to the parent UiO-66 while the other two functional groups cause reduced stability. Jasuja et al.[198] have worked on NH_3 adsorption on UiO-66 functionalized with –OH, $-(OH)_2$, $-NO_2$, $-NH_2$, $-SO_3H$, and $-(COOH)_2$ and determined that UiO-66 materials functionalized with $–SO_3H$ and $-(COOH)_2$ can adsorb less ammonia than the materials functionalized with -OH, and $-NH_2$ which is ascribed to reduced pore space in the former two materials. Considering the high stability of UiO-66 and shapes of the breakthrough curves, it is concluded that a chemical reaction of ammonia is unlikely to have happened. In Cmarik et al.'s work[199], adsorption of CO_2 and H_2O in UiO-66, UiO-66-NH_2, UiO-66-NO_2, UiO-66-Naphyl, and UiO-66-$(OCH_3)_2$ is studied and UiO-66-NH_2 is determined to be the best material for vacuum swing adsorption for dry operation. Hu et al.[200] have experimentally tested the CO_2

adsorption performance of several functionalized UiO-66 structures and shown UiO-66-$(COOH)_2$ to have high CO_2 working capacity, although it also captures considerable water at low pressures. Nik et al.[201] have demonstrated amine functionalized UiO-66 to have higher CO_2 adsorption than the parent one at 35°C. Similarly, Huang et al.[202] have determined UiO-66 materials functionalized with $-NO_2$, $-NH_2$, and $-(CH_3)_2$ to possess higher CO_2 adsorption than parent UiO-66. Jasuja et al.[203] have revealed that the incorporation of $-CH_3$ group into UiO-66 enhances CO_2 uptake and decreases water adsorption at low pressure. In another study of Jasuja et al.[204], functionalizing UiO-66 with $-(CH_3)_2$ reduces water uptake by almost 50% compared to the parent material while enhancing interactions with CO_2. Biswas et al.[159] synthesized functionalized UiO-66-R (R = NH_2, NO_2, OH, CH_3, and $(CH_3)_2$) and measured their CO_2 uptake to be higher than bare UiO-66. The sulphonic acid group also improves CO_2 adsorption as shown by Foo et al[188]. Kim et al.'s work[180] has shown that functionalization of UiO-66 with $-NH_2$, -OH, and $-(OH)_2$ leads to enhanced water adsorption at low relative humidity compared to the bare UiO-66. Schoenecker et al.[205] have also demonstrated that amine functionalized UiO-66 has larger affinity towards water than the bare UiO-66.

These experimental works suggest UiO-66 is a readily functionalizable material that can show promise in air separation applications. Computationally, Kim et al.[157] screened 21 functional groups such as metal carboxylates, hydroxyls, amines etc. using clusters representative of UiO-66 backbone to investigate ammonia adsorption in both dry and humid conditions. They have determined -COOCu, -COOAg functional groups to be the best performers in humid conditions while -COOCu has the largest ammonia affinity. However, the drawback of that study is they cannot incorporate the effect of confinement

to the binding energies with their cluster-based approach. Yu et al.[206] have partially considered this by developing FFs at the MP2 level for ammonia adsorption in MIL-47, IRMOF-1, -10 and -16 including -OH, -C=O, -Cl, and -COOH functional groups and using the resulting FFs in GCMC to simulate ammonia adsorption isotherms. Although there is significant recent progress in deriving quantum chemistry based accurate FFs to predict adsorption in porous structures[24, 129, 130, 132, 207-210], such methods necessitate relatively expensive calculations for each adsorbent to be studied. Since taking such an approach for multiple adsorbates in more than 30 functionalized materials would require very expensive calculations, a more computationally feasible method is used in this study where fewer quantum chemistry calculations are performed.

In this study, both cluster and periodic models are used to understand the effect of various functional groups on NH_3, H_2S, CO_2, and H_2O affinities in functionalized UiO-66 structures to identify the most promising functional groups for selective capture of air contaminants in humid conditions.

4.2 Computational Methods

In this section, details of electronic structure calculations employing cluster and periodic models are discussed. For the clusters, both MP2 and DFT level calculations are used whereas for the perodic models, only PBE-D2 level calculations are performed. In cluster calculations, the affinity rankings of functional groups at the MP2 and PBE-D2 levels are shown to have good correlation, which means the DFT level calculations can present qualitatively reliable results.

The cluster models are formed by attaching functional groups, which are listed in Table 3, to C_6H_5 or C_6H_4 (for bifunctional groups such as $-I_2$). For the functional groups

that are in written italics, optimization of the periodic models are problematic and results for those are not discussed for periodic models.

Table 3. Functional Groups Investigated.

-$(CF_3)_2$	-CH_3	-F_2
-$(CH_3)_2$	-Cl	-I
-$(COOH)_2$	-$(Cl)_2$	-I_2
-$(NH_2)_2$	-CN	-NCO
-$(OCH_3)_2$	-CHO	-NH_2
-$(OH)_2$	-*COOAg*	-NO_2
-Br	-*COOCu*	-NO_3
-$(Br)_2$	-COOH	-OCH_3
-C=O	-*COOK*	-OH
-CF_3	-*COOLi*	-OOH
-CH_2-F	-*COONa*	-SO_3H
-CH_2-NH_2	-F	-$(NO_2)_2$

Binding energy is defined as

$$E_{binding} = E_{adsorption\ complex} - E_{adsorbate} - E_{adsorbent} \quad (4.1)$$

where $E_{adsorption\ complex}$, $E_{adsorbate}$, and $E_{adsorbent}$ represent the total energy of the adsorption complex, the total energy of the isolated gas species, and the total energy of the isolated adsorbent, respectively. The bifunctional groups are attached to the ring in *para* positions with respect to each other. Cluster calculations are performed for all gas species except CO_2. The initial sites of adsorbates with respect to UiO-66 models are chosen in a way where favorable interactions, such as hydrogen bonding, Lewis acid-base interactions and combination of them, are possible.[157] Beginning from those initial positions, all atoms in the cluster and periodic models are relaxed. For cluster optimizations, MP2 and DFT level (PBE-D2, M06-2X) calculations are done using GAUSSIAN 09[89]. For all atoms, the

6-31+G(d,p) basis set is used, except silver atoms for which the LanL2DZ effective core potential is utilized. Basis set superposition error (BSSE)[211] effects are incorporated in the binding energies using the counterpoise method.

The periodic structure for bare UiO-66 is obtained from Jasuja et al.[203] in which hydrogen(s) of the benzene rings are replaced with the desired functional groups. The calculations are done in VASP with $1 \times 1 \times 1$ unit cells having 14-15 Å in each direction. At the PBE-D2[76] level, a 400 eV kinetic energy cutoff is used with one Γ-centered *k*-point. The optimizations are done with the total energy and ionic force convergence criteria of 1×10^{-4} eV and 3×10^{-2} eV/Å, respectively. In the optimizations, both lattice parameters and atomic positions are optimized. UiO-66 is a 3D cubic structure with $Zr_6O_4(OH)_4$ metal clusters connected with 1,4-benzenedicarboxylate linkers.[184] As shown in Figure 13, it includes two types of cages, one centric octahedral (11 Å) and eight tetrahedral (8 Å) cages, connected with triangular windows (6 Å).[212]

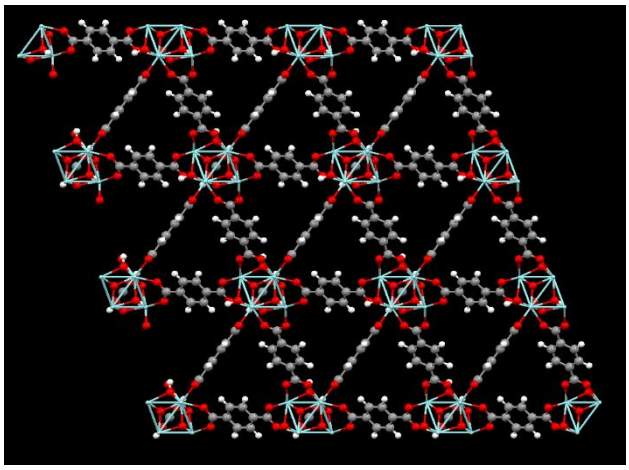

Figure 13. UiO-66 viewed along the *a* axis. (H, C, O, and Zr are depicted in white, gray, red, and cyan, respectively.)

To assess the potential of adsorbents for the selective adsorption of an adsorbate in humid conditions, the binding energy differences between a particular adsorbate and water is calculated. For instance, for the determination of potentially top-performer functional groups for selective ammonia adsorption in humid conditions, $\Delta = BE_{NH3} - BE_{H2O}$ is considered. Negative Δ values mean that particular functional group is likely to be selective towards ammonia over water and vice versa. Although evaluating only this parameter means disregarding the synergistic effects of adsorbates during a coadsorption, it is useful for screening many materials at a high-level.

4.3 Results

In the cluster calculations, firstly, MP2 and DFT level energies are compared to see if lower level DFT calculations can qualitatively describe the adsorption of gases of interest in functionalized UiO-66. A good correlation between MP2 and DFT level energies implies that DFT functional can be used to understand the confinement effects in the periodic models.

NH_3, H_2S, and H_2O adsorption energies are determined for the unfunctionalized and [-$(CF_3)_2$, -$(CH_3)_2$, -$(COOH)_2$, -$(NH_2)_2$, -$(OCH_3)_2$, -$(OH)_2$, -Br, -$(Br)_2$, -C=O, -CF_3, -CH_2-F, -CH_2-NH_2, -CH_3, -Cl, -$(Cl)_2$, -CN, -CHO, -COOAg, -COOCu, -COOH, -COOK, -COOLi, -COONa, -F, -F_2, -I, -I_2, -NCO, -NH_2, -NO_2, -NO_3, -OCH_3, -OH, -OOH, and -SO_3H] functionalized phenyl rings using MP2 and DFT (PBE-D2, and M06-2X) level calculations. Figure 14 shows the lowest binding energies calculated at MP2 and DFT levels. Those values are tabulated in Tables 15-17 in Appendix B.

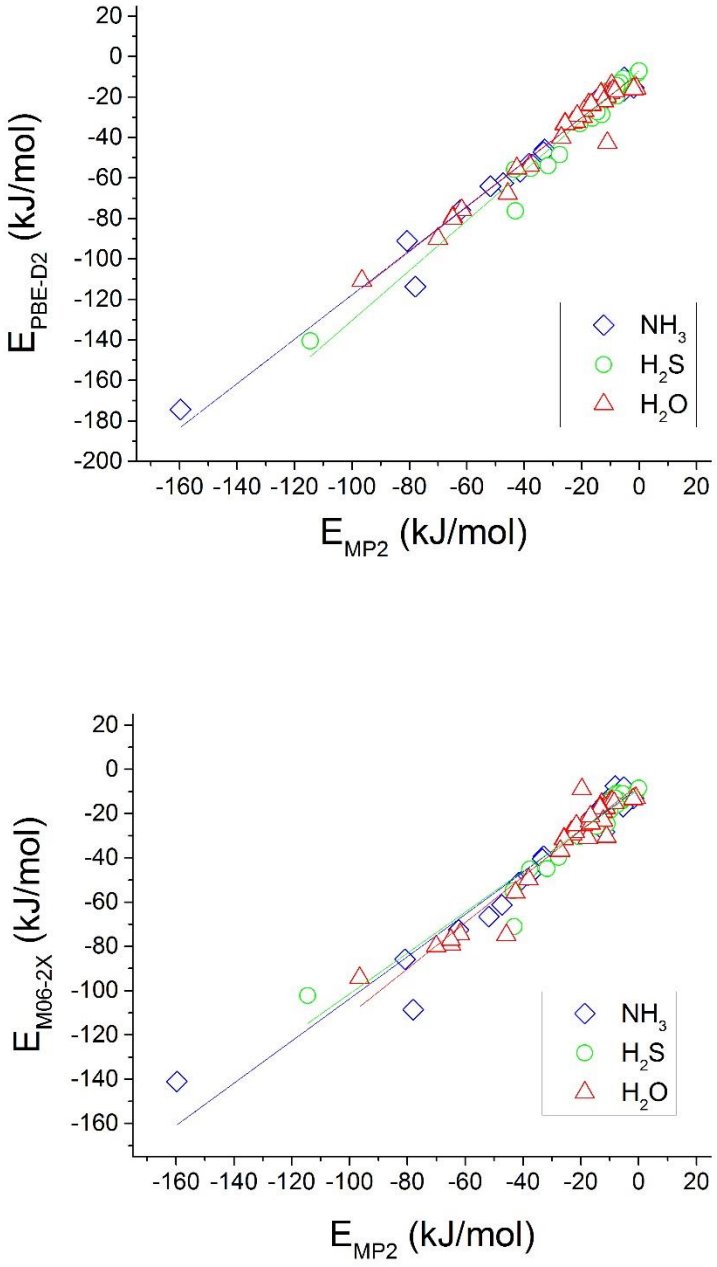

Figure 14. Binding energy comparisons for NH_3 (blue), H_2S (green), and H_2O (red) in functionalized phenyl rings at MP2 and DFT levels. The upper and bottom plots include PBE-D2 and M06-2X calculations, respectively. Lines correspond to the linear fits to the data.

The binding energies of NH_3, H_2S, and H_2O at MP2 and PBE-D2 levels are highly correlated, with R^2 values of 0.98, 0.97, and 0.96, respectively. Although the M06-2X binding energies also have good correlation with MP2 energies (R^2 = 0.95, 0.93, and 0.93 for NH_3, H_2S, and H_2O, respectively), it is weaker than the correlation between PBE-D2 and MP2 energies. Thus, if the ranking is done at computationally less expensive DFT level, PBE-D2 is slightly better than M06-2X at ordering the affinities of functionalized UiO-66 structures for the adsorbates studied. Although PBE-D2 can qualitatively give accurate results for the gas binding energies in functionalized UiO-66 materials, it should be noted that there is a systematic difference between MP2 and PBE-D2 energies. Considering the slopes of linear fits (1.10, 1.23, and 1.1 for NH_3, H_2S, and H_2O, respectively) in Figure 14, PBE-D2 results have bigger binding energy difference between any two materials for any of the adsorbates than MP2. To assess the quality of predictions of PBE-D2 for the binding energies, MAD between MP2 and PBE-D2 energies are calculated and found to be 10.7, 10.7, and 10.8 kJ/mol, respectively, for NH_3, H_2S, and H_2O. These figures imply that although PBE-D2 can give qualitatively satisfying results, it should be kept in mind that quantitatively there are significant differences in binding energies at these two different levels.

Having seen the satisfactory correlation between MP2 and PBE-D2 energies, the next thing that is investigated is whether PBE-D2 can reliably order the gas affinities of functionalized UiO-66 materials in periodic models as well. Figure 15 and Tables 18-20 show the comparisons between the lowest binding energies of NH_3, H_2S, and H_2O obtained at PBE-D2 level in clusters and periodic models. As seen in Figure 15, the correlations are poor for all adsorbates (R^2 = 0.504, 0.101, and 0.389 for NH_3, H_2S, and H_2O, respectively).

For all three gases, the cluster calculations cannot predict the material which has the highest interactions in the periodic models. For instance, for ammonia adsorption, the adsorbent that is predicted to have the strongest interactions by periodic calculations is UiO-66-OOH which is the third material in terms of binding strength in cluster calculations.

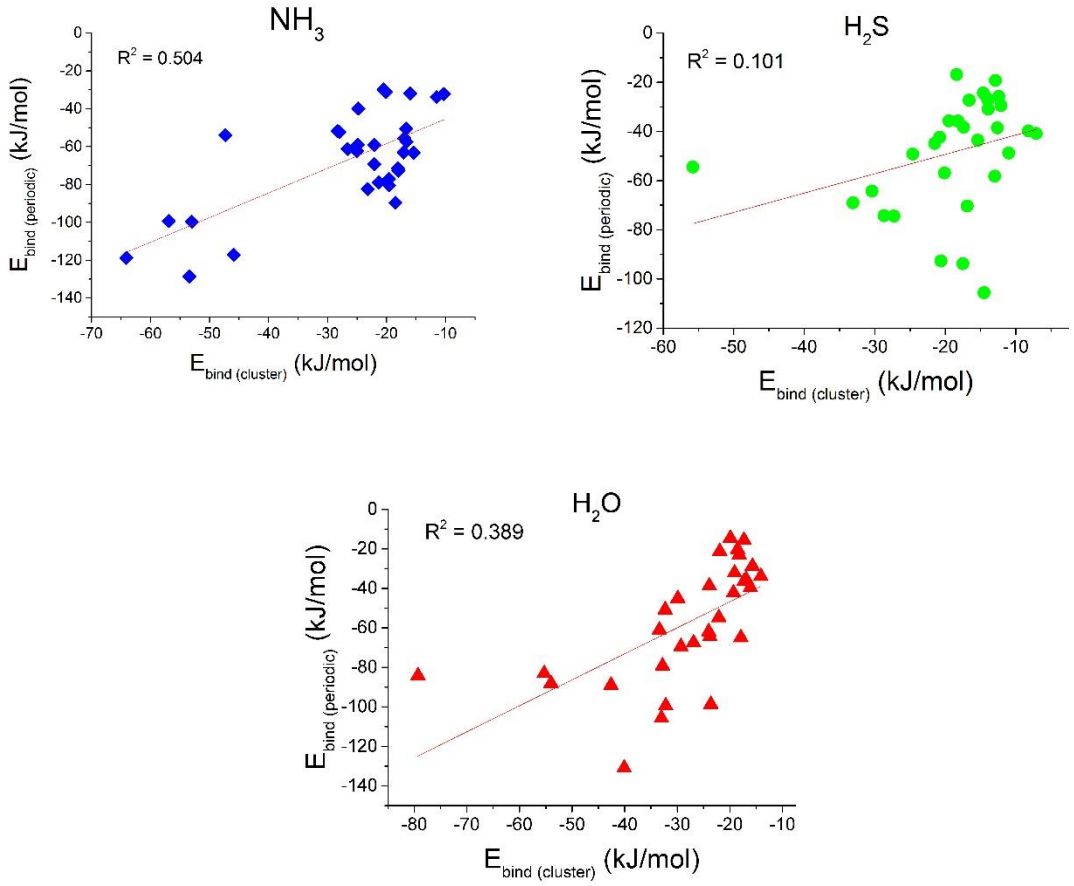

Figure 15. Comparison of most favorable binding energies of NH_3 (top left), H_2S (top right), and H_2O (bottom) in cluster and periodic models of bare and functionalized UiO-66 structures.

Such results are expected since in the cluster calculations, the long range dispersion effects cannot be incorporated. To understand the effect of dispersion in the binding energies in the periodic models, the molecules are placed approximately to the center of

octahedral cages and the vdW contribution to $E_{binding}$ is extracted. As can be seen from Figure 16 and Table 21, in many cases the dispersion effect is significant and can make up almost 50% of the total adsorption energy for NH_3, H_2S, and CO_2. Still, if the dispersion contributions were similar for all cases, then the ordering of the materials could be done with cluster calculations. It is also observed that dispersion energy can change significantly depending on the functional group attached. For instance, for H_2S, the dispersion energy can vary by about 20 kJ/mol. All together, these results imply that the use of PBE-D2 in periodic models to rank the materials is more reliable than cluster-based calculations. It is also important to note that the rankings obtained in this way would be strongly correlated with MP2 based rankings for periodic models if they could be done.

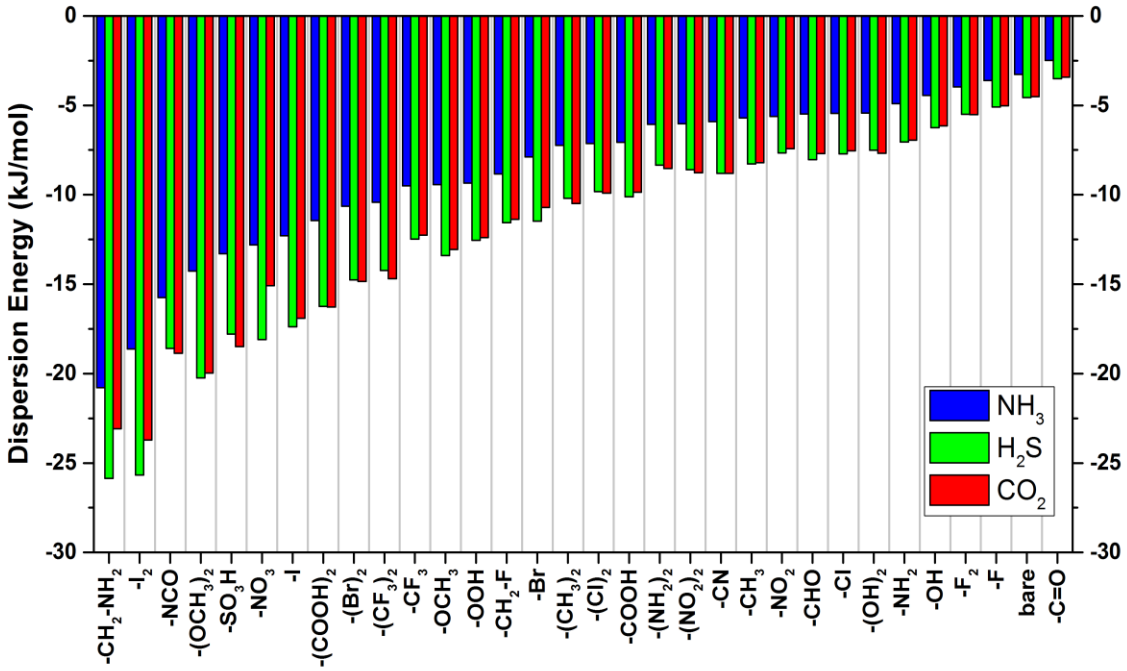

Figure 16. Dispersion interactions at the octahedral cage centers of functionalized UiO-66 structures obtained at PBE-D2 level using periodic models.

The following discussions detail the PBE-D2 calculation results in periodic models of functionalized UiO-66 for the evaluation of selective separation using these materials. Although determining binding energies of single molecules is important, it is not enough by itself to evaluate materials for practical adsorption applications. Generally, NH_3 and H_2S can be found in the environment together with H_2O, which can also interact strongly with a specific material. Thus, the relative binding strength of a material should be determined for selective separation purposes. Evaluations based on relative adsorption strength of gases, which is obtained by investigating individual binding sites, can be useful for adsorption cases where the bulk phase concentrations of gases of interest are low. In Figure 17, the relative binding energies of NH_3 and H_2O and the NH_3 binding energies are depicted for each functionalized UiO-66 material using periodic calculations at the PBE-D2 level. The materials with the functional groups on the left of this figure are the most selective ones for NH_3 over H_2O while the ones on the right are vice versa. A few materials can bind NH_3 more favorably than H_2O by up to 60 kJ/mol. For preferential NH_3 adsorption, $-(Cl)_2$ and $-F_2$ functionalized materials have the biggest potential. On the other end, two functionalized UiO-66 structures can bind H_2O stronger than NH_3 by more than 20 kJ/mol. The $-(OCH_3)_2$ and $-CH_2-NH_2$ functionalized materials bind H_2O 21.7 and 37.1 kJ/mol more favorably than NH_3. Looking at the trends of the net NH_3 binding energies and the differences between NH_3 and H_2O binding energies, it is clear that strong NH_3 binding does not correlate with preferential NH_3 binding over H_2O. For example, the -OOH functionalized UiO-66 has the strongest NH_3 binding but since it has similar H_2O binding energies, it is not ranked as one of the most promising materials for selective separation of

NH_3 in humid conditions. However, there are also a few examples where there is both strong NH_3 binding (over 100 kJ/mol) and a preferential NH_3 binding over H_2O.

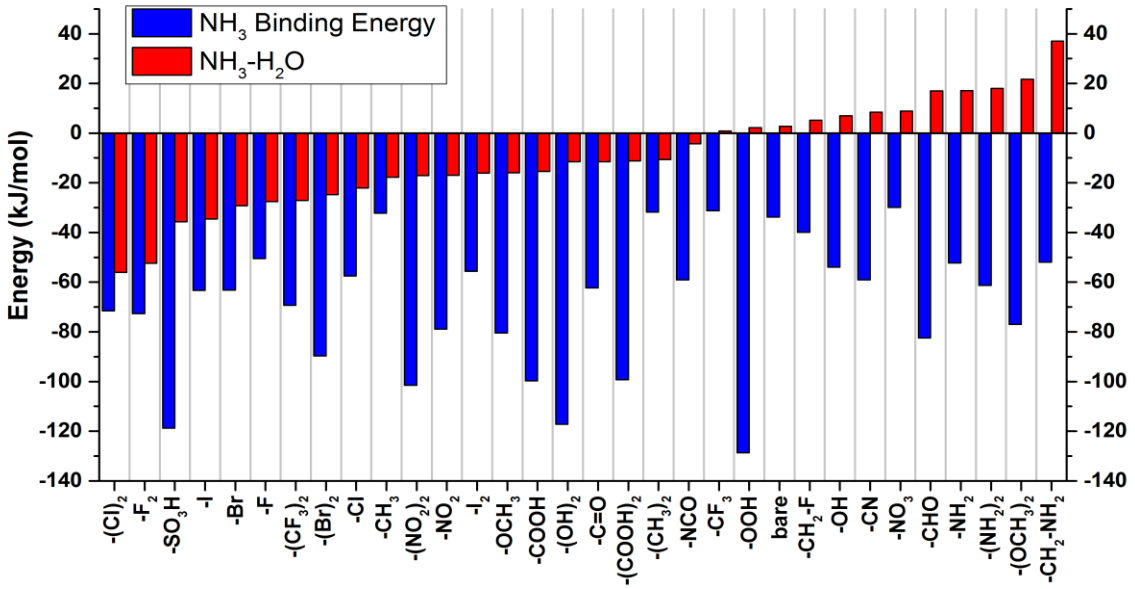

Figure 17. Relative binding energies of NH_3 and H_2O (red) and net NH_3 binding energies (blue) in functionalized periodic UiO-66 materials at PBE-D2 level.

In Figure 18, the relative H_2S and H_2O binding energies are shown as well as net H_2S binding energies. It is determined that all materials except eight of them have preferential H_2O binding over H_2S. Importantly, three materials bind H_2O more than 30 kJ/mol stronger than H_2S. As seen for NH_3, the strong H_2S adsorption does not always lead to high relative binding strength differences between H_2S and H_2O.

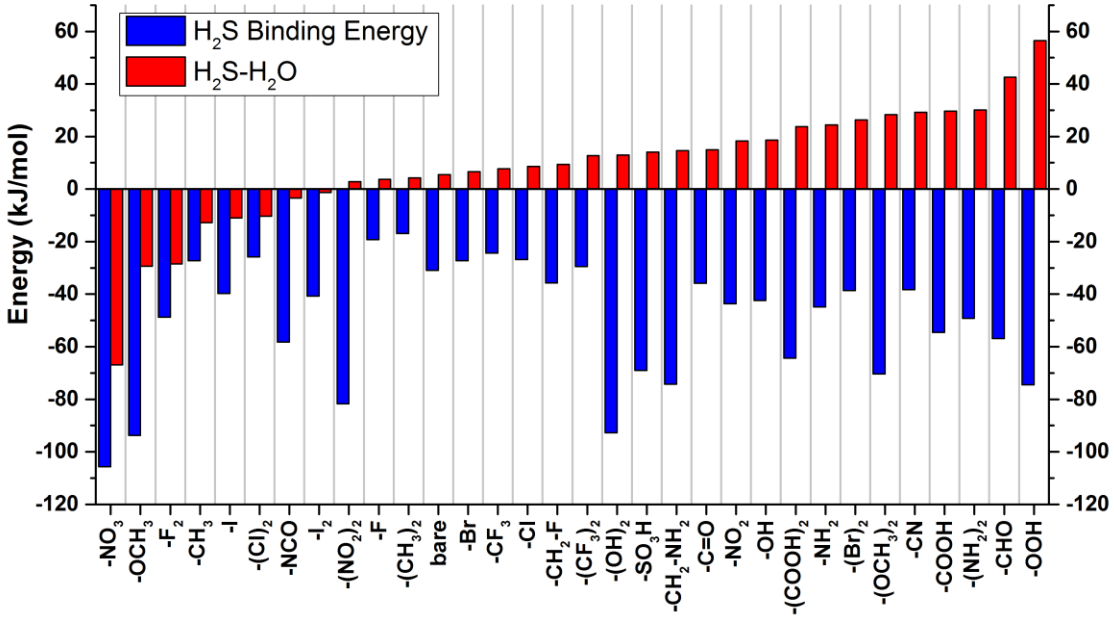

Figure 18. Relative H_2S binding energies compared to H_2O (red) and net H_2S binding energies (blue) in functionalized periodic UiO-66 materials calculated with PBE-D2.

In Figure 19, the relative CO_2 and H_2O binding energies and net CO_2 adsorption energies are illustrated where it is seen that most of the materials have preferential H_2O binding over CO_2. The top performers in terms of preferential CO_2 binding over H_2O are -F_2, -$(Cl)_2$, and -CH_3 functionalized UiO-66 structures. Especially, the performance of the -F_2 functionalized UiO-66 is remarkable since it binds CO_2 more strongly than H_2O by more than 25 kJ/mol.

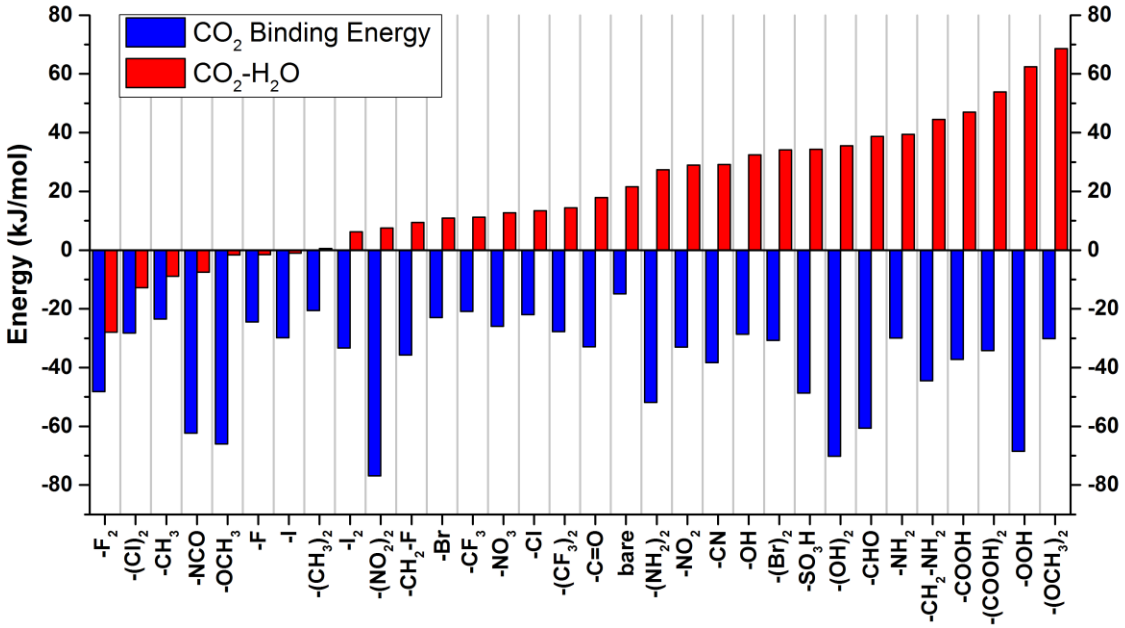

Figure 19. Relative CO_2 binding energies compared to H_2O (red) and net CO_2 binding energies (blue) in functionalized periodic UiO-66 materials calculated with PBE-D2.

To have a qualitative analysis of experimental and simulation results, the binding energies and experimental heats of adsorption are compared, noting they are not precisely the same quantities.[136] Jeremias et al.[213] have determined loading averaged heat of adsorption of water in UiO-66 and UiO-66-NH_2 as 41.3 and 89.5 kJ/mol by using the Clausius-Clapeyron equation at 25°C and 40°C. In our DFT calculations, the lowest binding energies of water for these two materials are found to be 36.5 and 69.4 kJ/mol, which implies a qualitative agreement between simulation and experimental results. Still, it should be noted that it is not clear, in general, how much difference should be between the loading averaged experimental heat of adsorption and the lowest binding energy. Similarly, Cmarik et al.[199] have determined heat of adsorption of CO_2 in UiO-66-NH_2 and UiO-66-NO_2 at infinite dilution as -28 and -32 kJ/mol using the Clausius-Clapeyron

equation at 298, 308, and 318 K. On our end, the calculations have shown the most favorable binding energies as -29.9 and -33.0 kJ/mol for those two structures, respectively. Despite the apparent close agreement between experimental and theoretical results, Fang et al.[136] have demonstrated that CO_2 heat of adsorption in zeolites is about 7-8 kJ/mol less favorable than the most favorable binding energy. This implies the difference between the simulated and experimental values are similar however the calculated values underpredict CO_2 binding strength. Due to limited available experimental data, the comparisons that can be made are not many but it can be concluded that PBE-D2 results are qualitatively in agreement with experimental data.

The evaluation of the relative binding energies to rank materials is adequate if the adsorption happens solely with a competitive mechanism for low concentration bulk phase gas mixtures. However, the possible synergistic effects can lead to considerable deviations from this analysis for many mixtures especially mixtures including water.[214] For instance, it has been reported that CO_2 adsorption in amine-involving materials increases with the presence of water.[215, 216] On the other hand, NH_3 adsorption in MOFs including UiO-66 derivatives decreases due to water coadsorption.[198, 217] Still, our analysis is useful for an initial screening of materials which can further be investigated in detail.

For the UiO-66 derivatives where there are bulky functional groups, diffusional limitations may come into play due to restricted pore space. To estimate which materials may suffer from diffusional constraints, the largest cavity diameter (LCD) and pore limiting diameter (PLD)[32] values are calculated for each energy-minimized empty structure using zeo++[218]. Although a more detailed analysis including pore flexibility[219, 220] should

be made to fully understand molecular diffusion, these pore size calculations based on rigid structures can give a rough idea about whether the diffusion limitations can be significant.

The PLD and LCD values for each functionalized UiO-66 material are shown in Table 4 listed from smallest to largest PLD. 10 materials have PLD values less than 3 Å which implies diffusion limitations can arise for large adsorbates such as H_2S. Such materials should be investigated further to fully understand molecular diffusion.

Table 4. PLD and LCD values of each functionalized UiO-66 structure.

	LCD (Å)	**PLD(Å)**		**LCD (Å)**	**PLD(Å)**
-$(CF_3)_2$	5.1	2.1	**-CF_3**	7.2	3.2
-$(OCH_3)_2$	5.8	2.2	**-COOH**	6.3	3.2
-$(COOH)_2$	5.9	2.2	**-OOH**	7.5	3.3
-I_2	6.5	2.2	**-C=O**	9.8	3.3
-NCO	7.4	2.4	**-CHO**	7.0	3.3
-$(Br)_2$	7.0	2.8	**-I**	7.6	3.4
-SO_3H	6.8	2.8	**-CH_2-F**	7.6	3.5
-$(NO_2)_2$	5.4	2.9	**-CN**	7.2	3.5
-CH_2-NH_2	7.5	2.9	**-F_2**	7.6	3.6
-$(CH_3)_2$	7.0	2.9	**-Br**	7.6	3.6
-NO_3	6.4	3.0	**-Cl**	7.6	3.7
-$(Cl)_2$	7.0	3.0	**-CH_3**	7.6	3.8
-$(NH_2)_2$	7.3	3.0	**-NH_2**	7.6	3.8
-NO_2	6.3	3.0	**-OH**	7.6	3.9
-$(OH)_2$	7.6	3.1	**Bare UiO-66**	8.6	4.0
-OCH_3	7.0	3.2	**-F**	7.6	4.0

4.4 Conclusions

Using both cluster and periodic models, more than 30 functionalized UiO-66 derivatives are computationally screened to comprehend their potentials for competitive adsorption of NH_3, H_2S, CO_2, and H_2O. Firstly, the binding energies calculated at different

levels of theory are compared using cluster models. It has been found that there is a good correlation between binding energies calculated using DFT functionals and more accurate MP2 results. This has revealed that DFT calculations can be employed to order materials with similar accuracies to the MP2 calculations with less computational time. Then, the binding energies calculated at PBE-D2 level using cluster and periodic models are compared. It should be noted that such a comparison cannot be made with MP2 calculations since they are computationally infeasible for periodic systems. The ranking of materials obtained using periodic models is different than that of cluster models where strong confinement effects play a role. It is also seen that such effects cannot be incorporated into cluster models using a simple energy correction.

Lastly, the competitive binding of NH_3, H_2S, and CO_2 with H_2O is evaluated by the periodic PBE-D2 calculations which do not take into account the synergistic effects. For the selective adsorption of NH_3, H_2S, and CO_2 over H_2O, [-$(Cl)_2$, -F_2, -SO_3H, -I, -Br, -F, -$(CF_3)_2$, -$(Br)_2$, -Cl, -CH_3, -$(NO_2)_2$, -NO_2, -I_2, -OCH_3, -COOH, -$(OH)_2$, -C=O, -$(COOH)_2$, -$(CH_3)_2$ and -NCO], [-NO_3, -OCH_3, -F_2, -CH_3, -I, -$(Cl)_2$ and -NCO] and [-F_2, -$(Cl)_2$, -CH_3 and -NCO] functionalized materials are determined to be the top performers, respectively. Most of the functionalized UiO-66 structures bind NH_3 stronger than H_2O whereas only several materials bind H_2S and CO_2 stronger than H_2O.

The approach presented here is useful to screen tens of functionalized UiO-66 materials for the selective adsorption of air contaminants in humid conditions. The results reported are reliable enough to guide experimental efforts for synthesizing smaller number of materials. However, it should be noted that, for the best performing materials, more

detailed investigations may be required to fully understand adsorption characteristics such as coadsorption and possible diffusional limitations due to attached functional groups.

CHAPTER 5

UNDERSTANDING PHASE INSTABILITIES IN LAYERED MATERIALS USING DFT*

5.1 Introduction

In this chapter, the phase transitions in two materials are studied, namely $CuInP_2S_6$ and $CuInP_2Se_6$. A brief background on these materials is given in this section. Although there are only several compounds with stoichiometry $M_2P_2X_6$ (M = Sn, Pb, Eu, and Sr) in 3-D, the layered chalcogenophospates are more common.[221] Transition metal thio/selenophosphates (TPS) are vdW layered solids where the typical chemical formulas are $M^{4+}[P_2X_6]^{4-}$, $[M^{2+}]_2[P_2X_6]^{4-}$, and $M^{1+}M^{3+}[P_2X_6]^{4-}$, M and X representing metal and S/Se atoms.[222-225] One of the important features of TPS is the strong ionicity of the bonds between metals and P_2X_6.[226]

$CuInP_2S_6$ is a ferrielectric material having a ferroelectric transition temperature (T_c) of 315 K, meaning it shows ferroelectric properties at room temperature.[227] It crystallizes into a monoclinic structure (space group Cc) based on ABC close-packed stacking of the chalcogens where two-thirds of the octahedral cages of S are occupied by metal atoms.[226, 228] In each layer, Cu, In and P-P are located in triangular patterns.[229] The layers in $CuInP_2S_6$

---

* Portions of the results described in this chapter have been previously published in Michael A. Susner, Alex Belianinov, Albina Y. Borisevich, Qian He, Hakan Demir, David S. Sholl, Panchapakesan Ganesh, Douglas L. Abernathy, Michael A. McGuire, and Petro Maksymovych, "High Tc layered ferrielectric crystals by coherent spinodal decomposition", ACS Nano, 2015, 9, 12365-12373

are linked with each other by weak vdW interactions.[230] The ferrielectricity occurs perpendicular to the layer planes due to displacement of Cu^{+} and In^{3+} cations away from octahedral cages in opposite directions.[229] The transition from a paraelectric to a ferrielectric phase occurs through a first-order phase transition.[231] The Cu and In atoms move off-center by 1.6 Å and 0.2 Å in antiparallel directions while P-P pairs move slightly (on the order of 0.01 Å).[232] The off-centering of metals are ascribed to a second-order Jahn-Teller effect.[221] In the layered structure, P_2S_6 networks absorb the structural distortions and confine the cations to displace in antiparallel directions.[221, 229] These displacements lead to a symmetry reduction from C2/c to Cc.[233] Recently, T_c of In-rich $CuInP_2S_6$ samples was determined to be slightly higher than 315 K, up to 330 K.[226] For $CuInP_2S_6$, there have been X-ray, dielectric and calorimetric investigations revealing the polar character of the structure.[229, 234, 235] It is reported that 2-D ferrielectric geometries are found in all known $M^{2+}PS_3$ and $A^{+}M^{3+}P_2S_6$ species having d^{10} cations.[236-240]

$In_{4/3}P_2S_6$ can be considered as a parent material of $CuInP_2S_6$ that is monoclinic (space group $P2_1/c$) at room temperature and rhombohedral ($R\bar{3}h$) at very high temperatures (> 945 K). To satisfy the charge neutrality, there are unoccupied octahedral sites (□), which are half of the In sites in number, giving a formula of $In_{4/3}\square_{2/3}P_2S_6$. The symmetry of the P_2S_6 constituents are the same in both $CuInP_2S_6$ and $In_{4/3}P_2S_6$, however, the number of In^{3+} ions and existence of Cu atoms create the differences between these two materials.[226]

$CuInP_2Se_6$ is another structure in chalcogenophosphate class of materials. Its high and low temperature structures have been identified to have space groups P-31c and P31c by single-crystal X-ray diffraction.[231] There are many similarities between the structural

dynamics of $CuInP_2Se_6$ and $CuInP_2S_6$. For $CuInP_2Se_6$, the motions of Cu^+ and In^{3+} ions do not compensate the dipole moments created and a ferroelectricity occurs as seen in $CuInP_2S_6$. The Cu^+ ions off-center by about 1.2 Å perpendicular to the layer while the In^{3+} ions move slightly (0.2 Å). The reduced In^{3+} mobility is attributed to the absence of a lone electron pair.[225] Due to the higher covalence of the bonds (stronger attraction) in $CuInP_2Se_6$ than sulfide analog, Cu^+ ions displace less in $CuInP_2Se_6$ compared to $CuInP_2S_6$.[233] This may lead to a shallower potential energy relaxation for Cu^+ in $CuInP_2Se_6$ than $CuInP_2S_6$.[241] The net dipole moment in one slab induces a corresponding moment in the adjacent slab. The ferroelectricity created in $CuInP_2Se_6$ is ascribed to a second-order Jahn-Teller coupling which includes Cu d-orbitals and Se orbitals.[223]

There have been various experimental efforts aimed at identifying structural changes in $CuInP_2Se_6$. Some of the findings of those studies are not always consistent with each other as noted below. The dielectric investigations revealed two phase transitions for $CuInP_2Se_6$: a second-order phase transition at 248 K and a first-order phase transition at 236 K.[242] However, calorimetric studies determined a phase transition between 220 and 240 K.[223] Broadband dielectric analysis identified a second-order phase transition at 226 K.[233] The change of lattice parameters of $CuInP_2Se_6$ with respect to temperature was also studied and it was found that as the structure is cooled both *a* and *c* parameters are reduced and the *a* parameter attains a local minimum at 226 K.[233] This observation is contrary to the anomalous increases in the lattice parameters of $CuInP_2S_6$ as it is heated.[232]

Structures similar to $CuInP_2S_6$ have also been studied previously $CuCr_{1-x}In_xP_2S_6$[243, 244] and $CuInP_2(Se_xS_{1-x})_6$[245]. A significant reduction of T_c under room temperature is

observed (to 200 K or below), however, making it impossible to see their ferroelectric properties around room temperature.

5.2 Computational Methods

For all DFT calculations, VASP version 5.3.5 has been used. For the calculations of $Cu_xIn_yP_2S_6$, $CuInP_2S_6$ and $In_2P_3S_9$ structures are acquired from the Inorganic Crystal Structure Database (ICSD) having ICSD numbers 79219 and 1700, respectively. Four structures of $Cu_xIn_yP_2S_6$ with excess In atoms with respect to Cu atoms in a stoichiometric structure were generated. The excess In ratios were 12.5, 15, 20, and 30%. To obtain those structures, firstly, all Cu atoms of $CuInP_2S_6$ are replaced with In atoms. Then, half of the In atoms are randomly selected and converted to Cu. Afterwards, a number of Cu atoms are randomly selected and removed to create vacancies while some of the Cu atoms are randomly converted to In to have excess In. The creation of vacancies are crucial to establish the charge neutrality of the system; without them, excess In charges would make the system positively charged. Finally, randomly converted In atoms that were not centered between the layers have been centered manually to have the final structures of $Cu_xIn_yP_2S_6$. All of the structures have been optimized using PBE-D2 functional where the symmetries are kept fixed (Cc: $CuInP_2S_6$, $P2_1/c$: $In_2P_3S_9$, and P1: $Cu_xIn_yP_2S_6$). The optimizations were done using the conjugate gradient method with the total ionic force convergence criterion is 1×10^{-2} eV/Å. For $CuInP_2S_6$ ($3 \times 2 \times 1$ supercell) and $In_2P_3S_9$ (unit cell), $1 \times 2 \times 2$ and $3 \times 4 \times 2$ k-point meshes are used, respectively. For total charge densities, finer FFT grids (three times denser in each direction) are acquired and used as reference for the Bader partitioning to calculate Bader charges of the valence charge density.

The $CuInP_2Se_6$ structure was also obtained from ICSD for which k-point convergence has been satisfied at $4 \times 4 \times 2$ for the unit cell. To get the relaxed structure (P31c), only atomic positions are equilibrated and the lattice parameters are kept fixed. The total ionic force convergence criterion for optimizations is 1×10^{-2} eV/Å which is achieved through conjugate gradient method. Phonopy[246] is used for phonon calculations and generating modulated structures. The non-analytical term correction[247, 248] is added to dynamical matrix at $q \to 0$. The spontaneous electric polarization is calculated using Berry phase or modern theory of polarization, which is described elsewhere.[249, 250]

5.3 Instability in $CuInP_2S_6$

In this work, the thermodynamic phase stability of excess In containing $CuInP_2S_6$ structures is studied computationally. It is assumed that the pure end phases are $CuInP_2S_6$ and $In_{4/3}P_2S_6$. Five random $Cu_xIn_{(4-x)/3}P_2S_6$ structures are generated as described in Section 5.2 for each Cu concentration studied. The miscibility of $Cu_xIn_{(4-x)/3}P_2S_6$ is investigated by calculating the enthalpy of mixing (per P_2S_6) at the PBE-D2 level as follows

$$\Delta H_{mixing} = E_{Cu_xIn_{(4-x)/3}P_2S_6} - \left(xE_{CuInP_2S_6} + \frac{1-x}{3}E_{In_4P_6S_{18}}\right) \quad (5.1)$$

where E_i, x denote the total energy of material i and Cu concentration. The free energy of mixing is calculated by

$$\Delta F_{mixing} = \Delta H_{mixing} - T\Delta S_{mixing} \quad (5.2)$$

where

$$\Delta S_{mixing} = -2k_B[C_{Cu}lnC_{Cu} + C_{In}lnC_{In} + C_{vac}lnC_{vac}] \quad (5.3)$$

with C_y represents the concentration of species y (Cu, In and vacancy, vac). To have chemical phase separation, a positive enthalpy of mixing, positive free enthalpy of mixing

at 0 K, is required which creates a solubility gap in phase diagram. In contrary, a negative enthalpy of mixing implies a single phase alloying is energetically favorable. In Figure 20, the free energy of mixing at 0 K is plotted with respect to Cu concentration.

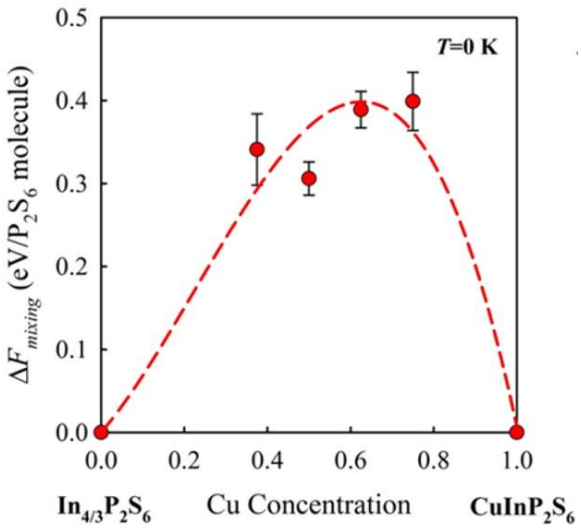

Figure 20. Enthalpy of mixing for excess In containing $CuInP_2S_6$ structure.

The endpoints on the x axis show the pure end members, $In_{4/3}P_2S_6$ (at zero Cu concentration) and $CuInP_2S_6$ (at Cu concentration of 1). By definition, the enthalpy of mixing for pure end phases is zero. The calculated values for intermediate Cu concentrations shown in Figure 20 are the averages of the enthalpy of mixing calculated for five structures at each concentration, with standard errors shown with error bars. The dotted line corresponds to a third order polynomial fitted to the calculated values. It can be seen that over a wide range of Cu concentration the enthalpy of mixing is positive, favoring chemical phase separation.

By fitting ΔF_{mixing} to a polynomial and taking its second derivative with respect to x, the spinodal decomposition temperature, T_s, can be estimated.[251] In Figure 21, T_s is plotted with respect to Cu concentration where endpoints are the same as in Figure 20.

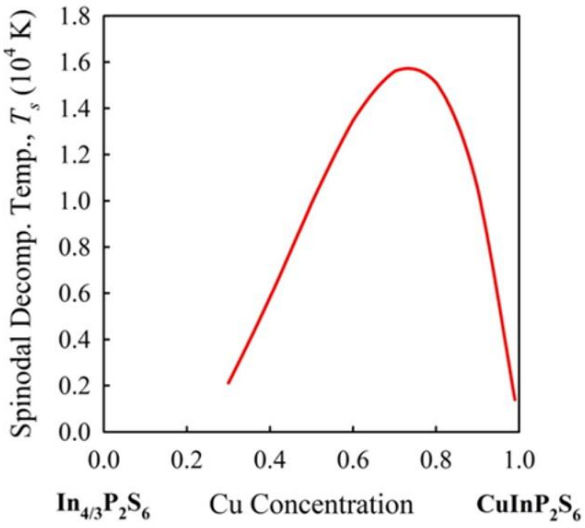

Figure 21. The calculated spinodal decomposition temperatures for excess In containing $CuInP_2S_6$ structure.

Below T_s, the second derivative of the free energy of mixing with respect to Cu concentration is negative, which means $CuInP_2S_6$ and $In_{4/3}P_2S_6$ can grow. One thing to note in Figure 21 is the high values of T_s. These high values, as seen in other spinodal mixtures[251], imply the phase separation can occur at growth temperatures of the experimental samples. To understand the effect of electrostatics on the positive enthalpy of mixing, Bader charges[252, 253] were assigned to the atoms and then Ewald summation[254] was performed using pymatgen[141]. A similar analysis was done with DDEC charges.[137-139] The electrostatics energy using both Bader and DDEC charges are indicated in Figure 22 where it can be seen that majority of the energy cost for the enthalpy of mixing is due to

the electrostatics. This suggests the immiscibility is related to the unfavorable electrostatic interactions in the alloy.

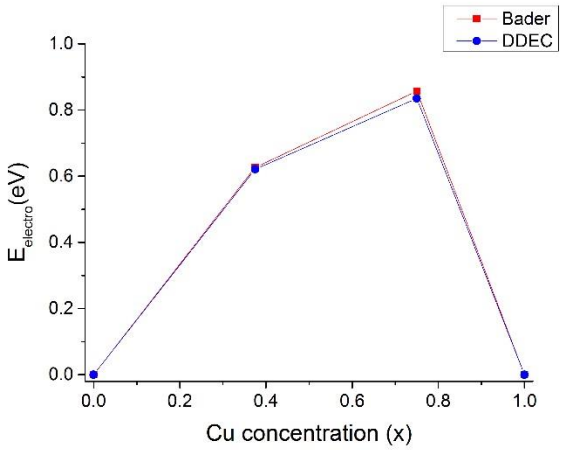

Figure 22. Electrostatic energies calculated using Bader and DDEC charges.

These computational results are supported by the Piezoresponse Force Microscopy (PFM) and energy-dispersive X-ray spectroscopy (EDS) analyses. Susner et al.[226] have demonstrated that for $Cu_{1-x}In_{1+x/3}P_2S_6$ with x~0.22, there are distinct regions of Cu and In rich phases, indicating the demixing experimentally. This demixing increased the ferrielectric transition temperature from 315 K (for $CuInP_2S_6$) to 335 K making In-rich $Cu_{1-x}In_{1+x/3}P_2S_6$ materials the highest temperature vdW gapped ferrielectric material. This implies that through compositional modification different phase transition properties can be obtained which can be useful for bulk nanostructuring of layered materials and creating new 2-D layered heterostructures.

5.4 Instability in $CuInP_2Se_6$

The vibrational properties of $CuInP_2Se_6$ were investigated to elucidate the material's dynamical instability/stability of it. Figure 23 shows the ICSD structure (centrosymmetric) and the energetically more stable structure. The biggest difference between these two structures is the off-centering of the Cu atoms from the middle of the layers. The energetically favorable structure has been obtained by following the eigenvector at the lowest frequency of the Γ point, which will be discussed more in the coming paragraphs (it corresponds to the energy minimum structure in Figure 25).

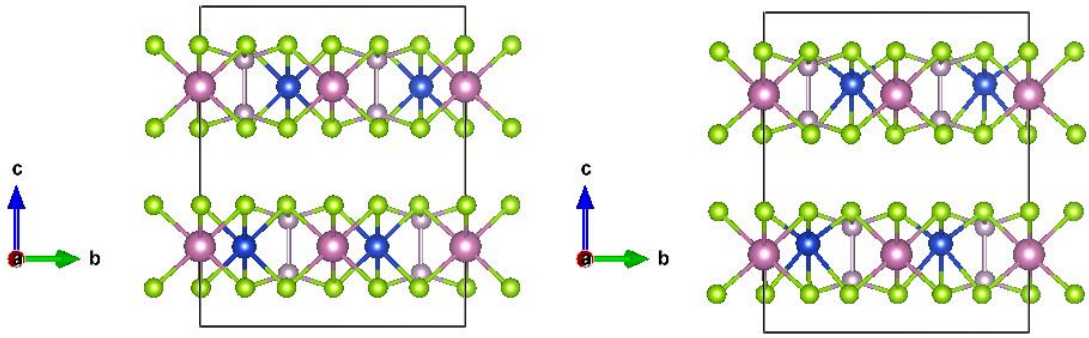

Figure 23. Centrosymmetric (left) and energy minimum (right) structures of $CuInP_2Se_6$ (Cu, In, P and Se are shown in blue, purple, light purple and green, respectively.).

Table 5 lists the lattice parameters and the angles of the ICSD structure of $CuInP_2Se_6$. All of the $CuInP_2Se_6$ structures have the same lattice parameters since during the introduction of distortions or optimizations, they are kept fixed.

Table 5. Structural parameters of $CuInP_2Se_6$.

Unit Cell Parameters	**a,b,c (Å) / α,β,γ (°)**
$CuInP_2Se_6$	6.392, 6.392, 13.338 / 90.0, 90.0, 120.0

As discussed in section 2.4, the phonon theory leads to a final eigenvalue-eigenvector problem where frequencies and eigenvectors can be found after determining the dynamical matrix. The dynamical matrix has been obtained by phonon calculations performed on $2 \times 2 \times 1$ supercells of $CuInP_2Se_6$ and the frequencies and the corresponding eigenvectors (distortions) have been calculated for zone center and zone boundaries.

Table 6 lists the imaginary frequencies (in meV) at Γ and the high symmetry k-points (M, L, A) which can cause structural instability. Due to high symmetry, some of the frequencies are degenerate.

Table 6. Imaginary frequencies at zone center and boundaries.

Frequency (meV)	Γ	M	L	A
ω_1	-4.64	-4.56	-4.53	-4.39
ω_2	-4.40	-4.51	-4.53	-4.39
ω_3	-1.19	-2.25	-2.22	-0.67
ω_4	-1.19	-2.22	-2.22	-0.67
ω_5	-	-	-	-0.67
ω_6	-	-	-	-0.67

Figure 24 depicts the vibrational DOS of the centrosymmetric $CuInP_2Se_6$ structure. Below zero frequency, this figure shows the soft modes that can cause the phase instability. It also contains the positive frequency information which can be used to get other vibrational motions that do not cause any phase transition. To find out which motions can cause energy stabilization, for each of the imaginary frequency listed in Table 6, the eigenvectors are introduced into the centrosymmetric structure in varying magnitudes to get a potential energy surface at zone center and the boundaries. The energy profile of the structures distorted with the eigenvectors corresponding to the imaginary frequencies at the Γ point is discussed here, since the biggest energy lowering is seen at the zone center. The energy profiles obtained at the frequencies determined for zone boundaries can be seen in Appendix C which have similar profiles. Figure 25 shows the energy profiles obtained by following the corresponding eigenvectors at the Γ point where from top left to bottom right the frequencies increase. It is clear that only the lowest two frequencies can lower the energy compared to the starting point which is the middle of the curves (displacement magnitude=0). Since this study is focused on phase instability, the vibrations at the other two frequencies are not investigated any further.

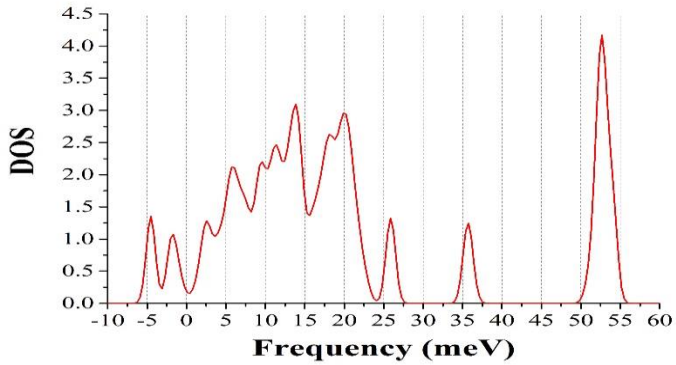

Figure 24. DOS plot for the centrosymmetric phase of $CuInP_2Se_6$.

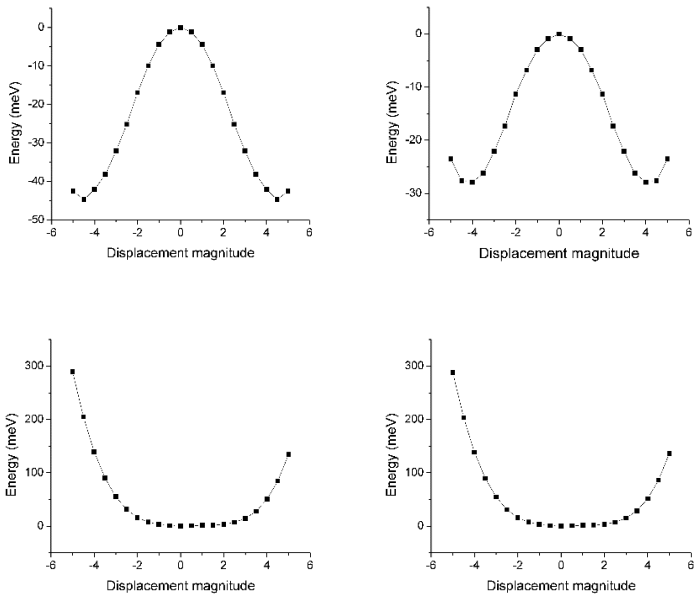

Figure 25. Energy profiles at increasing negative frequencies of Γ point (from top left to bottom right) with respect to displacement magnitude for fully distorted $CuInP_2Se_6$ structure.

To understand whether the motions of the specific kinds of atoms dominate the energy stabilization, the eigenvectors were modified for two scenarios. In one of them, only the metal distortions are kept while the non-metal distortions are taken as zero. In the other scenario, the opposite has been done to see the effect of only non-metal distortions. In Figure 26, it can be seen that at the lowest two frequencies, the energies of the distorted structures never go below that of the centrosymmetric structure, contrary to the observations made for the fully distorted structure in Figure 25. Similarly, in Figure 27, it is observed that if only the non-metal distortions are introduced to the centrosymmetric system, the energy stabilization cannot be achieved. This implies that there must be a collective motion to have the energy stabilization and the collective effect cannot be approximated by only metal or non-metal distortions. Likewise, only Cu and only In

distortions have been applied to the centrosymmetric structure and similar graphs are obtained (not shown).

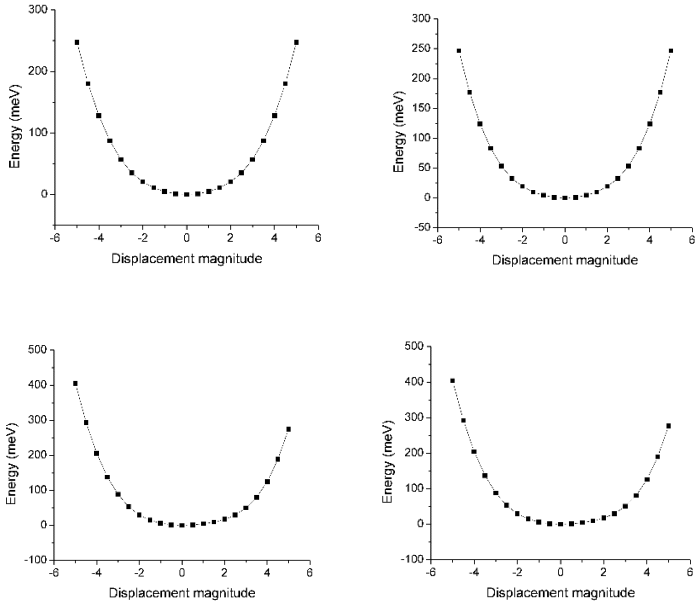

Figure 26. Energy profiles at increasing negative frequencies of Γ point (from top left to bottom right) with respect to displacement magnitude for $CuInP_2Se_6$ structure where only metals are distorted.

Since ferroelectricity is of interest to this study, the motions that stabilizes the centrosymmetric structure are characterized further. The eigenvectors obtained at the lowest frequency of the Γ point are plotted together with the atoms of the structure in Figure 28. Here, since there are multiple layers, for clarity, the atoms away from the point of view are drawn whiter, i.e. the farthest away atom is depicted in white, and the closest atom to the reader is in the original color of the atom type. It can be seen that at the lowest imaginary frequency the Cu atoms displace away from their starting positions (middle of the layers)

and Se networks rotate. The significant metal off-centering cause a polarization to arise in the structure, thus, this motion is classified as a ferroelectric motion.

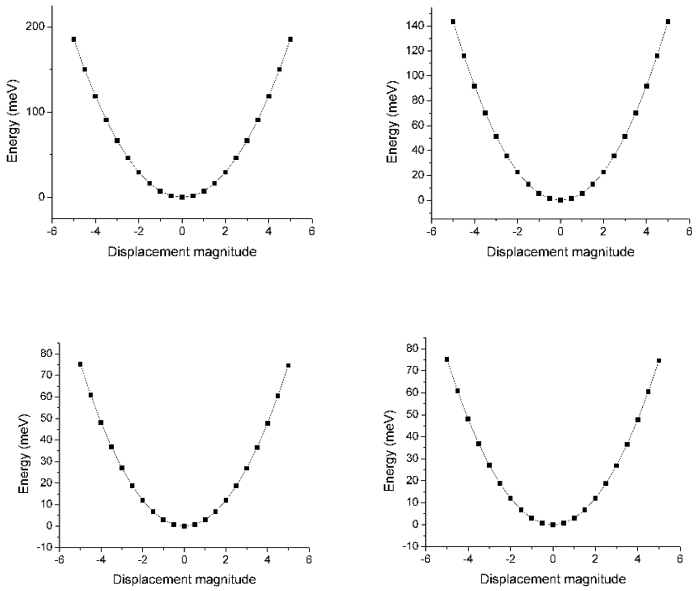

Figure 27. Energy profiles at increasing negative frequencies of Γ point (from top left to bottom right) with respect to displacement magnitude for $CuInP_2Se_6$ structure where only non-metals are distorted.

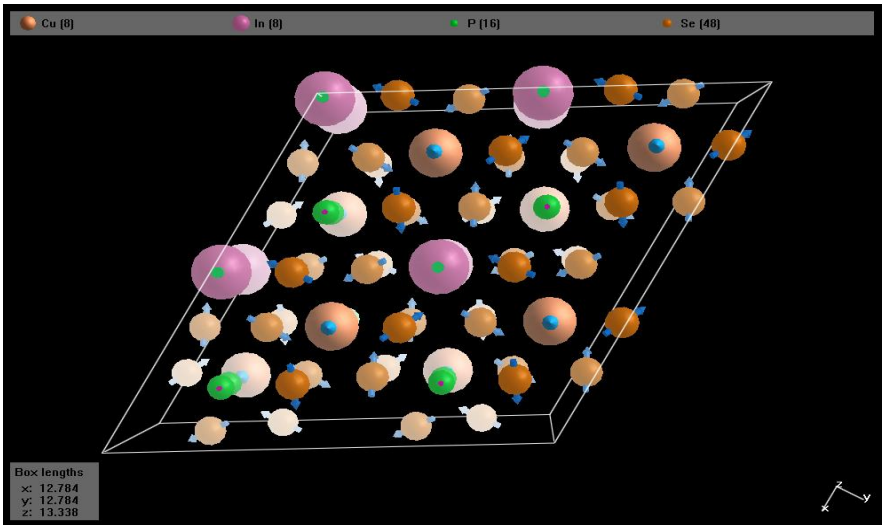

Figure 28. Distortions at the lowest frequency of the centrosymmetric phase causing ferroelectricity.

A similar plot has been obtained for the second lowest frequency at the Γ point and shown in Appendix C. The motions at the second lowest frequency have antiferroelectric properties and no macroscopic polarization is induced. To provide an evidence of the ferroelectric character of the vibrational motions at the lowest frequency at the zone center, the macroscopic polarization is obtained along z axis (the direction towards which Cu atoms off-center) for each distorted structure and the centrosymmetric structure. These values are plotted in Figure 29 with respect to the displacement magnitude. As expected, the centrosymmetric structure does not have any macroscopic polarization while the distorted structures have increasing polarization with the increasing magnitude of the motions.

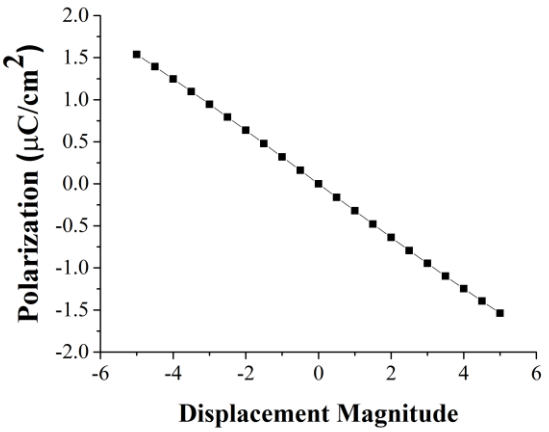

Figure 29. Polarization in z direction with respect to displacement magnitude at the lowest frequency.

Although it is interesting to prove the instability of the centrosymmetric $CuInP_2Se_6$, it is also desirable to have an approach to get a dynamically stable structure. The energy minimum structure obtained in Figure 25 is thermodynamically more favorable than the

centrosymmetric structure, however, due to the imaginary frequencies in its vibrational DOS (shown in Figure 30), it is not dynamically stable.

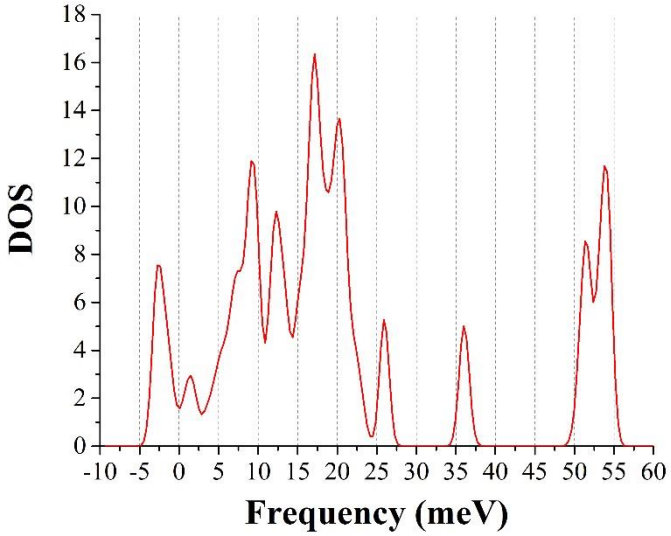

Figure 30. DOS of the energy minimum structure.

The approach we have taken to get the dynamically stable structure is as follows: Firstly, we have introduced only the Cu off-centering motions from the eigenvectors corresponding to the lowest frequency at the Γ point. Then, all of the atoms are relaxed while keeping the cell parameters fixed. Phonon calculations have been performed on the resulting relaxed structure. The band structure of this relaxed (ordered) structure is shown in Figure 31 where it is clearly seen that along different k-vectors there is no imaginary frequency proving the dynamical stability of the structure. It is also worth noting that the resulting structure has the experimentally observed space group (P31c).

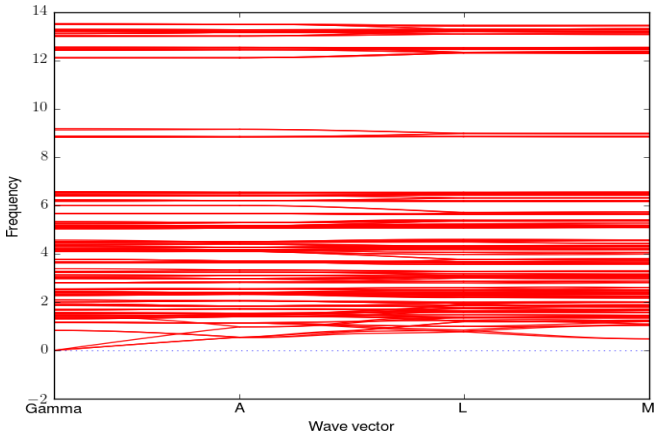

Figure 31. Band structure of the relaxed ferroelectric phase of $CuInP_2Se_6$ ($2 \times 2 \times 1$ supercell).

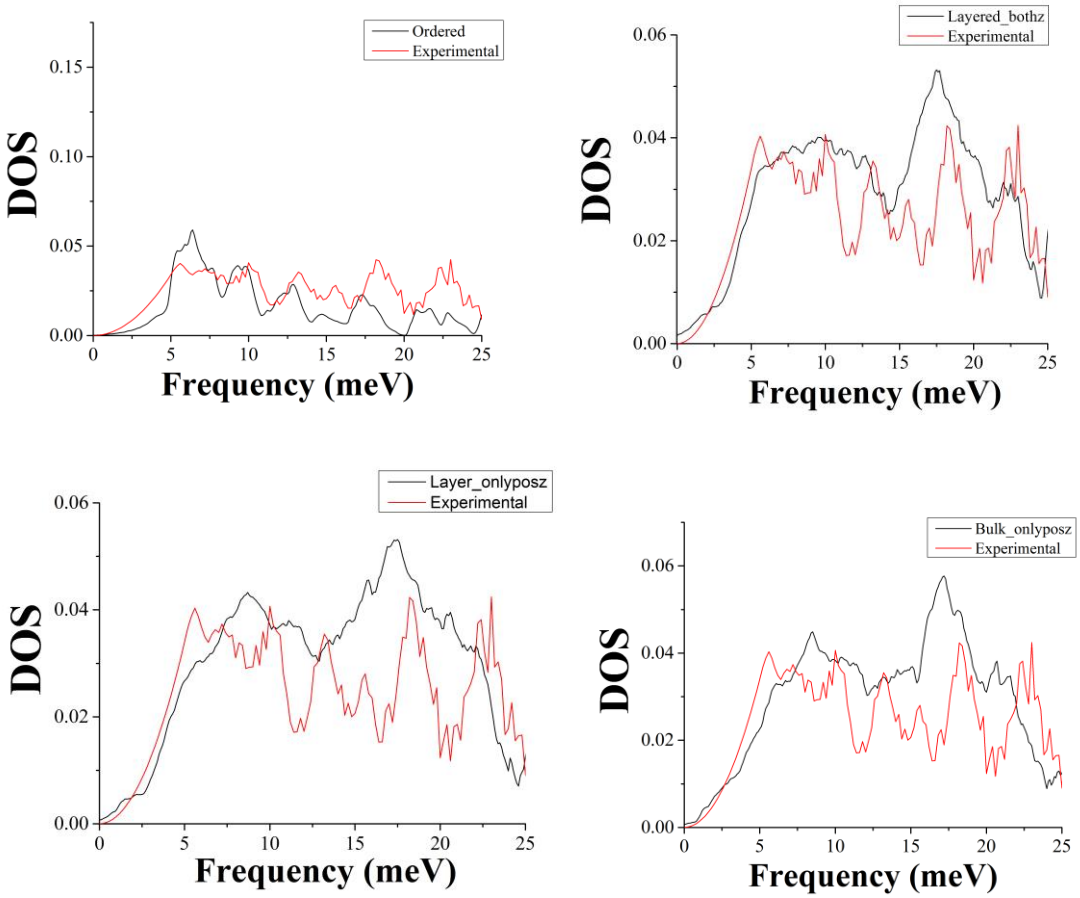

Figure 32. Comparison of the experimental and simulated DOS for ordered and disordered $CuInP_2Se_6$ (up to 25 meV).

One important issue about the centrosymmetric $CuInP_2Se_6$ structure is that in the reported experimental structure there is a 50% disorder possibility for the metal sites. To simulate the effect of this disorder on the phase stability, three different kinds of structures are obtained. In the first kind of them, the Cu/In disorder is introduced in the whole bulk system meaning Cu and In sites are randomly exchanged. Then, Cu atoms are randomly displaced along +z and finally all atoms are relaxed. The resulting structure is called "bulk_onlyposz". For the second type of material, the Cu and In sites are randomly exchanged within each layer separately. Then, Cu atoms are displaced randomly along +z and lastly, all atoms are relaxed. The resulting structure is called "layer_onlyposz". The last type of structure is similar to the second type, the only difference is Cu atoms are displaced randomly along both +z and -z. This structure is called "layered_bothz". The phonon calculations have been made for these structures as well. The ineleastic neutron scattering data at 5 K (measured using the ARCS time-of-flight chopper spectrometer at the Spallation Neutron Source, at Oak Ridge National Laboratory[255]) is compared with the simulated data in Figure 32. It can be seen that the disordered structures have reasonable agreement with the experimental data. It should be noted that the "ordered" case has the best agreement and the disorder has caused some deterioration in the agreement with the experiments especially for the "layer_onlyposz" case. The full range of comparison can be found in Appendix C.

5.5 Conclusions

In the first part of this chapter, the chemical phase separation of In rich $CuInP_2S_6$ is discussed using thermodynamic principles and the quantities of enthalpy and free energy of mixing. The enthalpy and free energy of mixing are calculated at four different Cu

concentrations for which five randomly generated structures are used to average them. Through the calculated values, a third order polynomial is fitted and it has been found that over a wide range of Cu concentration, the enthalpy of mixing is positive, implying that the chemical phase separation is favorable. To characterize the phase separation, the spinodal decomposition temperature is obtained by taking the second derivative of the free energy of mixing with respect to Cu concentration. It has been determined that the spinodal decomposition temperature are on the order of 10^4 K, meaning the phase separation could be seen even at very high temperatures. To reveal the underlying cause of the positive enthalpy of mixing, the electrostatic energy is calculated for the same structures using Bader and DDEC charges. It has been seen that there is a large positive electrostatic interaction contributing significantly to the positive values of the enthalpy of mixing. It should also be stated that both Bader and DDEC charges have given almost the same results meaning the electrostatic contribution is not strongly dependent on the charge assignment method used. From an experimental point of view, this also implies growing an In rich $CuInP_2S_6$ will lead to demixing of it into pure end members of it. This effect has been seen in PFM and EDS images for $Cu_{1-x}In_{1+x/3}P_2S_6$ where x~0.22.[226]

The second part of the chapter is about understanding the vibrational dynamics of $CuInP_2Se_6$. Experimentally, it has been already shown that $CuInP_2Se_6$ goes through phase transition starting from high temperature structure (P-31c) and ending at the low temperature structure (P31c). The centrosymmetric structure (P-31c) is obtained from ICSD and phonon calculations are performed based on it to see if it is dynamically unstable as seen in experiments. The calculated vibrational DOS has shown soft modes implying the possible instability of the centrosymmetric structure. The imaginary frequencies are

obtained at both zone center and zone boundaries (M, L and A k-vectors). Since the largest energy stabilization is seen at the Γ point, a more detailed analysis has been made for distortions at the zone center. At the Γ point, the eigenvectors corresponding to each of the four imaginary frequencies are followed to generate the energy potential curve starting from the undistorted (centrosymmetric) structure. It has been determined that the lowest two frequencies cause energy stabilization. At the lowest frequency of the Γ point, it has been seen that the distortions have ferroelectric property where the most important motion is off-centering of Cu atoms. Together with it, the rotational motions of Se atoms are also seen. At this frequency, the centrosymmetric structure is distorted along the corresponding eigenvector and the polarization is calculated with respect to the increasing distortions. At the second lowest frequency, no ferroelectric character is seen. To understand the effect of metal and non-metal distortions on the stability of the structure, at each frequency, the corresponding eigenvector is modified so that it has either only metal or non-metal distortions in it. By distorting the centrosymmetric structure along these modified motions, separate energy potential curves are obtained, showing no instability with pure metal or non-metal motions. This implies the instability cannot be simplified as a consequence of pure metal or non-metal motions and there is a collective effect of all atoms causing the instability.

Although it is possible to have a structure more stable than the centrosymmetric one by following the eigenvector at the lowest frequency, investigating its vibrational DOS, it has been seen that energy minimum structure is dynamically unstable. The dynamically stable structure has been obtained by first off-centering Cu atoms and then relaxing all of the atoms. To see the effect of disorder in the structure, disorders are introduced in either

bulk or layer-wise. Then, all Cu atoms are randomly off-centered along z axis and finally all atoms are relaxed. The disordered and relaxed structure have shown dynamic stability. The vibrational DOS of the ordered and the disordered structures are compared with the experimental data and a decent agreement has been seen for all cases. This implies even if the structure is disordered in reality, it can still attain its dynamic stability and structural characteristics are similar to experimental sample.

CHAPTER 6

CONCLUSIONS & OUTLOOK

MOFs present huge opportunities in many areas, including gas capture, storage, sensing, catalysis etc. due to their high surface area, void fraction, and chemical tunability. One of the advantages of MOFs over conventional adsorbents is numerous combinations that can be made with many different linkers and metal centers. This gives rise to not only high pore volumes and pore sizes, but also different chemistry in the structures. Considering the functionalizable characteristic of linkers in MOFs, the affinities of MOFs towards/against a particular species can be tailored much easier than zeolites, activated carbon etc. It has been shown that MOFs can be relatively easily synthesized and today there are thousands of MOFs synthesized some of which are commercially available.[26, 256] Despite these advantages, it should be kept in mind that many MOFs have low structural stability.[256]

Since there are already a large number of existing MOFs and the number of theoretical and synthesized MOFs is increasing rapidly, it is not practical to test the performances of them experimentally for even a particular adsorbate. Considering the fact that there are many complex applications for which MOFs can be useful, evaluations of MOFs for a single adsorbate may not be sufficient and multiple adsorbates may have to be investigated in the same medium. All of these facts show that if it is desired to identify best performing materials for many applications, the experimental efforts will be time consuming. Thus, experimental studies are generally comprised of a number of materials and computational studies are key to expedite the search for best materials for a specific

application. Computational studies can also reveal phenomena that cannot be measured experimentally. Depending on the level of accuracy desired, computational studies can investigate tens, hundreds or even thousands of structural properties of materials.

Generally, computational studies on gas storage and separation in MOFs rely on generic FFs which are not specifically developed for MOFs. These studies span a range of molecules including CH_4, H_2, CO_2, N_2, noble gas etc. [24, 27, 257, 258] Although they may give satisfactory adsorption predictions in MOFs without open metal sites[259], these generic FFs cannot describe adsorbate-adsorbent interactions well in MOFs with open metal sites[149]. One of the possible advantages of ab-initio based FFs over generic FFs is that since the former is derived for specific adsorbate-MOF interactions, it is more likely to see ab-initio based FFs to be transferable to similar MOFs. Assuming the predictions of ab-initio based FFs are accurate enough, they could be better candidates to be used for MOF screening than generic FFs. Depending on the accuracy of ab-initio based FFs, the diffusion properties of top performing MOFs can also be studied.

In this study, we have derived first principles based FFs to predict noble gas adsorption in MOFs and compared their prediction performances with experimental uptakes. To our knowledge, the developed FFs are the first FFs in the literature that are specifically targeting noble gas-MOF interactions. Until now, for noble gas adsorption, generally, polarization effects are neglected in the classical simulations. One of the strengths of this work is that FFs are developed by taken into account both dispersion and polarization effects. Although there are approaches to fit FF terms to partitioned DFT energy components including polarization[16, 207], our approach utilizes the total DFT energies and partitions the classical FF expression into two terms. By investigating

hundreds of configurations in the pore space, the average contribution of is determined to be as small as 1 %, even for Xe adsorption, which should have the highest polarization in a material compared to Ar or Kr. This finding is important to show a basis to omit polarization term for deriving FFs for noble gas adsorption. Although our polarization description could have included more terms, they are not required since the most important term has already been included and higher terms have less magnitude. Since polarization calculations require use of accurate charges, in this case DDEC charges, omitting polarization term can save some computational time. Our FF development procedure includes both random and GCMC generated configurations meaning two different pore sampling approaches are combined. While random configurations span both negative and positive interaction energies, GCMC configurations are the equilibrated configurations which, by definition, have negative interaction energies. One important point to note about these approaches is that there are cases where GCMC configurations could describe the strongest binding configurations while randomly generated configurations have weaker bindings. Thus, it is significant to include GCMC configurations in a FF development procedure to describe adsorption phenomena more accurately. Three DFT functionals (PBE-D2, vdW-DF, and vdW-DF2) have been used to derive FFs which are selected based on the success they have shown in predicting some of the adsorption properties in porous materials[75, 135, 136], their relatively low computational cost, and their availability in VASP. The adsorption isotherms and heats of adsorption curves generated by the derived FFs have been compared with a generic FF, UFF, as well as experimental data to identify advantages and disadvantages of the developed FFs. It has been seen that in many cases PBE-D2 based FFs have good predictions compared to experimental data, especially at low pressures.

However, as pressure increases, vdW-DF2 based FFs start showing better performance, which can be clearly seen in the high pressure region of Ar adsorption in both Cu-BTC and ZIF-8. On the other hand, vdW-DF based FFs have the worst noble gas adsorption predictions for all six materials. These findings clearly show that although there are adsorbate-adsorbent cases where one DFT based FF can have good predictions, that functional cannot perform well for all adsorbate-adsorbent interactions. To understand overall FF performances, the absolute deviations from experimental data are obtained at 1 bar for each FF and they are normalized by experimental loadings, assuming that the latter values are the correct values. By looking at those values, it has been seen that PBE-D2 and vdW-DF2 based FF have similar predictions compared to UFF. Overall, the best performing FFs, PBE-D2 based FF and UFF have 30-40% deviation from experiments.

It is important to identify the details of adsorption by obtaining density plots and RDFs of adsorbates. In general, it is possible that a FF may predict the right gas uptake but it may be just a coincidence where adsorption sites and their strengths are wrong/lacking but in total they give the right number. In our M-MOF-74 density plots, for all FFs used, the corner sites in the 1-D pore channels are identified as the most strong adsorption sites. A similar observation has been made by Rana et al.[148] for methane adsorption in Mg-MOF-74. For Cu-BTC, it has been observed that the smallest pore, tetrahedral cage, is filled first. Although UFF does not predict adsorption in the main pores of Cu-BTC, the ab-initio based FFs predict some adsorption in them. Similar density plots are obtained by Hulvey et al.[151] for Ar adsorption showing strong preferential adsorption near tetrahedral cage and windows. In ZIF-8, both the windows and the cages adsorb noble gases and there is not a strong preference of one over another. Since five of the six materials studied have open

metal sites, it is crucial to see if there is preferential adsorption of noble gases near those open metal sites as noted earlier for methane storage in Cu-BTC.[152] Interestingly, in both M-MOF-74 and Cu-BTC, the noble gases are not found to preferentially bind to open metal sites. Especially, for Cu-BTC, the probability of finding non-metal sites near noble gases is much larger than that of metal sites at close distances. For ZIF-8, which does not have any open metal site, noble gases are adsorbed at sites closer to non-metal atoms.

To sum up the findings of the FF derivation work, although on a case by case basis the ab-initio derived FFs can beat UFF, on average, UFF has the lowest deviations from the experiments. Although PBE-D2 based FFs also have similar average deviations, UFF has the advantage of not requiring any quantum mechanical calculations. Still, it is important to make these observations because this tells us that for the screening of MOFs, calculations at the DFT level using PBE-D2, vdW-DF and vdW-DF2 functionals are not necessarily appropriate. It also demonstrates that UFF is not a necessarily good candidate for accurate predictions either. This necessitates deriving FFs using higher level quantum chemical calculations to have higher accuracy in predictions that can beat generic FF performance. However, as expected, higher accuracy comes with higher computational cost and if the derived FFs are not transferable, the higher computational cost has to be spent for many different adsorbate-adsorbent pairs. Doing so is not useful obviously for screening purposes.

There are two ways to get more accurate FFs. One way is to use cluster-based approaches where typically MP2 level calculations are used. Although MP2 energies would describe the interactions better than DFT functionals, cluster-based approaches may suffer from the size of the cluster models used. If the cluster size is not large enough, the

long-range interactions may not be captured properly in the calculations, limiting the accuracy of FF predictions.[129] Sufficient tests must be made to ensure the cluster size is good enough for FF development purposes. The other way to go beyond DFT accuracy is to use the DFT/CC[260, 261] approach. Basically, the DFT/CC calculations require calculations at CCSD(T), MP2 and HF levels of theory. Using those cluster calculations, a correction energy term can be generated and added to PBE energy calculated in periodic model. Having obtained corrected energy, the quantum chemical energy can be fitted to classical FF expressions similar to the way shown in this study. Since, PBE-D2 energies are obtained by adding constant dispersion correction energies to PBE energies, PBE energies can be calculated by a simple algebra rather than requiring separate calculations. Thus, to have the DFT/CC energies, the calculations needed are the ones for the clusters. A good example of this has been shown by Fang et al.[262] for CO_2 adsorption LTA-4A where PBE-D2 based FF overpredict the experiments quite significantly and DFT/CC based FF has close predictions to experiments.

Going beyond DFT calculations is not only good to improve the accuracy of predictions for a particular adsorbate-adsorbent case, but it can also bring a huge advantage that is the transferability of FFs. If the accuracy of FFs is high enough, the same FF parameters can be used in different materials as long as they have the same atom types. This implies a huge cut in computational cost since there will not be any need to derive FFs for each and every case. However, it should be noted that having good predictions for a specific adsorption case does not mean those FF parameters will always have satisfactory predictions for other cases as well. For example, one may derive the FFs for ZIF-8 by assuming there is only one carbon type in the linkers while it is also possible to assign atom

types using the connectivity of the atoms. If the latter is used, there will be two types of carbons. Similarly, with the connectivity approach, there will be two types of hydrogens rather than one. It is not easy to comment on whether assigning atom types elementwise will be sufficient to have good FF predictions, however, if such a FF cannot predict the experimental case well (assuming experimental data are reliable), the connectivity based atom type assignment may be needed as an improvement to the FF description. An example of a transferable FF has been shown by Dzubak et al.[16] for CO_2 adsorption where their FF is based on MP2 calculations. In their study, multiple types of oxygen and carbon atoms are defined to derive the FF for CO_2 adsorption Mg-MOF-74. Having validated its success compared to experimental data, they have used the same FF parameters for the linker part of MOF-5 and derived Zn parameters using the same approach. They have seen almost an excellent agreement with the experimental data.

One of the significant assumptions of the calculations in this study is that structures are taken as rigid despite the atomic fluctuations that occur in reality. Although the structure does not have to deviate from its optimized, initial structure as the adsorption takes place, there are cases especially for MIL-53 where it may "breath" due to guest molecule adsorption.[263] Framework flexibility becomes a bigger concern when the diffusion is investigated in molecular dynamics simulations.[264] In such cases, the intramolecular interactions should also be modeled which may not be trivial due to many terms affecting the structure such as bond stretch, bending, torsion etc.

Assuming that the FF accuracy is high enough, a larger set of materials can be screened. For this purpose, CoRE MOF database is ideal since the structure in it are, by definition, computationally ready to use. For the noble gas separation, the pore sizes,

especially PLD, are crucial, thus, PLD and LCD values of the structures in CoRE MOF[29] database are calculated which are shown in Figure 33.

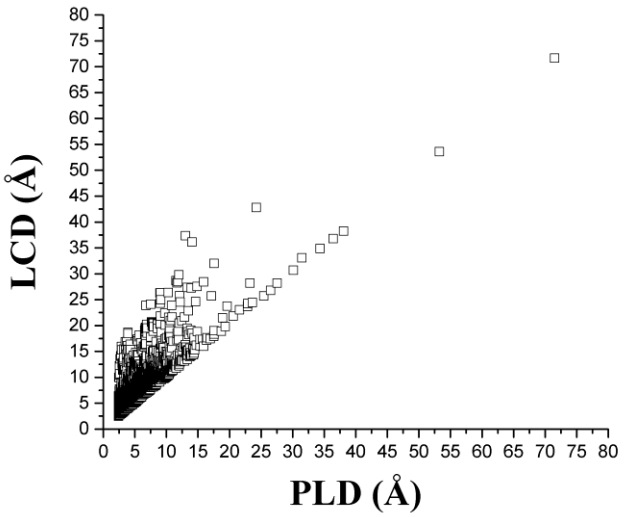

Figure 33. LCD and PLD values of the 4763 structures in CoRE MOF database.

By narrowing the list into the materials with PLDs that are of are interest, the potential candidates for noble gas separation in the database can be extracted. To have an efficient separation, a material should have pore sizes close to the desired adsorbate size and it should also ideally block the other gases in the mixture. Figure 34 show a smaller PLD scale where materials in the yellow shaded areas have potential to separate Ar/Kr, Ar/Xe, and Kr/Xe based on PLD sizes. For instance, the bottom plot in Figure 34 shows the materials that can adsorb Kr (LJ size = 3.7 Å) and block Xe (LJ size = 4.1 Å). Here, the range is specified 0.1 Å lower than the LJ sizes to consider some flexibility effect in the materials. Using such an initial screening, 372, 943, and 571 structures are identified for Ar/Kr, Ar/Xe, and Kr/Xe separations, respectively. With a transferable and accurate FF,

single-component adsorption isotherms can be obtained after which more detailed investigation can be made for top performers.

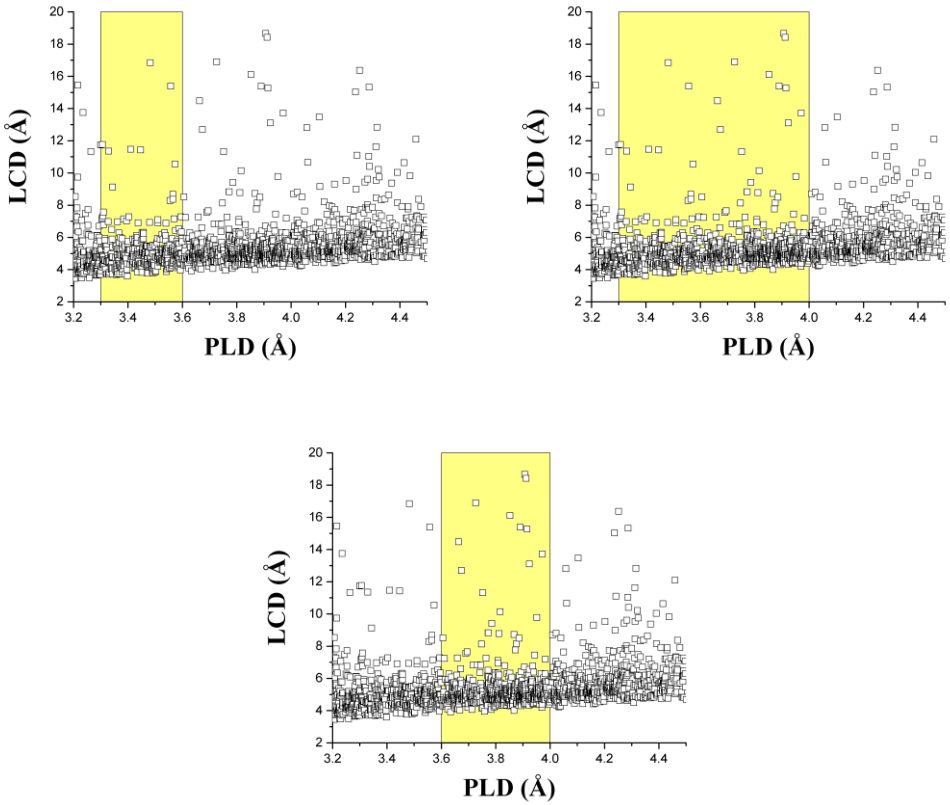

Figure 34. Candidate CoRE MOF materials for Ar/Kr (top left), Ar/Xe (top right), and Kr/Xe (bottom) separation.

In Chapter 4, functionalized UiO-66 series were investigated for the separation of contaminants (NH_3, H_2S, CO_2) from air. This separation is important since these contaminants, especially NH_3, H_2S, can be very harmful to human health even at very low concentrations. Besides determining the materials having favorable interactions with these gases in dry conditions, preferential interaction of the materials with the contaminants in humid conditions is also studied since in a real scenario air will likely be humid. Since

humidity is a concern in our study, the adsorbent should be stable under humidity, which is satisfied by parent UiO-66. Previously, Kim et al.[157] has screened affinities of functional groups attached to the UiO-66 backbone cluster towards both ammonia and water. They have identified functional groups that can have favorable interactions with ammonia in dry and humid conditions. Their study, however, lacks long range interactions due to cluster modeling. In our study, we have modeled the interactions of functional groups both in cluster and periodic models which enables us to see effect of dispersion in the ranking of materials. To understand the correlation between different levels of quantum chemical calculations, energies obtained at DFT level (PBE-D2, M06-2X) and MP2 level are compared. Good correlations are observed between both MP2 and PBE-D2, and MP2 and M06-2X, the former being better. Thus, PBE-D2 is selected to be used in periodic model. Having a good correlation between MP2 and DFT functional is quite important since it implies the screening of materials can be done reliably at a reasonable computational cost at DFT level. Having validated the qualitative agreement between MP2 and PBE-D2 energies, the interaction energies obtained at the PBE-D2 level in cluster and fully periodic models are also compared to see the effect of confinement. It has been determined that there is poor correlation between those energies, showing the importance of confinement. To estimate the dispersion effects, adsorbates are placed at the octahedral cage center and single point energies are obtained in several orientations. By extracting the dispersion part of the PBE-D2 energy, it has been seen that the dispersion can contribute up to 50% of the total adsorption energy for NH_3, H_2S and CO_2. The dispersion energy is found to change considerably for different functionalized materials. For example, it changes by 20 kJ/mol for H_2S depending on the functional group. Since the estimated dispersion effects vary

among the materials, ranking the materials based on cluster modeling will not be reliable and periodic models should be used. In periodic models, the materials are ranked based on the difference between the most favorable binding energies of a contaminant gas and water. It has been found that the rankings obtained using periodic model are different than those of cluster models implying the significance of long range interactions. It has also been seen that high affinity for a contaminant gas does not always imply favorable separation of it under humid conditions. The best performing materials for selective separation of NH_3, H_2S, and CO_2 over H_2O are [-$(Cl)_2$, -F_2, -SO_3H, -I, -Br, -F, -$(CF_3)_2$, -$(Br)_2$, -Cl, -CH_3, -$(NO_2)_2$, -NO_2, -I_2, -OCH_3, -COOH, -$(OH)_2$, -C=O, -$(COOH)_2$, -$(CH_3)_2$ and -NCO], [-NO_3, -OCH_3, -F_2, -CH_3, -I, -$(Cl)_2$ and -NCO] and [-F_2, -$(Cl)_2$, -CH_3 and -NCO] functionalized UiO-66 materials, respectively. Although there are many functional groups that can cause stronger NH_3 binding over H_2O, there are only a few functional groups that can lead to stronger H_2S and CO_2 binding over H_2O.

In spite of the fact that there is limited experimental data in the literature about functionalized UiO-66 materials, several conclusions can still be made. To have a qualitative comparison between experimental data and simulated values, the lowest binding energies of adsorbates in several functionalized materials are compared with the experimental heats of adsorption data. These two quantities are not exactly the same, thus, it does not allow a quantitative comparison but still it is useful for qualitative comparison purposes. It has been seen that the experimental ranking of water affinity for UiO-66 and UiO-66-NH_2 and the experimental ranking of CO_2 affinity in UiO-66-NH_2 and UiO-66-NO_2 are consistent with the theoretical rankings obtained in this study. Moreover, the experimental and simulated values have good agreement with each other.

To estimate the possible diffusional limitations, PLD values were calculated for each material. It has been observed that for 10 materials PLDs are smaller than 3 Å which may cause diffusion hindrance for large gas molecules such as H_2S. Although diffusion is not of primary interest of this study, for top performers diffusional limitations should be further looked into to see if there are any inaccessible regions in the pore space. Another important factor that is not studied here is coadsorption effects. Since the adsorbates are placed separately in the structures, synergistic effects are not included which may increase or decrease affinity of a gas in the presence of another gas. However, our approach is still useful to create a shortlist of materials from tens of possible functional groups and guide the experimental efforts.

The last portion of this thesis focuses on the physical properties of several non-porous layered materials. In Chapter 5, phase stabilities of $CuInP_2S_6$ and $CuInP_2Se_6$ are discussed using different approaches. The former is investigated from a thermodynamic perspective where enthalpy and free energy of mixing are calculated for In rich $CuInP_2S_6$. Assuming pure phases of $CuInP_2S_6$ and $In_{4/3}P_2S_6$, over a wide range of Cu concentration, a favorable chemical phase separation has been determined. The electrostatic energy contribution to the positive enthalpy of mixing has been determined to be significant for the phase separation using both Bader and DDEC charges. This phase separation can be seen as spinodal decomposition below the calculated spinodal decomposition temperatures. Since these temperatures are very high (10^4 K), practically it is possible to see the phase separation at the material growth conditions, which has been verified by experimental observations of Susner et al.[226] A similar analysis has been previously done for $CuIn_{1-x}Ga_xSe_2$.[251]

The phase instability of centrosymmetric $CuInP_2Se_6$ structure has been investigated by calculating vibrational motions at the zone center and zone boundaries (M, L, A k-vectors). At these k-vectors, imaginary frequencies have been obtained and the corresponding eigenvectors have been followed to generate the potential energy surface. It has been seen that the largest energy lowering occurs at the zone center and thus more calculations have been done at the Γ point. At the lowest frequency of the Γ point, the distortions lead to ferroelectric order in the structure. The corresponding polarization is calculated with respect to the magnitude of the distortion. To see if the energy stabilization can be approximated by only metal or non-metal distortions, eigenvectors are modified in a way that structures have only metal or non-metal distortions. By using those distortions, new potential energy curves are obtained which showed no energy stabilization. This implies that to see the energy stabilization a collective motion of all atoms are required and pure metal or non-metal distortions are not sufficient. Although it is possible to have more stable structure than the centrosymmetric structure by following the eigenvector at the lowest frequency of the Γ point, the former is not dynamically stable. To have the dynamically stable structure, firstly Cu atoms are off-centered by following the eigenvector distortions for Cu and then all of the atoms are relaxed. Finally, the possibility of disorder in the structure is also taken into account by introducing random disorders of metal sites in the whole bulk system or within each layer. Then, Cu atoms are off-centered along z axis and all atoms are relaxed. The vibrational DOS of the ordered structure agrees well with the experimental data and the disordered systems have decent agreement with the experimental data. It should be noted that none of them show any instability. This suggests even if there is a disorder in an experimental sample, dynamic stability is achievable.

There are several possible future directions that can be followed for $CuInP_2Se_6$-like structures. As it has been outlined earlier, detailed calculations have been performed for distortions at the Γ point. The displacements at the high symmetry k-vectors (M, L, A) can be further characterized similar to the Γ point motions. For ferroelectrics, one of the aims is to increase the polarization of the system. One way of doing this is maximizing the displacement of M^{3+} sites and minimizing M^{1+} displacement. This obviously requires replacing Cu^{1+} and In^{3+} sites with other candidate ions with the same valency, i.e. replacing In^{3+} with Sb^{3+}. Another way of achieving this can be maximizing M^{1+} displacement by using a M^{3+} which would fit very well into the octahedral cage of Se atoms and not move much. Lastly, from a practical use perspective of these materials, the switching properties of promising $CuInP_2Se_6$-like structures should be studied.

APPENDIX A

SUPPLEMENTARY INFORMATION FOR CHAPTER 3

Table 7. Derived force field parameters for Co-MOF-74.

Co-MOF-74	PBE-D2		vdW-DF		vdW-DF2	
	ε(K)	σ(Å)	ε(K)	σ(Å)	ε(K)	σ(Å)
H-Ar	3.328	3.297	379.310	2.828	52.354	2.832
C-Ar	38.439	3.474	52.363	3.565	53.618	3.470
O-Ar	74.654	3.248	108.820	3.297	164.836	3.120
Co-Ar	154.778	3.109	204.131	3.207	50.980	3.412
H-Xe	111.070	3.045	515.951	2.902	67.529	3.127
C-Xe	50.569	3.746	113.012	3.764	85.467	3.754
O-Xe	126.058	3.435	16.351	4.190	172.063	3.436
Co-Xe	696.420	3.011	708.156	3.024	35.506	3.631

Table 8. Derived force field parameters for Ni-MOF-74.

Ni-MOF-74	PBE-D2		vdW-DF		vdW-DF2	
	ε(K)	σ(Å)	ε(K)	σ(Å)	ε(K)	σ(Å)
H-Ar	82.761	2.781	556.072	2.764	96.614	2.706
C-Ar	59.596	3.415	22.316	3.780	62.023	3.439
O-Ar	40.741	3.412	134.217	3.281	134.661	3.154
Ni-Ar	249.157	3.117	239.552	3.135	51.918	3.461
H-Xe	165.573	2.950	465.085	2.950	206.695	2.926
C-Xe	92.418	3.618	136.303	3.742	55.579	3.863
O-Xe	59.839	3.616	6.516	4.487	136.081	3.488
Ni-Xe	426.137	3.169	365.972	3.261	172.595	3.453

Table 9. Derived force field parameters for Zn-MOF-74.

Zn-MOF-74	PBE-D2		vdW-DF		vdW-DF2	
	ε(K)	σ(Å)	ε(K)	σ(Å)	ε(K)	σ(Å)
H-Ar	36.141	2.957	106.027	3.021	40.066	2.907
C-Ar	42.925	3.461	107.438	3.441	39.934	3.518
O-Ar	71.147	3.300	133.997	3.229	147.642	3.171
Zn-Ar	420.107	2.901	80.596	3.311	294.334	2.982
H-Xe	67.693	3.113	61.470	3.348	52.803	3.245
C-Xe	93.532	3.576	150.958	3.663	60.448	3.772
O-Xe	51.566	3.697	144.520	3.553	105.028	3.592
Zn-Xe	935.898	2.959	26.229	3.825	667.784	3.090

Table 10. Derived force field parameters for Mg-MOF-74.

Mg-MOF-74	PBE-D2		vdW-DF		vdW-DF2	
	ε(K)	σ(Å)	ε(K)	σ(Å)	ε(K)	σ(Å)
H-Ar	37.171	2.943	289.769	2.923	3.345	3.534
C-Ar	41.524	3.487	56.289	3.513	48.664	3.476
O-Ar	62.350	3.330	116.701	3.299	161.272	3.146
Mg-Ar	500.749	2.785	332.103	2.971	217.239	2.982
H-Xe	62.490	3.155	57.441	3.372	47.666	3.301
C-Xe	68.506	3.659	155.331	3.658	57.711	3.796
O-Xe	52.662	3.651	100.188	3.629	114.757	3.564
Mg-Xe	961.205	2.969	82.051	3.565	539.425	3.157

Table 11. Derived force field parameters for ZIF-8.

ZIF-8	PBE-D2		vdW-DF		vdW-DF2	
	ε(K)	σ(Å)	ε(K)	σ(Å)	ε(K)	σ(Å)
H-Ar	110.679	2.647	52.469	3.054	176.008	2.616
C-Ar	22.864	3.761	59.430	3.594	29.188	3.723
N-Ar	374.859	2.387	601.377	2.515	166.353	2.411
Zn-Ar	107.188	2.813	107.894	4.756	107.188	2.813
H-Xe	131.705	2.995	31.717	3.367	183.048	2.941
C-Xe	23.440	4.085	44.810	4.116	35.907	4.139
N-Xe	681.114	2.831	1617.740	2.534	1342.592	2.293
Zn-Xe	162.483	3.067	231.913	5.036	162.483	3.067

Table 12. Derived force field parameters for Cu-BTC.

Cu-BTC	PBE-D2		vdW-DF		vdW-DF2	
	ε(K)	**σ(Å)**	**ε(K)**	**σ(Å)**	**ε(K)**	**σ(Å)**
H-Ar	43.364	2.784	272.412	2.819	101.287	2.623
C-Ar	52.327	3.433	80.119	3.459	76.827	3.390
O-Ar	57.899	3.306	54.718	3.462	68.363	3.282
Cu-Ar	254.085	2.881	332.408	2.911	142.607	2.740
H-Xe	113.358	3.009	65.349	3.336	258.391	2.911
C-Xe	81.649	3.620	134.442	3.729	113.761	3.705
O-Xe	101.198	3.481	73.826	3.729	13.585	4.145
Cu-Xe	600.874	2.948	656.345	3.035	727.904	2.857

Table 13. Comparison of cell parameters of experimental and optimized structures.

	CoRE (CSD) MOF/Equivalent CoRE (CSD) MOF/Optimized structure (PBE-D2, vdW-DF, vdW-DF2)					
	a	**b**	**c**	**α**	**β**	**γ**
Co-MOF-74	6.806/15.116/14.737-14.988-15.047	15.116/15.116/14.735-14.979-15.028	15.116/6.806/6.490-6.510-6.540	62.211/81.368/81.567-81.662-81.652	81.368/81.368/81.547-81.666-81.658	98.632/117.789/117.893-117.885-117.846
Mg-MOF-74	6.759/15.194/15.220-15.343-15.345	15.194/15.194/15.211-15.337-15.340	15.194/6.759/6.872-6.988-6.979	62.159/81.473/81.338-81.253-81.270	81.473/81.473/81.336-81.258-81.269	98.527/117.841/117.860-117.708-117.723
Ni-MOF-74	6.770/15.057/14.961-15.198-15.196	15.057/15.057/14.964-15.212-15.199	15.057/6.770/6.189-6.201-6.251	62.205/81.380/82.034-82.194-82.130	81.380/81.380/82.103-82.150-82.083	98.620/117.795/118.105-118.191-118.133
Zn-MOF-74	6.628/15.099/15.196-15.350-15.318	15.099/15.099/15.217-15.370-15.343	15.099/6.628/6.956-7.012-7.047	62.103/81.586/81.259-81.286-81.205	81.586/81.586/81.209-81.170-81.135	98.414/117.897/117.684-117.613-117.581
Cu-BTC	18.627/18.627/18.738-18.914-18.929	18.627/18.627/18.738-18.914-18.929	18.627/18.627/18.738-18.914-18.929	60.000/60.000/60.009-60.003-59.996	60.000/60.000/60.009-60.003-59.996	60.000/60.000/60.009-60.003-59.996
ZIF-8	14.714/14.714/14.657-14.928-14.911	14.714/14.714/14.662-14.940-14.923	14.714/14.714/14.656-14.928-14.910	109.471/109.471/109.456-109.487-109.489	109.471/109.471/109.496-109.393-109.399	109.471/109.471/109.456-109.487-109.489

Table 14. Simulated, experimental surface areas and deviations from experimental surface areas.

SA(m^2/g)	PBE-D2	vdW-DF	vdW-DF2	Experimental	Perc. Dev. (%)	Perc. Dev. (%)	Perc. Dev. (%)
Co-MOF-74	1123	1178	1191	1292	13	9	8
Mg-MOF-74	1691	1744	1748	1530	-11	-14	-14
Ni-MOF-74	1118	1151	1161	1199	7	4	3
Zn-MOF-74	1304	1337	1343	973	-34	-37	-38
Cu-BTC	2198	2285	2292	1603	-37	-43	-43
ZIF-8	1314	1430	1422	1391	6	-3	-2

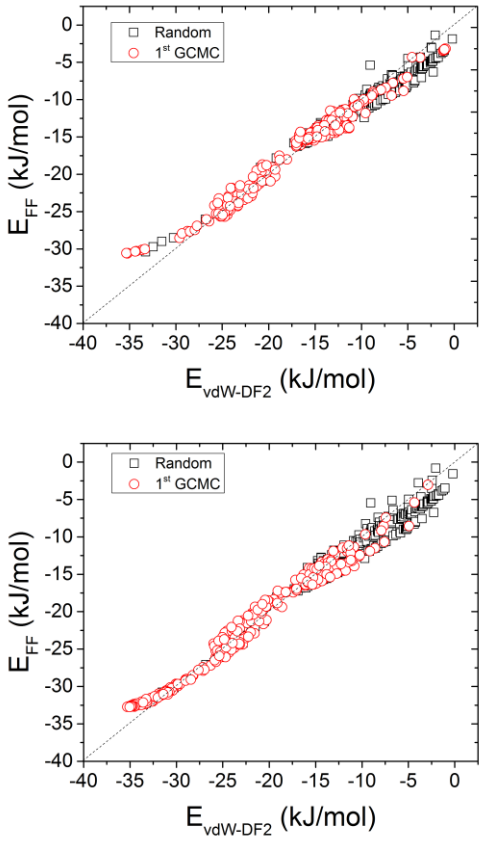

Figure 35. Comparison of vdW-DF2 and fitted FF binding energies for Xe-HKUST-1 (GCMC configurations generated at 100 (top) and 1 bar (bottom)).

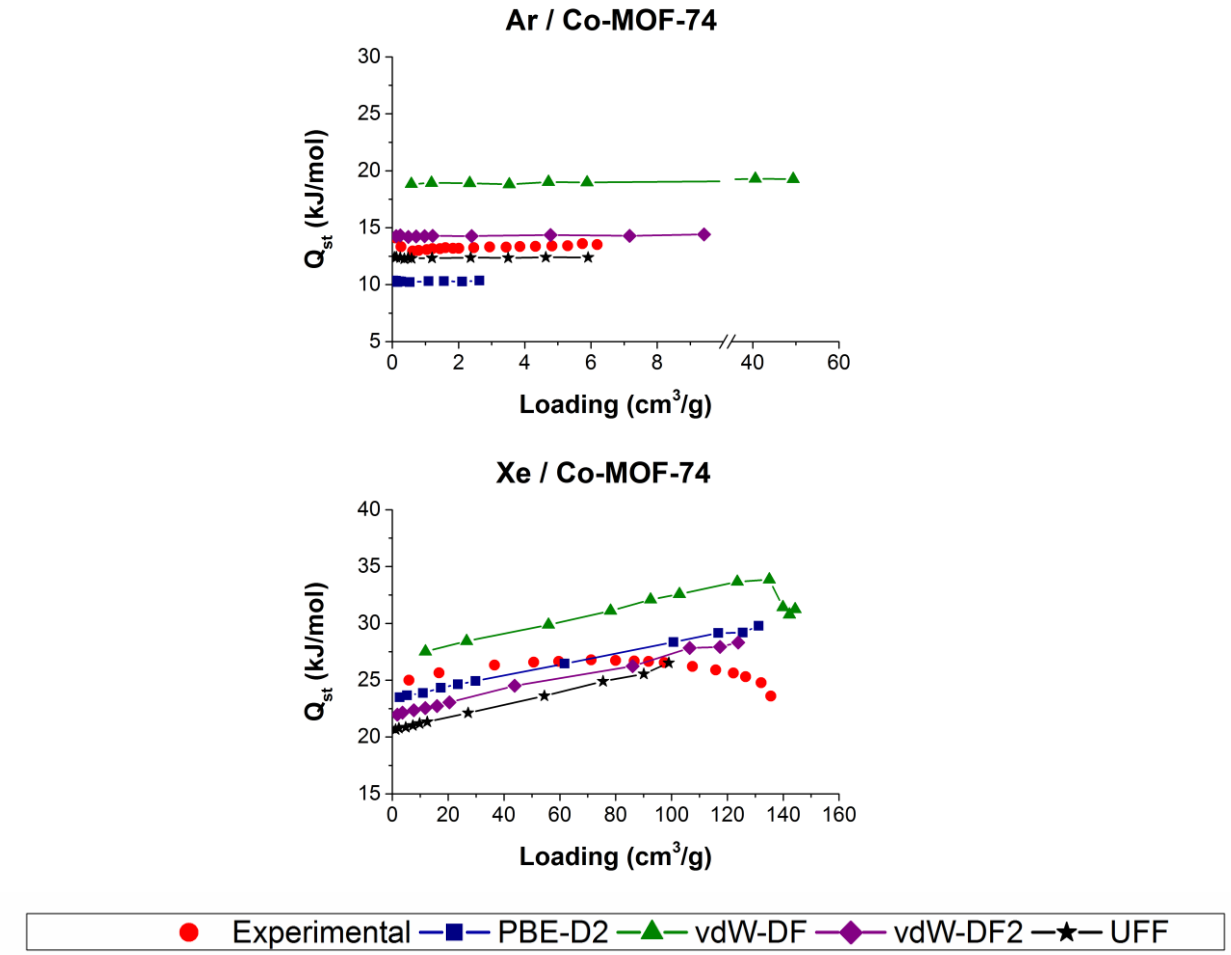

Figure 36. Heat of adsorption values calculated at 292 K for Ar and Xe adsorption in Co-MOF-74.

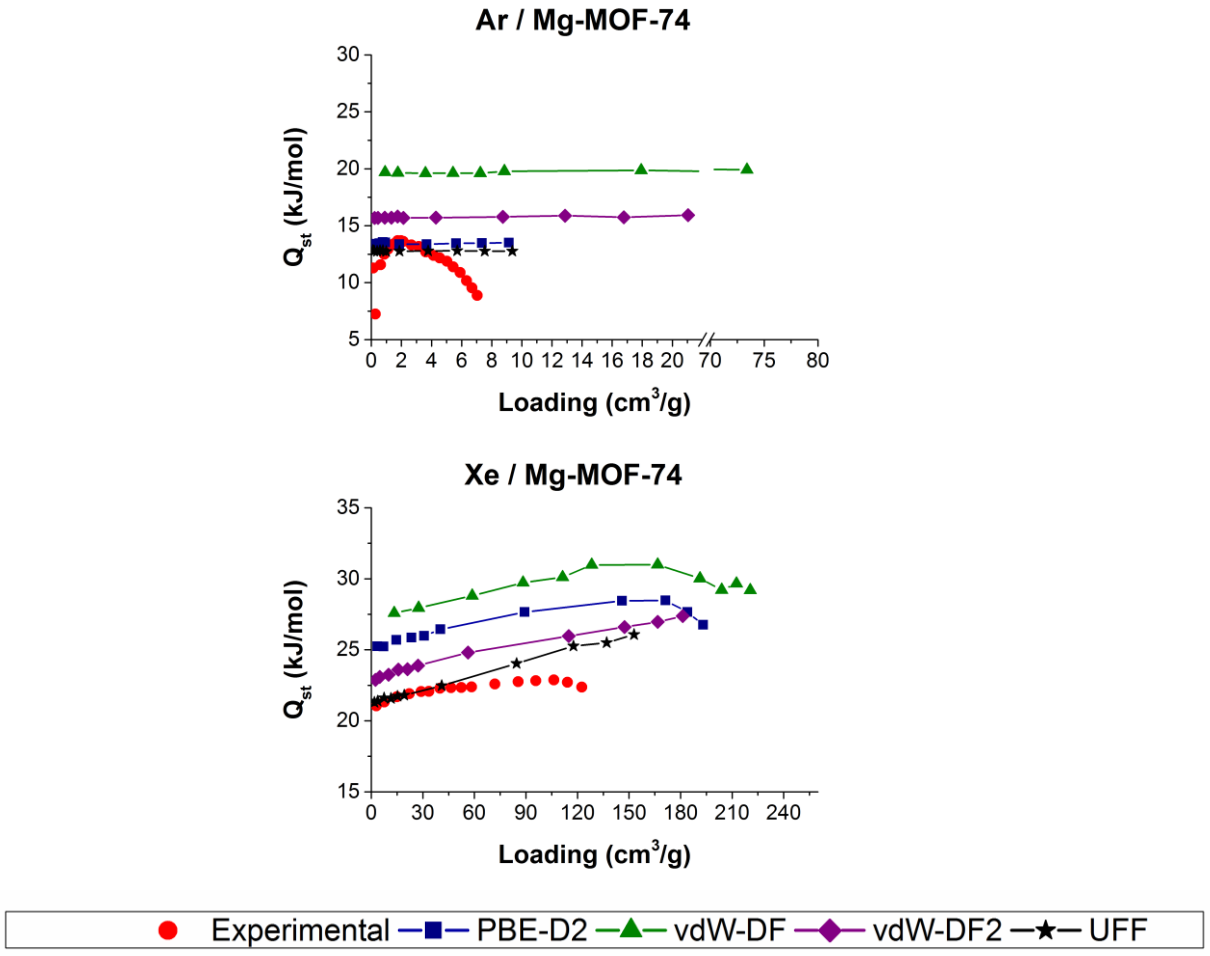

Figure 37. Heat of adsorption values calculated at 292 K for Ar and Xe adsorption in Mg-MOF-74.

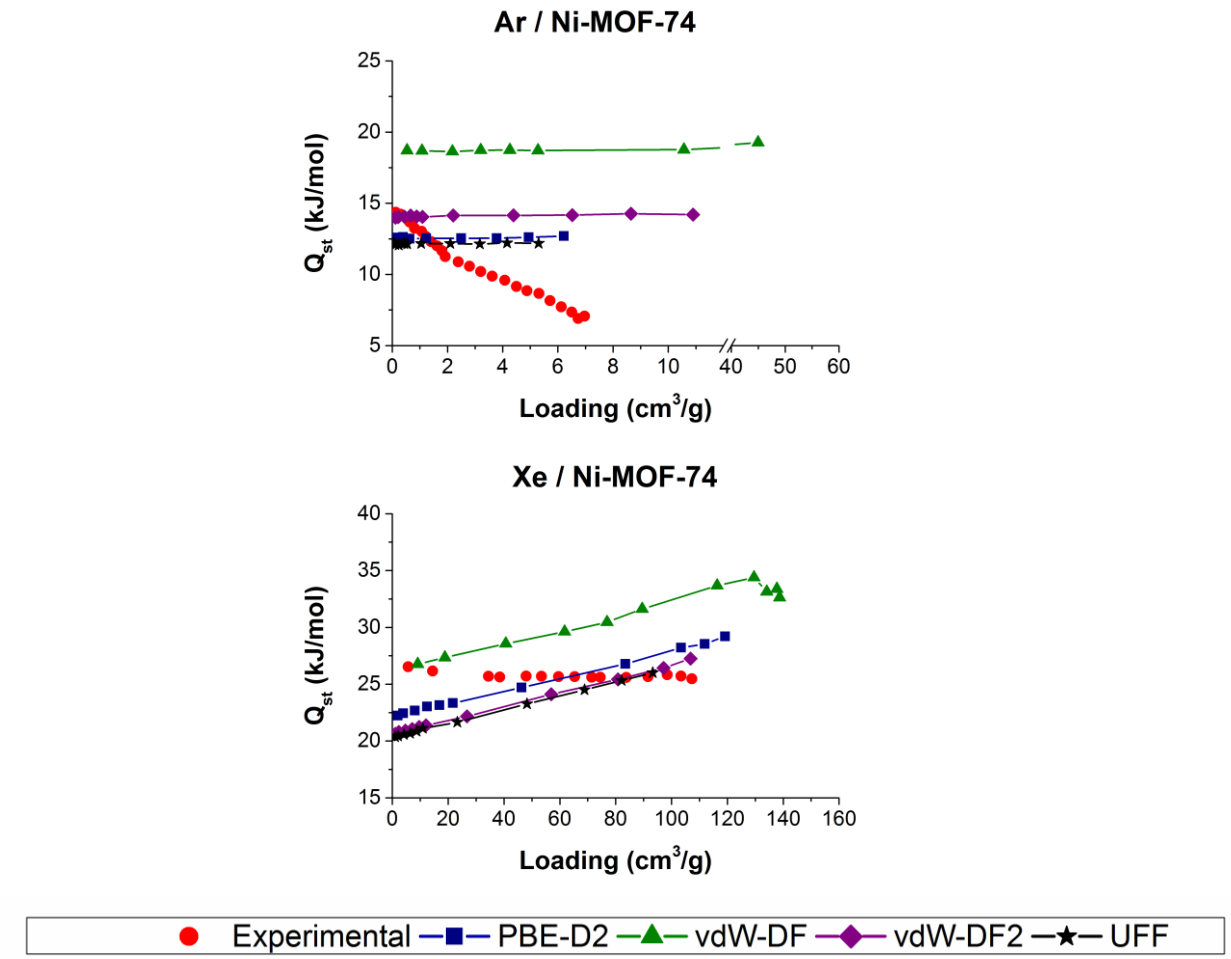

Figure 38. Heat of adsorption values calculated at 292 K for Ar and Xe adsorption in Ni-MOF-74.

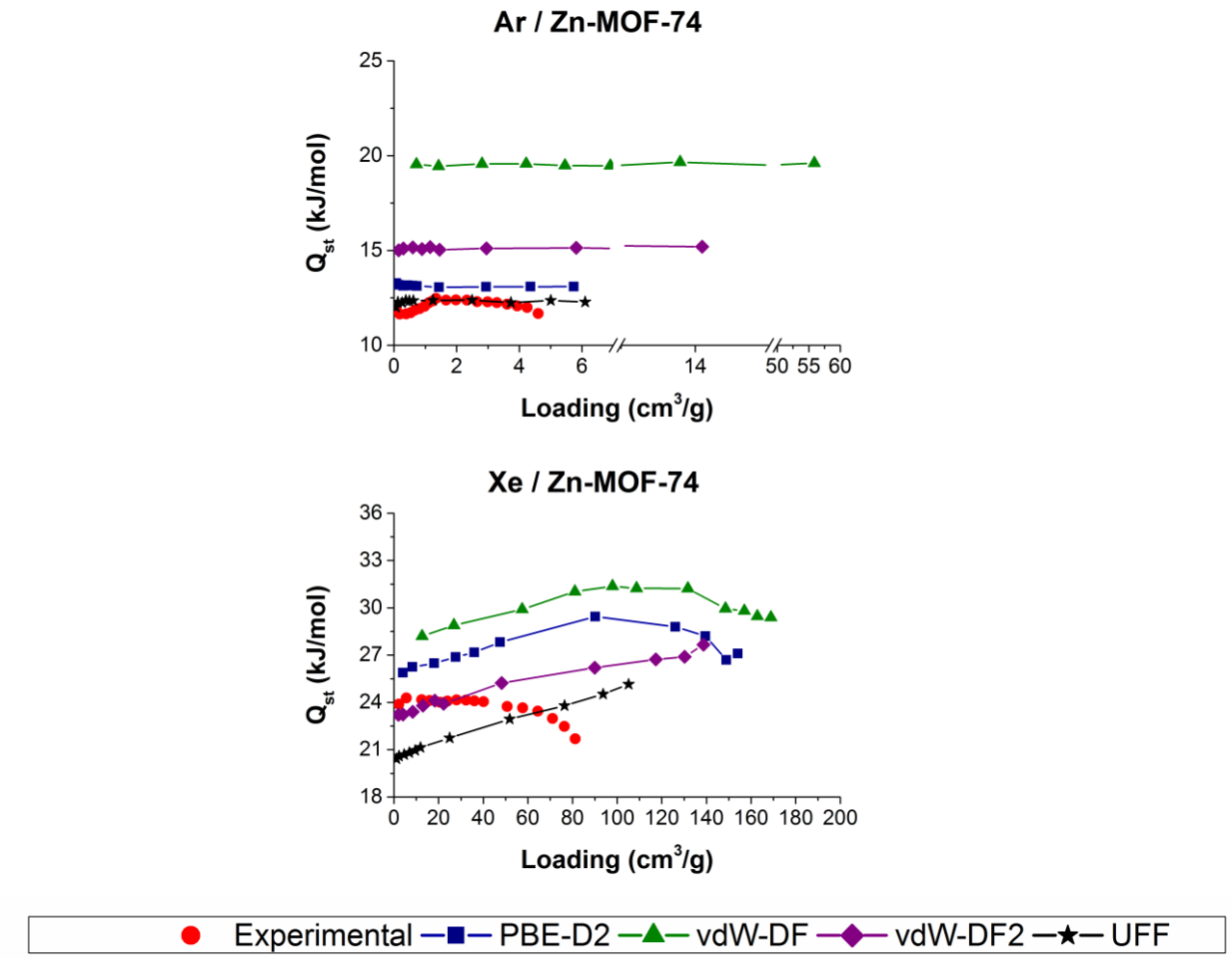

Figure 39. Heat of adsorption values calculated at 292 K for Ar and Xe adsorption in Zn-MOF-74.

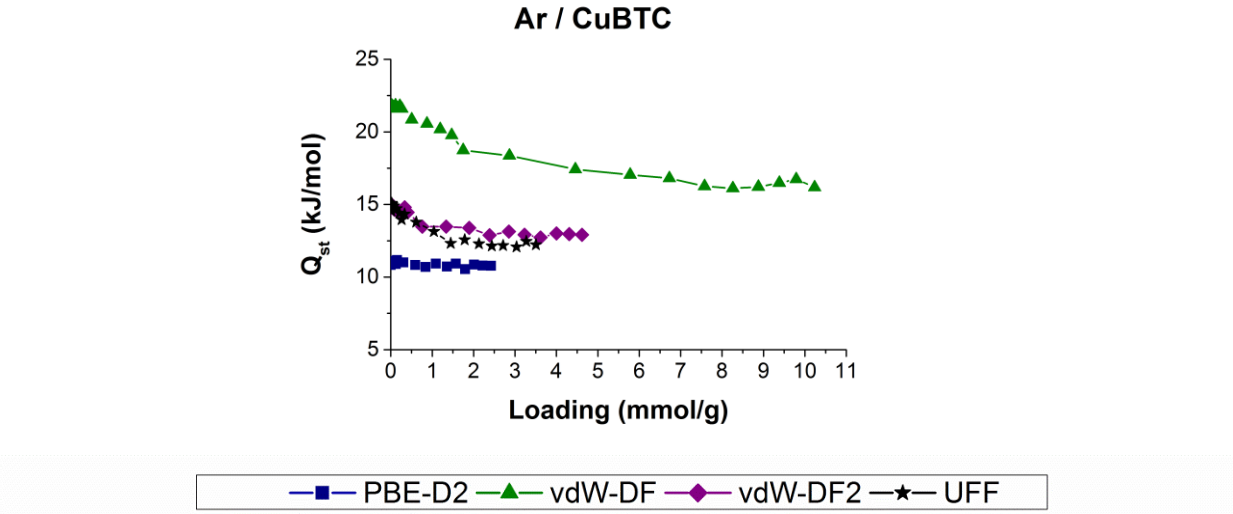

Figure 40. Heat of adsorption values for Ar-Cu-BTC at 308 K.

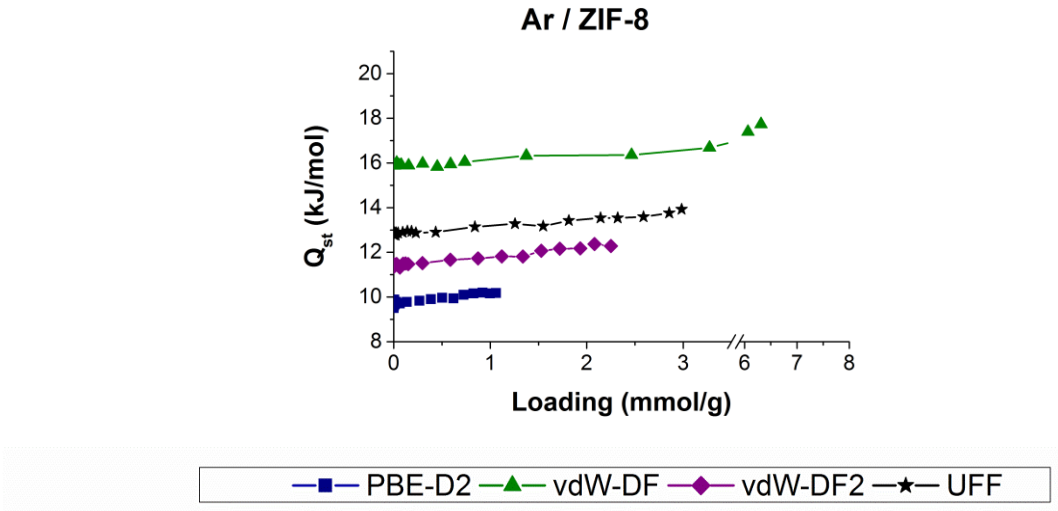

Figure 41. Heat of adsorption values for Ar-ZIF-8 at 308 K.

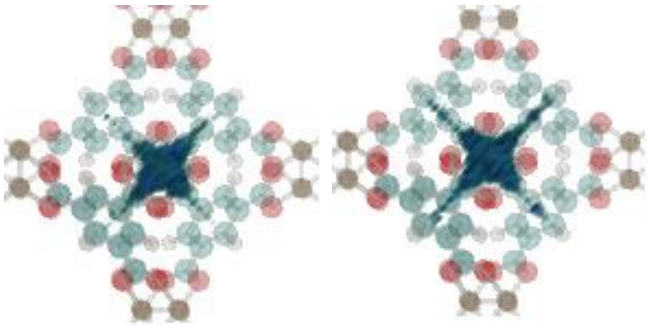

Figure 42. Density plots for Xe adsorption in Cu-BTC using PBE-D2 based FF at 308 K 0.01 bar (left) and 0.1 bar (right) (Framework drawn transparent for adsorbate clarity).

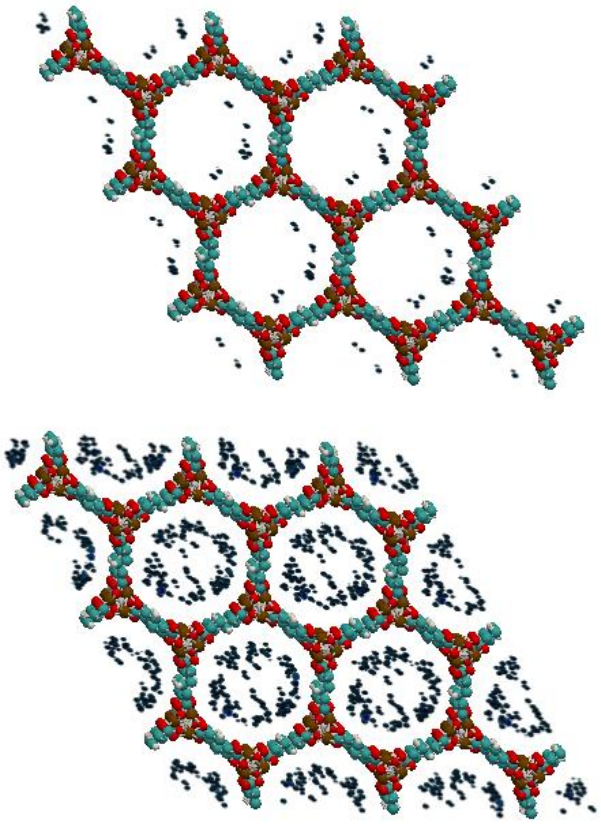

Figure 43. Density plots for Ar adsorption in Co-MOF-74 using PBE-D2 based FF at 292 K and pressures of 10^{-4} bar (left) and 10^{-3} bar (right).

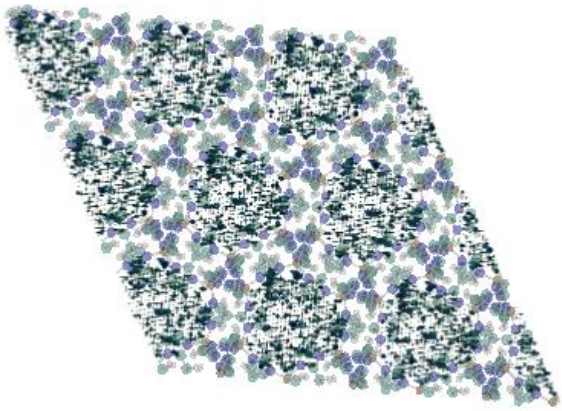

Figure 44. Density plots for Ar adsorption in ZIF-8 using PBE-D2 based FF at 308 K and 0.1 bar (Framework drawn transparent for adsorbate clarity).

APPENDIX B

SUPPLEMENTARY INFORMATION FOR CHAPTER 4

Table 15. Lowest NH_3 binding energies in clusters (kJ/mol).

	MP2	PBE-D2	M06-2X
-$(CF_3)_2$	-14.0	-22.1	-19.5
-$(CH_3)_2$	-8.1	-16.0	-7.5
-$(COOH)_2$	-41.4	-56.9	-51.0
-$(NH_2)_2$	-16.7	-26.6	-23.3
-$(OCH_3)_2$	-11.8	-19.6	-28.2
-$(OH)_2$	-32.9	-45.9	-39.3
bare UiO-66	-5.5	-11.5	-9.9
-Br	-6.7	-17.1	-14.2
-$(Br)_2$	-10.7	-18.5	-15.8
-C=O	-16.3	-25.0	-21.5
-CF_3	-12.0	-20.1	-17.1
-CH_2-F	-14.1	-24.8	-19.0
-CH_2-NH_2	-17.6	-28.3	-26.1
-CH_3	-5.2	-10.3	-8.0
-Cl	-9.0	-16.6	-14.0
-$(Cl)_2$	-10.4	-18.1	-15.5
-CN	-16.2	-24.9	-22.0
-CHO	-14.6	-23.2	-19.2
-COOAg	-78.0	-113.7	-108.6
-COOCu	-159.7	-174.3	-141.0
-COOH	-38.3	-53.0	-47.8
-COOK	-47.3	-62.6	-61.2
-COOLi	-80.8	-91.2	-85.8
-COONa	-62.3	-75.9	-72.5
-F	-10.4	-16.7	-13.5
-F_2	-11.5	-18.0	-14.8
-I	-1.8	-15.4	-13.1
-I_2	-5.4	-17.0	-16.9
-NCO	-14.9	-22.1	-20.9
-NH_2	-17.8	-28.0	-24.2
-NO_2	-14.2	-21.3	-19.1
-NO_3	-14.2	-20.5	-23.8

Table 15 (continued).

	MP2	PBE-D2	M06-2X
-OCH_3	-11.6	-19.6	-18.7
-OH	-33.3	-47.3	-40.4
-OOH	-37.3	-53.4	-47.1
-SO_3H	-51.8	-64.1	-66.5

Table 16. Lowest H_2S binding energies in clusters (kJ/mol).

	MP2	PBE-D2	M06-2X
-$(CF_3)_2$	-5.1	-12.1	-12.2
-$(CH_3)_2$	-10.1	-18.4	-18.3
-$(COOH)_2$	-16.3	-30.4	-25.1
-$(NH_2)_2$	-14.6	-24.6	-23.5
-$(OCH_3)_2$	-10.9	-16.9	-24.6
-$(OH)_2$	-12.3	-20.6	-17.6
bare UiO-66	-6.8	-13.9	-14.2
-Br	-7.3	-13.9	-15.4
-$(Br)_2$	-6.0	-12.6	-13.4
-C=O	-10.1	-18.2	-14.2
-CF_3	-5.9	-14.6	-14.4
-CH_2-F	-7.7	-19.5	-10.8
-CH_2-NH_2	-13.0	-28.7	-22.2
-CH_3	-9.2	-16.6	-17.0
-Cl	-6.8	-14.0	-10.8
-$(Cl)_2$	-5.7	-12.4	-13.5
-CN	-10.1	-17.4	-15.0
-CHO	-10.9	-20.1	-15.1
-COOAg	-43.1	-76.2	-71.0
-COOCu	-114.5	-140.5	-102.2
-COOH	-43.4	-55.8	-54.9
-COOK	-27.7	-48.5	-39.7
-COOLi	-37.7	-55.2	-45.1
-COONa	-31.7	-53.9	-44.8
-F	-6.0	-12.9	-11.9
-F_2	-5.5	-11.0	-11.0
-I	-0.6	-8.2	-9.9
-I_2	0.0	-7.1	-8.5

Table 16 (continued).

	MP2	PBE-D2	M06-2X
-NCO	-6.6	-13.0	-14.1
-NH_2	-13.0	-21.5	-21.4
-NO_2	-8.1	-15.4	-12.9
-NO_3	-7.7	-14.5	-16.2
-OCH_3	-9.9	-17.5	-18.7
-OH	-10.9	-20.8	-17.3
-OOH	-14.6	-27.3	-25.8
-SO_3H	-20.6	-33.1	-30.4

Table 17. Lowest H_2O binding energies in clusters (kJ/mol).

	MP2	PBE-D2	M06-2X
-$(CF_3)_2$	-12.8	-19.3	-15.6
-$(CH_3)_2$	-12.4	-21.9	-19.1
-$(COOH)_2$	-38.1	-54.0	-49.7
-$(NH_2)_2$	-23.3	-32.8	-28.2
-$(OCH_3)_2$	-17.6	-23.6	-31.0
-$(OH)_2$	-25.8	-33.0	-31.2
bare UiO-66	-9.1	-17.3	-14.9
-Br	-9.6	-14.1	-14.5
-$(Br)_2$	-10.1	-17.9	-15.2
-C=O	-23.0	-32.3	-29.4
-CF_3	-11.8	-19.1	-17.0
-CH_2-F	-19.7	-29.9	-9.0
-CH_2-NH_2	-11.1	-42.6	-30.5
-CH_3	-11.3	-19.9	-17.5
-Cl	-9.2	-16.9	-14.5
-$(Cl)_2$	-8.5	-17.3	-15.2
-CN	-19.2	-26.9	-25.3
-CHO	-22.0	-32.2	-28.4
-COOAg	-45.8	-67.8	-74.9
-COOCu	-96.5	-110.7	-94.2
-COOH	-64.9	-79.3	-79.1
-COOK	-61.8	-75.8	-74.4
-COOLi	-70.1	-90.0	-79.9
-COONa	-65.0	-80.1	-77.0

Table 17 (continued).

	MP2	**PBE-D2**	**M06-2X**
-F	-13.3	-18.2	-16.9
-F_2	-13.4	-18.5	-17.6
-I	-1.0	-15.7	-13.0
-I_2	-1.9	-16.1	-13.5
-NCO	-12.3	-22.1	-23.3
-NH_2	-21.6	-29.3	-25.3
-NO_2	-16.9	-24.0	-23.5
-NO_3	-16.5	-23.9	-24.6
-OCH_3	-16.7	-23.8	-21.2
-OH	-25.8	-33.4	-31.6
-OOH	-27.1	-40.1	-36.8
-SO_3H	-42.6	-55.3	-55.7

Table 18. Lowest binding energies (kJ/mol) of NH_3 in cluster and periodic models at PBE-D2 level.

	Periodic	**Cluster**
-OOH	-128.6	-53.4
-SO_3H	-118.8	-64.1
-$(OH)_2$	-117.2	-45.9
-COOH	-99.7	-53.0
-$(COOH)_2$	-99.3	-56.9
-$(Br)_2$	-89.7	-18.5
-CHO	-82.4	-23.2
-OCH_3	-80.4	-19.6
-NO_2	-78.9	-21.3
-$(OCH_3)_2$	-77.0	-19.6
-F_2	-72.7	-18.0
-$(Cl)_2$	-71.5	-18.1
-$(CF_3)_2$	-69.3	-22.1
-I	-63.2	-15.4
-Br	-63.1	-17.1
-C=O	-62.3	-25.0
-$(NH_2)_2$	-61.3	-26.6
-NCO	-59.1	-22.1
-CN	-59.0	-24.9
-Cl	-57.5	-16.6
-I_2	-55.6	-17.0
-OH	-54.0	-47.3
-NH_2	-52.3	-28.0
-CH_2-NH_2	-51.9	-28.3
-F	-50.5	-16.7
-CH_2-F	-39.9	-24.8
Bare UiO-66	-33.8	-11.5
-CH_3	-32.2	-10.3
-$(CH_3)_2$	-31.8	-16.0
-CF_3	-31.2	-20.1
-NO_3	-29.9	-20.5

Table 19. Lowest binding energies (kJ/mol) of H_2S in cluster and periodic models at PBE-D2 level.

	Periodic	**Cluster**
-NO_3	-105.6	-14.5
-OCH_3	-93.8	-17.5
-$(OH)_2$	-92.7	-20.6
-OOH	-74.4	-27.3
-CH_2-NH_2	-74.3	-28.7
-$(OCH_3)_2$	-70.3	-16.9
-SO_3H	-69.0	-33.1
-$(COOH)_2$	-64.3	-30.4
-NCO	-58.2	-13.0
-CHO	-56.9	-20.1
-COOH	-54.5	-55.8
-$(NH_2)_2$	-49.2	-24.6
-F_2	-48.8	-11.0
-NH_2	-44.9	-21.5
-NO_2	-43.6	-15.4
-OH	-42.4	-20.8
-I_2	-40.8	-7.1
-I	-39.8	-8.2
-$(Br)_2$	-38.6	-12.6
-CN	-38.3	-17.4
-C=O	-35.8	-18.2
-CH_2-F	-35.7	-19.5
Bare UiO-66	-31.0	-13.9
-$(CF_3)_2$	-29.5	-12.1
-CH_3	-27.3	-16.6
-Br	-27.2	-13.9
-Cl	-26.8	-14.0
-$(Cl)_2$	-25.8	-12.4
-CF_3	-24.4	-14.6
-F	-19.3	-12.9
-$(CH_3)_2$	-16.9	-18.4

Table 20. Lowest binding energies (kJ/mol) of H_2O in cluster and periodic models at PBE-D2 level.

	Periodic	**Cluster**
-OOH	-130.9	-40.1
-$(OH)_2$	-105.7	-33.0
-CHO	-99.4	-32.2
-$(OCH_3)_2$	-98.7	-23.6
-CH_2-NH_2	-89.0	-42.6
-$(COOH)_2$	-88.1	-54.0
-COOH	-84.2	-79.3
-SO_3H	-83.1	-55.3
-$(NH_2)_2$	-79.2	-32.8
-NH_2	-69.4	-29.3
-CN	-67.5	-26.9
-$(Br)_2$	-64.9	-17.9
-OCH_3	-64.4	-23.8
-NO_2	-61.9	-24.0
-OH	-61.0	-33.4
-NCO	-54.8	-22.1
-C=O	-50.8	-32.3
-CH_2-F	-45.1	-29.9
-$(CF_3)_2$	-42.2	-19.3
-I_2	-39.5	-16.1
-NO_3	-38.7	-23.9
Bare UiO-66	-36.5	-17.3
-Cl	-35.4	-16.9
-Br	-33.9	-14.1
-CF_3	-32.1	-19.1
-I	-28.7	-15.7
-F	-23.0	-18.2
-$(CH_3)_2$	-21.2	-21.9
-F_2	-20.3	-18.5
-$(Cl)_2$	-15.5	-17.3
-CH_3	-14.5	-19.9

Table 21. Dispersion energies (kJ/mol) at the octahedral pore centers and ratios of dispersion energy at the octahedral pore center/binding energy calculated with PBE-D2 functional in periodic models of UiO-66 variants.

	Dispersion energy (kJ/mol)			**Disp./BE**		
	NH_3	**H_2S**	**CO_2**	**NH_3**	**H_2S**	**CO_2**
bare	-3.3	-4.6	-4.5	0.10	0.15	0.30
-Br	-7.9	-11.5	-10.7	0.12	0.42	0.47
-$(Br)_2$	-10.6	-14.8	-14.9	0.12	0.38	0.48
-Cl	-5.5	-7.7	-7.5	0.09	0.29	0.34
-$(Cl)_2$	-7.1	-9.8	-9.9	0.10	0.38	0.35
-F	-3.6	-5.1	-5.0	0.07	0.26	0.21
-F_2	-4.0	-5.5	-5.5	0.05	0.11	0.11
-I	-12.3	-17.4	-16.9	0.19	0.44	0.57
-NH_2	-4.9	-7.0	-7.0	0.09	0.16	0.23
-$(NH_2)_2$	-6.1	-8.3	-8.5	0.10	0.17	0.16
-NO_2	-5.6	-7.7	-7.4	0.07	0.18	0.23
-$(NO_2)_2$	-6.0	-8.6	-8.8	0.06	0.11	0.11
-OH	-4.4	-6.3	-6.1	0.08	0.15	0.21
-$(OH)_2$	-5.4	-7.5	-7.7	0.05	0.08	0.11
-OOH	-9.3	-12.6	-12.4	0.07	0.17	0.18
-CH_2-NH_2	-20.8	-25.9	-23.1	0.40	0.35	0.52
-CH_2-F	-8.8	-11.6	-11.4	0.22	0.32	0.32
-C=O	-2.5	-3.5	-3.4	0.04	0.10	0.10
-CH_3	-5.7	-8.3	-8.2	0.18	0.30	0.35
-$(CH_3)_2$	-7.2	-10.2	-10.5	0.23	0.60	0.51
-CN	-5.9	-8.8	-8.8	0.10	0.23	0.23
-CHO	-5.5	-8.0	-7.7	0.07	0.14	0.13
-$(COOH)_2$	-11.4	-16.2	-16.3	0.12	0.25	0.48
-OCH_3	-9.4	-13.4	-13.1	0.12	0.14	0.20
-CF_3	-9.5	-12.5	-12.3	0.30	0.51	0.59
-$(CF_3)_2$	-10.4	-14.2	-14.7	0.15	0.48	0.53
-COOH	-7.1	-10.1	-9.9	0.07	0.19	0.26
-I_2	-18.6	-25.7	-23.7	0.34	0.63	0.71
-NCO	-15.7	-18.6	-18.9	0.27	0.32	0.30
-$(OCH_3)_2$	-14.3	-20.2	-20.0	0.19	0.29	0.66
-SO_3H	-13.3	-17.8	-18.5	0.11	0.26	0.38
-NO_3	-12.8	-18.1	-15.1	0.43	0.17	0.58

Table 22. Lowest binding energies and energy differences in kJ/mol compared to H_2O for all adsorbates studied in periodic models.

	NH_3	H_2S	H_2O	CO_2	NH_3-H_2O	H_2S-H_2O	CO_2-H_2O
bare	-33.8	-31.0	-36.5	-14.9	2.7	5.5	21.6
-Br	-63.1	-27.2	-33.9	-22.9	-29.3	6.6	11.0
-$(Br)_2$	-89.7	-38.6	-64.9	-30.8	-24.7	26.3	34.2
-Cl	-57.5	-26.8	-35.4	-22.0	-22.1	8.6	13.4
-$(Cl)_2$	-71.5	-25.8	-15.5	-28.3	-56.0	-10.3	-12.8
-F	-50.5	-19.3	-23.0	-24.5	-27.5	3.7	-1.5
-F_2	-72.7	-48.8	-20.3	-48.2	-52.4	-28.4	-27.9
-I	-63.2	-39.8	-28.7	-29.8	-34.5	-11.0	-1.1
-NH_2	-52.3	-44.9	-69.4	-29.9	17.1	24.5	39.4
-$(NH_2)_2$	-61.3	-49.2	-79.2	-51.9	18.0	30.1	27.3
-NO_2	-78.9	-43.6	-61.9	-33.0	-16.9	18.3	29.0
-$(NO_2)_2$	-101.5	-81.7	-84.4	-76.9	-17.0	2.8	7.5
-OH	-54.0	-42.4	-61.0	-28.6	7.0	18.6	32.4
-$(OH)_2$	-117.2	-92.7	-105.7	-70.2	-11.6	13.0	35.5
-OOH	-128.6	-74.4	-130.9	-68.5	2.2	56.4	62.4
-CH_2-NH_2	-51.9	-74.3	-89.0	-44.5	37.1	14.7	44.5
-CH_2-F	-39.9	-35.7	-45.1	-35.7	5.2	9.4	9.4
-C=O	-62.3	-35.8	-50.8	-32.9	-11.5	15.0	17.9
-CH_3	-32.2	-27.3	-14.5	-23.4	-17.7	-12.7	-8.9
-$(CH_3)_2$	-31.8	-16.9	-21.2	-20.6	-10.6	4.3	0.6
-CN	-59.0	-38.3	-67.5	-38.4	8.5	29.2	29.1
-CHO	-82.4	-56.9	-99.4	-60.7	17.0	42.5	38.7
-$(COOH)_2$	-99.3	-64.3	-88.1	-34.2	-11.2	23.8	53.9
-OCH_3	-80.4	-93.8	-64.4	-66.1	-15.9	-29.3	-1.6
-CF_3	-31.2	-24.4	-32.1	-20.8	0.9	7.7	11.2
-$(CF_3)_2$	-69.3	-29.5	-42.2	-27.7	-27.1	12.7	14.4
-COOH	-99.7	-54.5	-84.2	-37.2	-15.4	29.7	47.0
-I_2	-55.6	-40.8	-39.5	-33.3	-16.1	-1.3	6.2
-NCO	-59.1	-58.2	-54.8	-62.3	-4.3	-3.4	-7.5
-$(OCH_3)_2$	-77.0	-70.3	-98.7	-30.1	21.7	28.4	68.6
-SO_3H	-118.8	-69.0	-83.1	-48.7	-35.7	14.1	34.4
-NO_3	-29.9	-105.6	-38.7	-26.0	8.8	-66.9	12.7

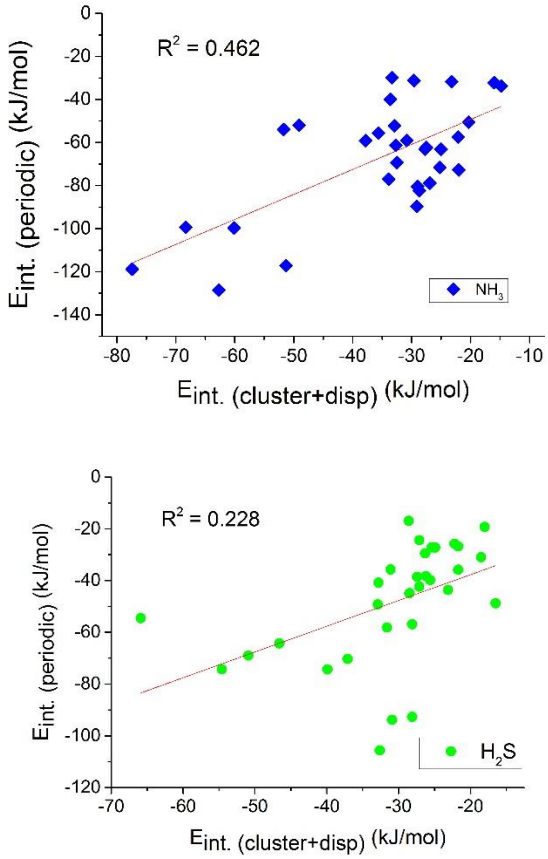

Figure 45. Interaction energies in periodic models in comparison with the summation of interactions in cluster models and dispersion energies at the octahedral pore center of the periodic models.

APPENDIX C

SUPPLEMENTARY INFORMATION FOR CHAPTER 5

Table 23. Distortions in fractional coordinates at the lowest frequency of the Γ mode (Distortion magnitude = 1).

	x	**y**	**z**		**x**	**y**	**z**
Cu1	0	9.99E-16	0.006101	Se9	-0.00041	0.00033	-0.00028
Cu2	0	9.99E-16	0.006101	Se10	-0.00041	0.00033	-0.00028
Cu3	0	9.99E-16	0.006101	Se11	-0.00041	0.00033	-0.00028
Cu4	0	9.99E-16	0.006101	Se12	-0.00041	0.00033	-0.00028
Cu5	2E-15	3E-15	0.006101	Se13	-0.00041	0.00033	-0.00028
Cu6	2E-15	3E-15	0.006101	Se14	-0.00041	0.00033	-0.00028
Cu7	2E-15	3E-15	0.006101	Se15	-0.00041	0.00033	-0.00028
Cu8	2E-15	3E-15	0.006101	Se16	-0.00041	0.00033	-0.00028
In1	1	1	-0.00132	Se17	-0.00033	-0.00074	-0.00028
In2	0	1	-0.00132	Se18	-0.00033	-0.00074	-0.00028
In3	1	-1E-15	-0.00132	Se19	-0.00033	-0.00074	-0.00028
In4	0	-1E-15	-0.00132	Se20	-0.00033	-0.00074	-0.00028
In5	1	1E-16	-0.00132	Se21	-0.00033	-0.00074	-0.00028
In6	0	1E-16	-0.00132	Se22	-0.00033	-0.00074	-0.00028
In7	1	0	-0.00132	Se23	-0.00033	-0.00074	-0.00028
In8	0	0	-0.00132	Se24	-0.00033	-0.00074	-0.00028

Table 23 (continued).

	x	y	z		x	y	z
P1	0	-1E-15	-0.00069	Se25	0.000412	0.000742	-0.00028
P2	0	-1E-15	-0.00069	Se26	0.000412	0.000742	-0.00028
P3	0	-1E-15	-0.00069	Se27	0.000412	0.000742	-0.00028
P4	0	-1E-15	-0.00069	Se28	0.000412	0.000742	-0.00028
P5	2E-15	9.99E-16	-0.00069	Se29	0.000412	0.000742	-0.00028
P6	9.99E-16	9.99E-16	-0.00069	Se30	0.000412	0.000742	-0.00028
P7	2E-15	9.99E-16	-0.00069	Se31	0.000412	0.000742	-0.00028
P8	9.99E-16	9.99E-16	-0.00069	Se32	0.000412	0.000742	-0.00028
P9	9.99E-16	9.99E-16	-0.00069	Se33	0.00033	-0.00041	-0.00028
P10	9.99E-16	9.99E-16	-0.00069	Se34	0.00033	-0.00041	-0.00028
P11	9.99E-16	9.99E-16	-0.00069	Se35	0.00033	-0.00041	-0.00028
P12	9.99E-16	9.99E-16	-0.00069	Se36	0.00033	-0.00041	-0.00028
P13	-2E-15	0	-0.00069	Se37	0.00033	-0.00041	-0.00028
P14	-2E-15	0	-0.00069	Se38	0.00033	-0.00041	-0.00028
P15	-2E-15	0	-0.00069	Se39	0.00033	-0.00041	-0.00028
P16	-2E-15	0	-0.00069	Se40	0.00033	-0.00041	-0.00028
Se1	0.000742	0.000412	-0.00028	Se41	-0.00074	-0.00033	-0.00028
Se2	0.000742	0.000412	-0.00028	Se42	-0.00074	-0.00033	-0.00028
Se3	0.000742	0.000412	-0.00028	Se43	-0.00074	-0.00033	-0.00028
Se4	0.000742	0.000412	-0.00028	Se44	-0.00074	-0.00033	-0.00028

Table 23 (continued).

	x	**y**	**z**		**x**	**y**	**z**
Se5	0.000742	0.000412	-0.00028	Se45	-0.00074	-0.00033	-0.00028
Se6	0.000742	0.000412	-0.00028	Se46	-0.00074	-0.00033	-0.00028
Se7	0.000742	0.000412	-0.00028	Se47	-0.00074	-0.00033	-0.00028
Se8	0.000742	0.000412	-0.00028	Se48	-0.00074	-0.00033	-0.00028

Table 24. Distortions in fractional coordinates at the second lowest frequency of the Γ mode (Distortion magnitude = 1).

	x	y	z		x	y	z
Cu1	0	0	-0.00625	Se9	0.000427	-0.00033	-0.00011
Cu2	0	0	-0.00625	Se10	0.000427	-0.00033	-0.00011
Cu3	0	0	-0.00625	Se11	0.000427	-0.00033	-0.00011
Cu4	0	0	-0.00625	Se12	0.000427	-0.00033	-0.00011
Cu5	2E-15	3E-15	0.006248	Se13	-0.00043	0.000331	0.000107
Cu6	2E-15	3E-15	0.006248	Se14	-0.00043	0.000331	0.000107
Cu7	2E-15	3E-15	0.006248	Se15	-0.00043	0.000331	0.000107
Cu8	2E-15	3E-15	0.006248	Se16	-0.00043	0.000331	0.000107
In1	6E-16	1	0.001074	Se17	0.000331	0.000757	-0.00011
In2	9.99E-16	1	0.001074	Se18	0.000331	0.000757	-0.00011
In3	6E-16	-1E-15	0.001074	Se19	0.000331	0.000757	-0.00011
In4	9.99E-16	-1E-15	0.001074	Se20	0.000331	0.000757	-0.00011
In5	1	2E-16	-0.00107	Se21	-0.00033	-0.00076	0.000107
In6	0	2E-16	-0.00107	Se22	-0.00033	-0.00076	0.000107
In7	1	0	-0.00107	Se23	-0.00033	-0.00076	0.000107
In8	0	0	-0.00107	Se24	-0.00033	-0.00076	0.000107
P1	0	9.99E-16	0.000242	Se25	-0.00043	-0.00076	-0.00011
P2	0	9.99E-16	0.000242	Se26	-0.00043	-0.00076	-0.00011
P3	0	9.99E-16	0.000242	Se27	-0.00043	-0.00076	-0.00011

Table 24 (continued).

	x	y	z		x	y	z
P4	0	9.99E-16	0.000242	Se28	-0.00043	-0.00076	-0.00011
P5	9.99E-16	9.99E-16	-0.00024	Se29	0.000427	0.000757	0.000107
P6	9.99E-16	9.99E-16	-0.00024	Se30	0.000427	0.000757	0.000107
P7	9.99E-16	9.99E-16	-0.00024	Se31	0.000427	0.000757	0.000107
P8	0	9.99E-16	-0.00024	Se32	0.000427	0.000757	0.000107
P9	-1E-15	-2E-15	0.000242	Se33	-0.00033	0.000427	-0.00011
P10	-1E-15	-2E-15	0.000242	Se34	-0.00033	0.000427	-0.00011
P11	-1E-15	-2E-15	0.000242	Se35	-0.00033	0.000427	-0.00011
P12	-1E-15	-2E-15	0.000242	Se36	-0.00033	0.000427	-0.00011
P13	-2E-15	0	-0.00024	Se37	0.000331	-0.00043	0.000107
P14	-2E-15	0	-0.00024	Se38	0.000331	-0.00043	0.000107
P15	-2E-15	0	-0.00024	Se39	0.000331	-0.00043	0.000107
P16	-2E-15	0	-0.00024	Se40	0.000331	-0.00043	0.000107
Se1	-0.00076	-0.00043	-0.00011	Se41	0.000757	0.000331	-0.00011
Se2	-0.00076	-0.00043	-0.00011	Se42	0.000757	0.000331	-0.00011
Se3	-0.00076	-0.00043	-0.00011	Se43	0.000757	0.000331	-0.00011
Se4	-0.00076	-0.00043	-0.00011	Se44	0.000757	0.000331	-0.00011
Se5	0.000757	0.000427	0.000107	Se45	-0.00076	-0.00033	0.000107
Se6	0.000757	0.000427	0.000107	Se46	-0.00076	-0.00033	0.000107
Se7	0.000757	0.000427	0.000107	Se47	-0.00076	-0.00033	0.000107
Se8	0.000757	0.000427	0.000107	Se48	-0.00076	-0.00033	0.000107

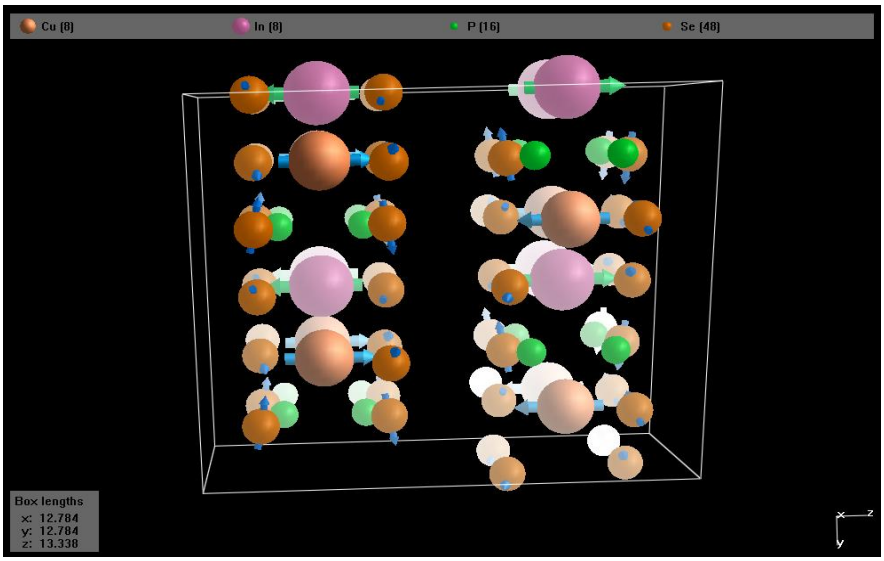

Figure 46. The eigenvectors at the second lowest frequency of the Γ point.

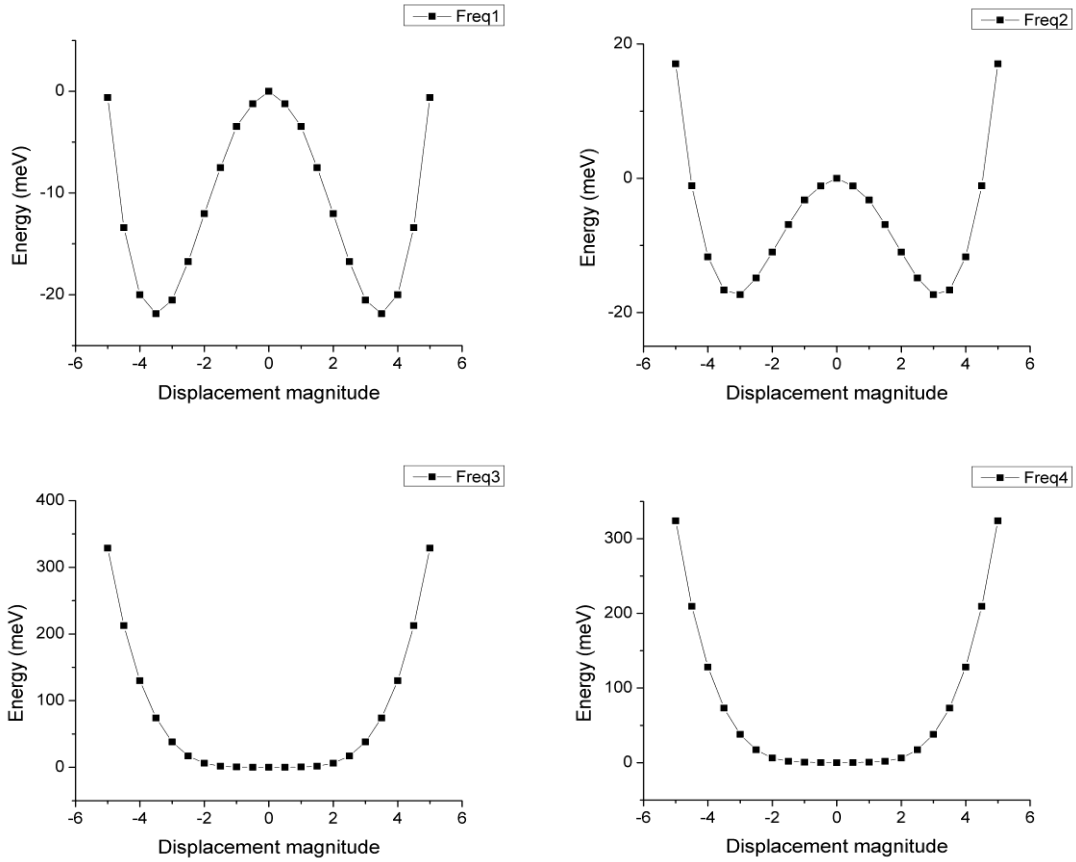

Figure 47. Energy profiles at increasing negative frequencies of M point (from top left to bottom right) with respect to displacement magnitude for fully distorted structure.

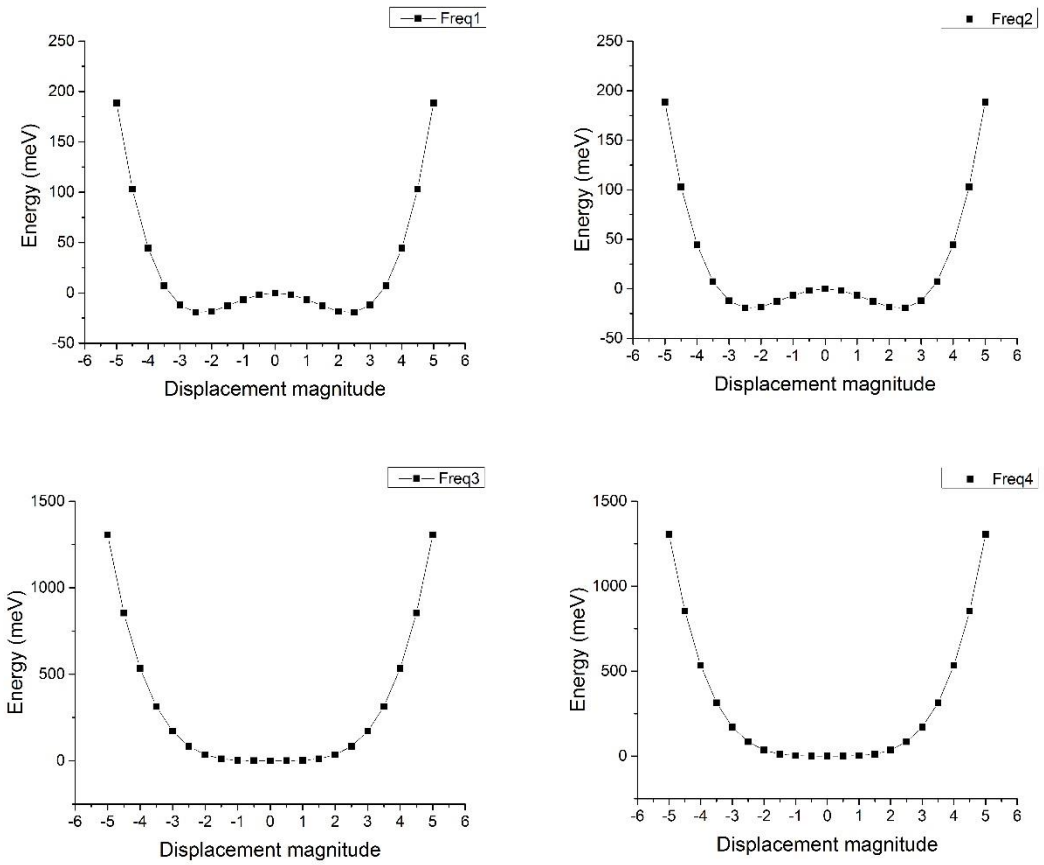

Figure 48. Energy profiles at increasing negative frequencies of L point (from top left to bottom right) with respect to displacement magnitude for fully distorted structure.

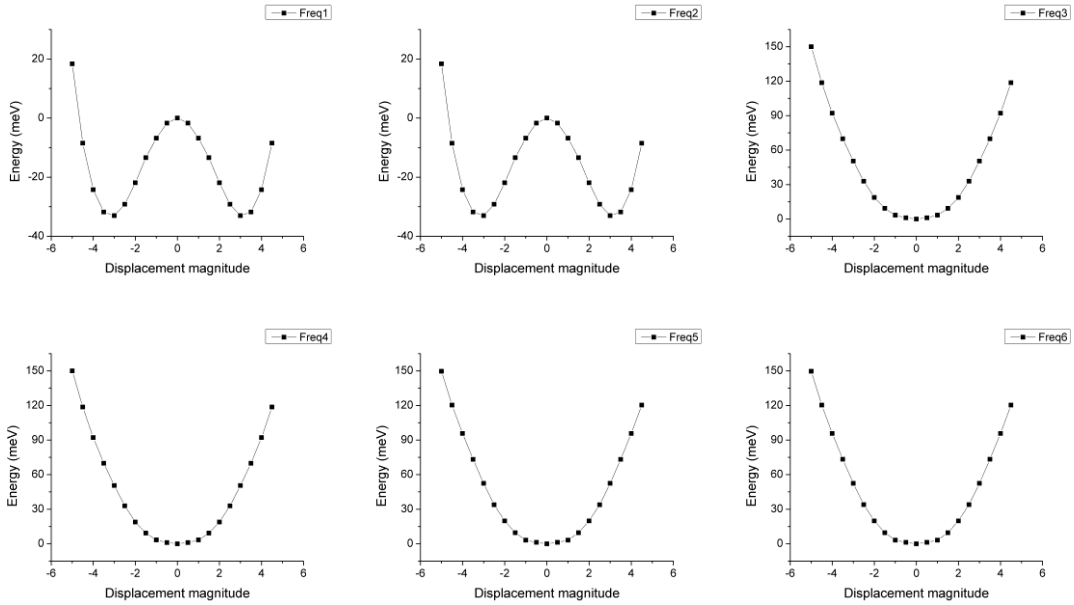

Figure 49. Energy profiles at increasing negative frequencies of A point (from top left to bottom right) with respect to displacement magnitude for fully distorted structure.

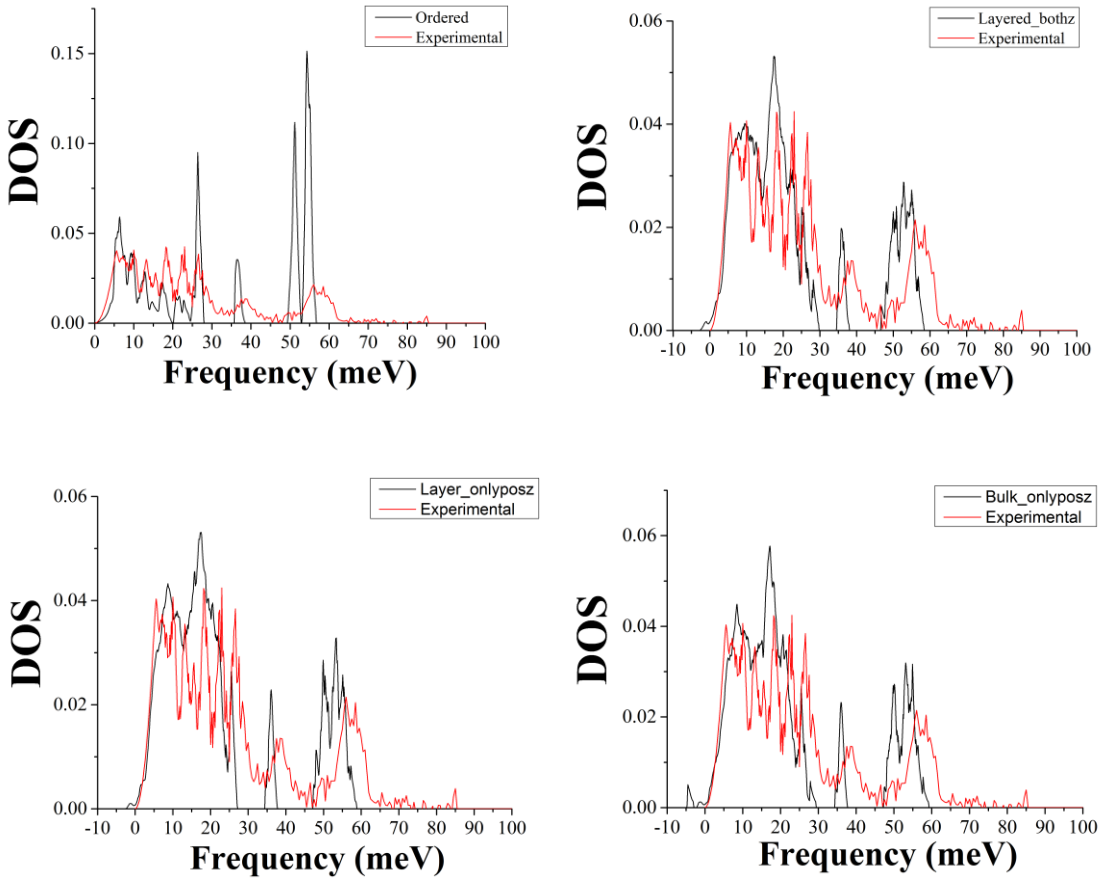

Figure 50. Full comparison of experimental and simulated DOS for ordered and disorder $CuInP_2Se_6$.

REFERENCES

1. R. Dawson, A. I. Cooper and D. J. Adams, *Progress in Polymer Science*, 2012, **37**, 530-563.

2. L. D. Gelb, *MRS Bulletin*, 2009, **34**, 592-601.

3. M. E. Davis, *Nature*, 2002, **417**, 813-821.

4. S. T. Meek, J. A. Greathouse and M. D. Allendorf, *Advanced Materials*, 2011, **23**, 249-267.

5. J.-R. Li, R. J. Kuppler and H.-C. Zhou, *Chemical Society reviews*, 2009, **38**, 1477-1504.

6. S. Keskin and S. Kizilel, *Industrial & Engineering Chemistry Research*, 2011, **50**, 1799-1812.

7. H.-C. Zhou, J. R. Long and O. M. Yaghi, *Chemical Reviews*, 2012, **112**, 673-674.

8. J.-R. Li, J. Sculley and H.-C. Zhou, *Chemical Reviews*, 2012, **112**, 869-932.

9. T. Watanabe and D. S. Sholl, *The Journal of chemical physics*, 2010, **133**, 094509.

10. N. L. Rosi, J. Kim, M. Eddaoudi, B. Chen, M. O'Keeffe and O. M. Yaghi, *Journal of the American Chemical Society*, 2005, **127**, 1504-1518.

11. J. R. Karra and K. S. Walton, *Langmuir*, 2008, **24**, 8620-8626.

12. G. Férey, C. Mellot-Draznieks, C. Serre, F. Millange, J. Dutour, S. Surblé and I. Margiolaki, *Science*, 2005, **309**, 2040-2042.

13. Y. Gurdal and S. Keskin, *Industrial & Engineering Chemistry Research*, 2012, **51**, 7373-7382.

14. S. L. James, *Chemical Society reviews*, 2003, **32**, 276-288.

15. A. Martin-Calvo, E. Garcia-Perez, J. Manuel Castillo and S. Calero, *Physical Chemistry Chemical Physics*, 2008, **10**, 7085-7091.

16. A. L. Dzubak, L.-C. Lin, J. Kim, J. A. Swisher, R. Poloni, S. N. Maximoff, B. Smit and L. Gagliardi, *Nature chemistry*, 2012, **4**, 810-816.

17. T. Duren, Y.-S. Bae and R. Q. Snurr, *Chemical Society reviews*, 2009, **38**, 1237-1247.

18. L. E. Kreno, K. Leong, O. K. Farha, M. Allendorf, R. P. Van Duyne and J. T. Hupp, *Chemical Reviews*, 2012, **112**, 1105-1125.

19. P. Horcajada, T. Chalati, C. Serre, B. Gillet, C. Sebrie, T. Baati, J. F. Eubank, D. Heurtaux, P. Clayette, C. Kreuz, J.-S. Chang, Y. K. Hwang, V. Marsaud, P.-N. Bories, L. Cynober, S. Gil, G. Ferey, P. Couvreur and R. Gref, *Nature Materials*, 2010, **9**, 172-178.

20. J. Lee, O. K. Farha, J. Roberts, K. A. Scheidt, S. T. Nguyen and J. T. Hupp, *Chemical Society reviews*, 2009, **38**, 1450-1459.

21. R. B. Getman, Y.-S. Bae, C. E. Wilmer and R. Q. Snurr, *Chemical Reviews*, 2012, **112**, 703-723.

22. K. Sumida, D. L. Rogow, J. A. Mason, T. M. McDonald, E. D. Bloch, Z. R. Herm, T.-H. Bae and J. R. Long, *Chemical Reviews*, 2012, **112**, 724-781.

23. M. P. Suh, H. J. Park, T. K. Prasad and D.-W. Lim, *Chemical Reviews*, 2012, **112**, 782-835.

24. H. Demir, J. A. Greathouse, C. L. Staiger, J. J. Perry IV, M. D. Allendorf and D. S. Sholl, *Journal of Materials Chemistry A*, 2015, **3**, 23539-23548.

25. J. J. Perry, S. L. Teich-McGoldrick, S. T. Meek, J. A. Greathouse, M. Haranczyk and M. D. Allendorf, *The Journal of Physical Chemistry C*, 2014, **118**, 11685-11698.

26. S. Nair, J. Gascon and Z. Lai, *Chemical Engineering Science*, 2015, **124**, 1-2.

27. C. E. Wilmer, M. Leaf, C. Y. Lee, O. K. Farha, B. G. Hauser, J. T. Hupp and R. Q. Snurr, *Nature chemistry*, 2012, **4**, 83-89.

28. F. Allen, *Acta Crystallographica Section B*, 2002, **58**, 380-388.

29. Y. G. Chung, J. Camp, M. Haranczyk, B. J. Sikora, W. Bury, V. Krungleviciute, T. Yildirim, O. K. Farha, D. S. Sholl and R. Q. Snurr, *Chemistry of Materials*, 2014, **26**, 6185-6192.

30. C. M. Simon, R. Mercado, S. K. Schnell, B. Smit and M. Haranczyk, *Chemistry of Materials*, 2015, **27**, 4459-4475.

31. Y. Basdogan, K. B. Sezginel and S. Keskin, *Industrial & Engineering Chemistry Research*, 2015, **54**, 8479-8491.

32. E. Haldoupis, S. Nair and D. S. Sholl, *Journal of the American Chemical Society*, 2010, **132**, 7528-7539.

33. T. Van Heest, S. L. Teich-McGoldrick, J. A. Greathouse, M. D. Allendorf and D. S. Sholl, *The Journal of Physical Chemistry C*, 2012, **116**, 13183-13195.

34. T. Saha-Dasgupta, *Journal of Physics: Condensed Matter*, 2014, **26**, 193201.

35. Y. U. Wang, *Journal of Materials Science*, 2009, **44**, 5225-5234.

36. M. Połomska, T. Pawłowski, A. Pietraszko and L. Kirpichnikova, *Journal of Molecular Structure*, 2004, **704**, 95-100.

37. S. M. Yang, J.-G. Yoon and T. W. Noh, *Current Applied Physics*, 2011, **11**, 1111-1125.

38. R. Raffaele, *Modelling and Simulation in Materials Science and Engineering*, 2003, **11**, R69.

39. H. J. Bakker, S. Hunsche and H. Kurz, *Reviews of Modern Physics*, 1998, **70**, 523-536.

40. T. Granzow, T. Woike, M. Wöhlecke, M. Imlau and W. Kleemann, *Physical Review Letters*, 2002, **89**, 127601.

41. S. Horiuchi and Y. Tokura, *Nature Materials*, 2008, **7**, 357-366.

42. L. Kantorovich, *Quantum Theory of the Solid State: An Introduction*, Springer Netherlands, 2004.

43. X. Hao, J. Zhai, L. B. Kong and Z. Xu, *Progress in Materials Science*, 2014, **63**, 1-57.

44. L. Jin, F. Li and S. Zhang, *Journal of the American Ceramic Society*, 2014, **97**, 1-27.

45. B.-H. Annette, *Journal of Physics: Condensed Matter*, 2012, **24**, 273202.

46. J. F. Scott, *Science*, 2007, **315**, 954-959.

47. N. Izyumskaya, Y. Alivov and H. Morkoç, *Critical Reviews in Solid State and Materials Sciences*, 2009, **34**, 89-179.

48. C. F. Pulvari, *Physical Review*, 1960, **120**, 1670-1673.

49. K. C. Kao, *Dielectric Phenomena in Solids*, Elsevier Science, 2004.

50. E. Sun and W. Cao, *Progress in Materials Science*, 2014, **65**, 124-210.

51. A. Roy, R. Prasad, S. Auluck and A. Garg, *Applied Physics Letters*, 2013, **102**, 182901.

52. V. Garcia and M. Bibes, *Nature Communications*, 2014, **5**.

53. V. Garcia and M. Bibes, *Nature*, 2012, **483**, 279-281.

54. M. Teresa Buscaglia, C. Harnagea, M. Dapiaggi, V. Buscaglia, A. Pignolet and P. Nanni, *Chemistry of Materials*, 2009, **21**, 5058-5065.

55. M. Dawber, K. M. Rabe and J. F. Scott, *Reviews of Modern Physics*, 2005, **77**, 1083-1130.

56. S.-E. Park and T. R. Shrout, *Journal of Applied Physics*, 1997, **82**, 1804-1811.

57. A. García and D. Vanderbilt, *Applied Physics Letters*, 1998, **72**, 2981-2983.

58. X. Tan, C. Ma, J. Frederick, S. Beckman and K. G. Webber, *Journal of the American Ceramic Society*, 2011, **94**, 4091-4107.

59. E. Sawaguchi, H. Maniwa and S. Hoshino, *Physical Review*, 1951, **83**, 1078-1078.

60. G. Shirane and R. Pepinsky, *Physical Review*, 1953, **91**, 812-815.

61. G. Shirane, R. Newnham and R. Pepinsky, *Physical Review*, 1954, **96**, 581-588.

62. G. A. Samara, *Physical Review Letters*, 1971, **27**, 103-106.

63. A. J. Cohen, P. Mori-Sánchez and W. Yang, *Science*, 2008, **321**, 792-794.

64. A. J. Cohen, P. Mori-Sánchez and W. Yang, *Chemical Reviews*, 2012, **112**, 289-320.

65. P. W. Atkins and R. S. Friedman, *Molecular quantum mechanics*, Oxford University Press, 1997.

66. D. A. McQuarrie, *Quantum chemistry*, University Science Books, 1983.

67. M. A. Ratner and G. C. Schatz, *Introduction to Quantum Mechanics in Chemistry*, Prentice Hall, 2001.

68. N. Argaman and G. Makov, *American Journal of Physics*, 2000, **68**, 69-79.

69. E. S. Kryachko and E. V. Ludeña, *Physics Reports*, 2014, **544**, 123-239.

70. E. Schrödinger, *Physical Review*, 1926, **28**, 1049-1070.

71. D. Sholl and J. A. Steckel, *Density Functional Theory: A Practical Introduction*, Wiley, 2009.

72. J. P. Perdew, J. A. Chevary, S. H. Vosko, K. A. Jackson, M. R. Pederson, D. J. Singh and C. Fiolhais, *Physical Review B*, 1992, **46**, 6671-6687.

73. J. P. Perdew, K. Burke and M. Ernzerhof, *Physical Review Letters*, 1996, **77**, 3865-3868.

74. S. Grimme, R. Huenerbein and S. Ehrlich, *Chemphyschem*, 2011, **12**, 1258-1261.

75. M. K. Rana, H. S. Koh, J. Hwang and D. J. Siegel, *The Journal of Physical Chemistry C*, 2012, **116**, 16957-16968.

76. S. Grimme, *Journal of computational chemistry*, 2006, **27**, 1787-1799.

77. M. Dion, H. Rydberg, E. Schröder, D. C. Langreth and B. I. Lundqvist, *Physical Review Letters*, 2004, **92**, 246401.

78. K. Lee, É. D. Murray, L. Kong, B. I. Lundqvist and D. C. Langreth, *Physical Review B*, 2010, **82**, 081101.

79. Y. Zhang and W. Yang, *Physical Review Letters*, 1998, **80**, 890-890.

80. J. P. Perdew and W. Yue, *Physical Review B*, 1986, **33**, 8800-8802.

81. É. D. Murray, K. Lee and D. C. Langreth, *Journal of Chemical Theory and Computation*, 2009, **5**, 2754-2762.

82. Y. Liu, J. Zhao, F. Li and Z. Chen, *Journal of computational chemistry*, 2013, **34**, 121-131.

83. Y. Zhao and D. G. Truhlar, *Theoretical Chemistry Accounts*, 2007, **120**, 215-241.

84. G. Kresse and J. Furthmüller, *Physical Review B*, 1996, **54**, 11169-11186.

85. G. Kresse and J. Furthmüller, *Computational Materials Science*, 1996, **6**, 15-50.

86. G. Kresse and J. Hafner, *Physical Review B*, 1993, **47**, 558-561.

87. P. E. Blöchl, *Physical Review B*, 1994, **50**, 17953-17979.

88. G. Kresse and D. Joubert, *Physical Review B*, 1999, **59**, 1758-1775.

89. Gaussian 09, Revision E.01, M. J. Frisch, G. W. Trucks, H. B. Schlegel, G. E. Scuseria, M. A. Robb, J. R. Cheeseman, G. Scalmani, V. Barone, B. Mennucci, G. A. Petersson, H. Nakatsuji, M. Caricato, X. Li, H. P. Hratchian, A. F. Izmaylov, J. Bloino, G. Zheng, J. L. Sonnenberg, M. Hada, M. Ehara, K. Toyota, R. Fukuda, J. Hasegawa, M. Ishida, T. Nakajima, Y. Honda, O. Kitao, H. Nakai, T. Vreven, J. A. Montgomery Jr., J. E. Peralta, F. Ogliaro, M. J. Bearpark, J. Heyd, E. N. Brothers, K. N. Kudin, V. N. Staroverov, R. Kobayashi, J. Normand, K. Raghavachari, A. P. Rendell, J. C. Burant, S. S. Iyengar, J. Tomasi, M. Cossi, N. Rega, N. J. Millam, M. Klene, J. E. Knox, J. B. Cross, V. Bakken, C. Adamo, J. Jaramillo, R. Gomperts, R. E. Stratmann, O. Yazyev, A. J. Austin, R. Cammi, C. Pomelli, J. W. Ochterski, R. L. Martin, K. Morokuma, V. G. Zakrzewski, G. A. Voth, P. Salvador, J. J. Dannenberg, S. Dapprich, A. D. Daniels, Ö. Farkas, J. B. Foresman, J. V. Ortiz, J. Cioslowski and D. J. Fox, Gaussian, Inc., Wallingford CT, 2009.

90. C. Møller and M. S. Plesset, *Physical Review*, 1934, **46**, 618-622.

91. A. Tkatchenko, R. A. DiStasio, M. Head-Gordon and M. Scheffler, *The Journal of chemical physics*, 2009, **131**, 094106.

92. S. Grimme, *The Journal of chemical physics*, 2003, **118**, 9095-9102.

93. S. M. Cybulski and M. L. Lytle, *The Journal of chemical physics*, 2007, **127**, 141102.

94. D. Cremer, *Wiley Interdisciplinary Reviews: Computational Molecular Science*, 2011, **1**, 509-530.

95. M. Häser, *Theoretica chimica acta*, **87**, 147-173.

96. A. H. Fuchs and A. K. Cheetham, *The Journal of Physical Chemistry B*, 2001, **105**, 7375-7383.

97. J. J. Potoff and J. I. Siepmann, *AIChE Journal*, 2001, **47**, 1676-1682.

98. D. Frenkel and B. Smit, *Understanding Molecular Simulation: From Algorithms to Applications*, Academic Press, San Diego, Second edn., 2002.

99. E. Kaxiras, *Atomic and Electronic Structure of Solids*, Cambridge University Press, 2003.

100. S. Sircar, *Industrial & Engineering Chemistry Research*, 2006, **45**, 5435-5448.

101. S. Keskin, *The Journal of Physical Chemistry C*, 2012, **116**, 1772-1779.

102. B. Liu and B. Smit, *Langmuir*, 2009, **25**, 5918-5926.

103. Q. Yang, L. Ma, C. Zhong, X. An and D. Liu, *The Journal of Physical Chemistry C*, 2011, **115**, 2790-2797.

104. M. Xue, Z. Zhang, S. Xiang, Z. Jin, C. Liang, G.-S. Zhu, S.-L. Qiu and B. Chen, *Journal of Materials Chemistry*, 2010, **20**, 3984-3988.

105. B. Mu, F. Li and K. S. Walton, *Chemical communications*, 2009, DOI: 10.1039/B819828D, 2493-2495.

106. E. Atci, I. Erucar and S. Keskin, *The Journal of Physical Chemistry C*, 2011, **115**, 6833-6840.

107. C. A. Fernandez, J. Liu, P. K. Thallapally and D. M. Strachan, *Journal of the American Chemical Society*, 2012, **134**, 9046-9049.

108. S. T. Meek, S. L. Teich-McGoldrick, J. J. Perry, J. A. Greathouse and M. D. Allendorf, *The Journal of Physical Chemistry C*, 2012, **116**, 19765-19772.

109. Y. Gurdal and S. Keskin, *The Journal of Physical Chemistry C*, 2013, **117**, 5229-5241.

110. P. K. Thallapally, J. W. Grate and R. K. Motkuri, *Chemical communications*, 2012, **48**, 347-349.

111. J. Liu, P. K. Thallapally and D. Strachan, *Langmuir*, 2012, **28**, 11584-11589.

112. U. Mueller, M. Schubert, F. Teich, H. Puetter, K. Schierle-Arndt and J. Pastre, *Journal of Materials Chemistry*, 2006, **16**, 626-636.

113. A. Soleimani Dorcheh, D. Denysenko, D. Volkmer, W. Donner and M. Hirscher, *Microporous and Mesoporous Materials*, 2012, **162**, 64-68.

114. S. Pawsey, I. Moudrakovski, J. Ripmeester, L.-Q. Wang, G. J. Exarhos, J. L. C. Rowsell and O. M. Yaghi, *The Journal of Physical Chemistry C*, 2007, **111**, 6060-6067.

115. J. A. Greathouse, T. L. Kinnibrugh and M. D. Allendorf, *Industrial & Engineering Chemistry Research*, 2009, **48**, 3425-3431.

116. D. Dubbeldam, H. Frost, K. S. Walton and R. Q. Snurr, *Fluid Phase Equilibria*, 2007, **261**, 152-161.

117. P. Ryan, O. K. Farha, L. J. Broadbelt and R. Q. Snurr, *AIChE Journal*, 2011, **57**, 1759-1766.

118. B. J. Sikora, C. E. Wilmer, M. L. Greenfield and R. Q. Snurr, *Chemical Science*, 2012, **3**, 2217-2223.

119. G. Maurin, R. Bell, B. Kuchta, T. Poyet and P. Llewellyn, *Adsorption*, 2005, **11**, 331-336.

120. G. Maurin, P. L. Llewellyn, T. Poyet and B. Kuchta, *Microporous and Mesoporous Materials*, 2005, **79**, 53-59.

121. J. Cirera, J. C. Sung, P. B. Howland and F. Paesani, *The Journal of chemical physics*, 2012, **137**, 054704.

122. J. G. McDaniel, K. Yu and J. R. Schmidt, *The Journal of Physical Chemistry C*, 2011, **116**, 1892-1903.

123. A. K. Rappe, C. J. Casewit, K. S. Colwell, W. A. Goddard and W. M. Skiff, *Journal of the American Chemical Society*, 1992, **114**, 10024-10035.

124. S. L. Mayo, B. D. Olafson and W. A. Goddard, *The Journal of Physical Chemistry*, 1990, **94**, 8897-8909.

125. W. L. Jorgensen, D. S. Maxwell and J. Tirado-Rives, *Journal of the American Chemical Society*, 1996, **118**, 11225-11236.

126. D. Fairen-Jimenez, R. Galvelis, A. Torrisi, A. D. Gellan, M. T. Wharmby, P. A. Wright, C. Mellot-Draznieks and T. Duren, *Dalton Transactions*, 2012, **41**, 10752-10762.

127. J. Pérez-Pellitero, H. Amrouche, F. R. Siperstein, G. Pirngruber, C. Nieto-Draghi, G. Chaplais, A. Simon-Masseron, D. Bazer-Bachi, D. Peralta and N. Bats, *Chemistry – A European Journal*, 2010, **16**, 1560-1571.

128. W. Li, J. Zhang, H. Guo and G. Gahungu, *The Journal of Physical Chemistry C*, 2011, **115**, 4935-4942.

129. H. Fang, H. Demir, P. Kamakoti and D. S. Sholl, *Journal of Materials Chemistry A*, 2014, **2**, 274-291.

130. A. R. Kulkarni and D. S. Sholl, *Langmuir*, 2015, **31**, 8453-8468.

131. J. A. Gee and D. S. Sholl, *The Journal of Physical Chemistry C*, 2015, **119**, 16920-16926.

132. E. Haldoupis, J. Borycz, H. Shi, K. D. Vogiatzis, P. Bai, W. L. Queen, L. Gagliardi and J. I. Siepmann, *The Journal of Physical Chemistry C*, 2015, **119**, 16058-16071.

133. J. Kim, L.-C. Lin, K. Lee, J. B. Neaton and B. Smit, *The Journal of Physical Chemistry C*, 2014, **118**, 2693-2701.

134. M. Prakash, N. Sakhavand and R. Shahsavari, *The Journal of Physical Chemistry C*, 2013, **117**, 24407-24416.

135. R. Poloni, B. Smit and J. B. Neaton, *The Journal of Physical Chemistry A*, 2012, **116**, 4957-4964.

136. H. Fang, P. Kamakoti, J. Zang, S. Cundy, C. Paur, P. I. Ravikovitch and D. S. Sholl, *The Journal of Physical Chemistry C*, 2012, **116**, 10692-10701.

137. T. A. Manz and D. S. Sholl, *Journal of Chemical Theory and Computation*, 2010, **6**, 2455-2468.

138. T. A. Manz and D. S. Sholl, *Journal of Chemical Theory and Computation*, 2011, **7**, 4146-4164.

139. T. A. Manz and D. S. Sholl, *Journal of Chemical Theory and Computation*, 2012, **8**, 2844-2867.

140. A. Gupta, S. Chempath, M. J. Sanborn, L. A. Clark and R. Q. Snurr, *Molecular Simulation*, 2003, **29**, 29-46.

141. S. P. Ong, W. D. Richards, A. Jain, G. Hautier, M. Kocher, S. Cholia, D. Gunter, V. L. Chevrier, K. A. Persson and G. Ceder, *Computational Materials Science*, 2013, **68**, 314-319.

142. D. Dubbeldam, S. Calero, D. E. Ellis and R. Q. Snurr, RASPA 1.0, Northwestern University, Evanston, IL, 2008.

143. T. Düren, F. Millange, G. Férey, K. S. Walton and R. Q. Snurr, *The Journal of Physical Chemistry C*, 2007, **111**, 15350-15356.

144. M. V. Parkes, C. L. Staiger, J. J. Perry Iv, M. D. Allendorf and J. A. Greathouse, *Physical Chemistry Chemical Physics*, 2013, **15**, 9093-9106.

145. N. de Nevers, *Physical and Chemical Equilibrium for Chemical Engineers*, Wiley, 2012.

146. S. Surblé, F. Millange, C. Serre, T. Düren, M. Latroche, S. Bourrelly, P. L. Llewellyn and G. Férey, *Journal of the American Chemical Society*, 2006, **128**, 14889-14896.

147. J. Zang, S. Nair and D. S. Sholl, *The Journal of Physical Chemistry C*, 2013, **117**, 7519-7525.

148. M. K. Rana, H. S. Koh, H. Zuberi and D. J. Siegel, *The Journal of Physical Chemistry C*, 2014, **118**, 2929-2942.

149. J. Getzschmann, I. Senkovska, D. Wallacher, M. Tovar, D. Fairen-Jimenez, T. Düren, J. M. van Baten, R. Krishna and S. Kaskel, *Microporous and Mesoporous Materials*, 2010, **136**, 50-58.

150. H. S. Koh, M. K. Rana, A. G. Wong-Foy and D. J. Siegel, *The Journal of Physical Chemistry C*, 2015, **119**, 13451-13458.

151. Z. Hulvey, K. V. Lawler, Z. Qiao, J. Zhou, D. Fairen-Jimenez, R. Q. Snurr, S. V. Ushakov, A. Navrotsky, C. M. Brown and P. M. Forster, *The Journal of Physical Chemistry C*, 2013, **117**, 20116-20126.

152. L. Chen, L. Grajciar, P. Nachtigall and T. Düren, *The Journal of Physical Chemistry C*, 2011, **115**, 23074-23080.

153. A. M. Ebrahim and T. J. Bandosz, *ACS Applied Materials & Interfaces*, 2013, **5**, 10565-10573.

154. P. Ghosh, K. C. Kim and R. Q. Snurr, *The Journal of Physical Chemistry C*, 2014, **118**, 1102-1110.

155. G. W. Peterson, G. W. Wagner, A. Balboa, J. Mahle, T. Sewell and C. J. Karwacki, *The Journal of Physical Chemistry C*, 2009, **113**, 13906-13917.

156. P. Z. Moghadam, P. Ghosh and R. Q. Snurr, *The Journal of Physical Chemistry C*, 2015, **119**, 3163-3170.

157. K. C. Kim, D. Yu and R. Q. Snurr, *Langmuir*, 2013, **29**, 1446-1456.

158. L. Shen, S. Liang, W. Wu, R. Liang and L. Wu, *Journal of Materials Chemistry A*, 2013, **1**, 11473-11482.

159. S. Biswas and P. Van Der Voort, *European Journal of Inorganic Chemistry*, 2013, **2013**, 2154-2160.

160. B. Zheng, J. Bai, J. Duan, L. Wojtas and M. J. Zaworotko, *Journal of the American Chemical Society*, 2011, **133**, 748-751.

161. Y. Zhao, H. Wu, T. J. Emge, Q. Gong, N. Nijem, Y. J. Chabal, L. Kong, D. C. Langreth, H. Liu, H. Zeng and J. Li, *Chemistry – A European Journal*, 2011, **17**, 5101-5109.

162. I. Spanopoulos, P. Xydias, C. D. Malliakas and P. N. Trikalitis, *Inorganic Chemistry*, 2013, **52**, 855-862.

163. M. Kandiah, M. H. Nilsen, S. Usseglio, S. Jakobsen, U. Olsbye, M. Tilset, C. Larabi, E. A. Quadrelli, F. Bonino and K. P. Lillerud, *Chemistry of Materials*, 2010, **22**, 6632-6640.

164. L.-M. Yang, E. Ganz, S. Svelle and M. Tilset, *Journal of Materials Chemistry C*, 2014, **2**, 7111-7125.

165. J. B. DeCoste, G. W. Peterson, H. Jasuja, T. G. Glover, Y.-g. Huang and K. S. Walton, *Journal of Materials Chemistry A*, 2013, **1**, 5642-5650.

166. G. W. Peterson, J. B. DeCoste, T. G. Glover, Y. Huang, H. Jasuja and K. S. Walton, *Microporous and Mesoporous Materials*, 2013, **179**, 48-53.

167. A. D. Wiersum, E. Soubeyrand-Lenoir, Q. Yang, B. Moulin, V. Guillerm, M. B. Yahia, S. Bourrelly, A. Vimont, S. Miller, C. Vagner, M. Daturi, G. Clet, C. Serre, G. Maurin and P. L. Llewellyn, *Chemistry – An Asian Journal*, 2011, **6**, 3270-3280.

168. Q. Yang, A. D. Wiersum, H. Jobic, V. Guillerm, C. Serre, P. L. Llewellyn and G. Maurin, *The Journal of Physical Chemistry C*, 2011, **115**, 13768-13774.

169. Q. Yang, V. Guillerm, F. Ragon, A. D. Wiersum, P. L. Llewellyn, C. Zhong, T. Devic, C. Serre and G. Maurin, *Chemical communications*, 2012, **48**, 9831-9833.

170. B. Bozbiyik, T. Duerinck, J. Lannoeye, D. E. De Vos, G. V. Baron and J. F. M. Denayer, *Microporous and Mesoporous Materials*, 2014, **183**, 143-149.

171. J. H. Cavka, S. Jakobsen, U. Olsbye, N. Guillou, C. Lamberti, S. Bordiga and K. P. Lillerud, *Journal of the American Chemical Society*, 2008, **130**, 13850-13851.

172. H. Wu, T. Yildirim and W. Zhou, *The Journal of Physical Chemistry Letters*, 2013, **4**, 925-930.

173. L. Valenzano, B. Civalleri, S. Chavan, S. Bordiga, M. H. Nilsen, S. Jakobsen, K. P. Lillerud and C. Lamberti, *Chemistry of Materials*, 2011, **23**, 1700-1718.

174. W. Liang, R. Babarao and D. M. D'Alessandro, *Inorganic Chemistry*, 2013, **52**, 12878-12880.

175. P. Deria, Y. G. Chung, R. Q. Snurr, J. T. Hupp and O. K. Farha, *Chemical Science*, 2015, **6**, 5172-5176.

176. Q. Zhao, W. Yuan, J. Liang and J. Li, *International Journal of Hydrogen Energy*, 2013, **38**, 13104-13109.

177. D. Sun, Y. Fu, W. Liu, L. Ye, D. Wang, L. Yang, X. Fu and Z. Li, *Chemistry – A European Journal*, 2013, **19**, 14279-14285.

178. J. B. DeCoste, T. J. Demasky, M. J. Katz, O. K. Farha and J. T. Hupp, *New Journal of Chemistry*, 2015, **39**, 2396-2399.

179. Y. Wu, H. Chen, D. Liu, J. Xiao, Y. Qian and H. Xi, *ACS Applied Materials & Interfaces*, 2015, **7**, 5775-5787.

180. S.-I. Kim, T.-U. Yoon, M.-B. Kim, S.-J. Lee, Y. K. Hwang, J.-S. Chang, H.-J. Kim, H.-N. Lee, U. H. Lee and Y.-S. Bae, *Chemical Engineering Journal*, 2016, **286**, 467-475.

181. Z. Hu and D. Zhao, *Dalton Transactions*, 2015, **44**, 19018-19040.

182. J. H. Cavka, C. A. Grande, G. Mondino and R. Blom, *Industrial & Engineering Chemistry Research*, 2014, **53**, 15500-15507.

183. M. Kim and S. M. Cohen, *CrystEngComm*, 2012, **14**, 4096-4104.

184. M. J. Katz, Z. J. Brown, Y. J. Colon, P. W. Siu, K. A. Scheidt, R. Q. Snurr, J. T. Hupp and O. K. Farha, *Chemical communications*, 2013, **49**, 9449-9451.

185. C. Zlotea, D. Phanon, M. Mazaj, D. Heurtaux, V. Guillerm, C. Serre, P. Horcajada, T. Devic, E. Magnier, F. Cuevas, G. Ferey, P. L. Llewellyn and M. Latroche, *Dalton Transactions*, 2011, **40**, 4879-4881.

186. W. Morris, C. J. Doonan and O. M. Yaghi, *Inorganic Chemistry*, 2011, **50**, 6853-6855.

187. M. Kim, J. F. Cahill, Y. Su, K. A. Prather and S. M. Cohen, *Chemical Science*, 2012, **3**, 126-130.

188. M. Lin Foo, S. Horike, T. Fukushima, Y. Hijikata, Y. Kubota, M. Takata and S. Kitagawa, *Dalton Transactions*, 2012, **41**, 13791-13794.

189. S. J. Garibay and S. M. Cohen, *Chemical communications*, 2010, **46**, 7700-7702.

190. T. Duerinck, R. Bueno-Perez, F. Vermoortele, D. E. De Vos, S. Calero, G. V. Baron and J. F. M. Denayer, *The Journal of Physical Chemistry C*, 2013, **117**, 12567-12578.

191. K.-Y. A. Lin, Y.-T. Liu and S.-Y. Chen, *Journal of colloid and interface science*, 2016, **461**, 79-87.

192. F. Yang, H. Huang, X. Wang, F. Li, Y. Gong, C. Zhong and J.-R. Li, *Crystal Growth & Design*, 2015, **15**, 5827-5833.

193. K. Hendrickx, D. E. P. Vanpoucke, K. Leus, K. Lejaeghere, A. Van Yperen-De Deyne, V. Van Speybroeck, P. Van Der Voort and K. Hemelsoet, *Inorganic Chemistry*, 2015, **54**, 10701-10710.

194. L. Shen, R. Liang, M. Luo, F. Jing and L. Wu, *Physical Chemistry Chemical Physics*, 2015, **17**, 117-121.

195. Q. Yang, S. Vaesen, F. Ragon, A. D. Wiersum, D. Wu, A. Lago, T. Devic, C. Martineau, F. Taulelle, P. L. Llewellyn, H. Jobic, C. Zhong, C. Serre, G. De Weireld and G. Maurin, *Angewandte Chemie International Edition*, 2013, **52**, 10316-10320.

196. D. Cunha, C. Gaudin, I. Colinet, P. Horcajada, G. Maurin and C. Serre, *Journal of Materials Chemistry B*, 2013, **1**, 1101-1108.

197. S. Devautour-Vinot, C. Martineau, S. Diaby, M. Ben-Yahia, S. Miller, C. Serre, P. Horcajada, D. Cunha, F. Taulelle and G. Maurin, *The Journal of Physical Chemistry C*, 2013, **117**, 11694-11704.

198. H. Jasuja, G. W. Peterson, J. B. Decoste, M. A. Browe and K. S. Walton, *Chemical Engineering Science*, 2015, **124**, 118-124.

199. G. E. Cmarik, M. Kim, S. M. Cohen and K. S. Walton, *Langmuir*, 2012, **28**, 15606-15613.

200. Z. Hu, Y. Peng, Z. Kang, Y. Qian and D. Zhao, *Inorganic Chemistry*, 2015, **54**, 4862-4868.

201. O. G. Nik, X. Y. Chen and S. Kaliaguine, *Journal of Membrane Science*, 2012, **413–414**, 48-61.

202. Y. Huang, W. Qin, Z. Li and Y. Li, *Dalton Transactions*, 2012, **41**, 9283-9285.

203. H. Jasuja, J. Zang, D. S. Sholl and K. S. Walton, *The Journal of Physical Chemistry C*, 2012, **116**, 23526-23532.

204. H. Jasuja and K. S. Walton, *The Journal of Physical Chemistry C*, 2013, **117**, 7062-7068.

205. P. M. Schoenecker, C. G. Carson, H. Jasuja, C. J. J. Flemming and K. S. Walton, *Industrial & Engineering Chemistry Research*, 2012, **51**, 6513-6519.

206. D. Yu, P. Ghosh and R. Q. Snurr, *Dalton Transactions*, 2012, **41**, 3962-3973.

207. J. G. McDaniel and J. R. Schmidt, *The Journal of Physical Chemistry A*, 2013, **117**, 2053-2066.

208. J. G. McDaniel, K. Yu and J. R. Schmidt, *The Journal of Physical Chemistry C*, 2012, **116**, 1892-1903.

209. J. G. McDaniel and J. R. Schmidt, *The Journal of Physical Chemistry C*, 2012, **116**, 14031-14039.

210. A. T. Hagler, *Journal of Chemical Theory and Computation*, 2015, **11**, 5555-5572.

211. S. F. Boys and F. Bernardi, *Molecular Physics*, 2002, **100**, 65-73.

212. F. Vermoortele, R. Ameloot, A. Vimont, C. Serre and D. De Vos, *Chemical communications*, 2011, **47**, 1521-1523.

213. F. Jeremias, V. Lozan, S. K. Henninger and C. Janiak, *Dalton Transactions*, 2013, **42**, 15967-15973.

214. K. S. Walton and D. S. Sholl, *AIChE Journal*, 2015, **61**, 2757-2762.

215. A. R. Kulkarni and D. S. Sholl, *Industrial & Engineering Chemistry Research*, 2012, **51**, 8631-8645.

216. S. A. Didas, A. R. Kulkarni, D. S. Sholl and C. W. Jones, *ChemSusChem*, 2012, **5**, 2058-2064.

217. G. W. Peterson, J. B. DeCoste, F. Fatollahi-Fard and D. K. Britt, *Industrial & Engineering Chemistry Research*, 2014, **53**, 701-707.

218. T. F. Willems, C. H. Rycroft, M. Kazi, J. C. Meza and M. Haranczyk, *Microporous and Mesoporous Materials*, 2012, **149**, 134-141.

219. R. J. Verploegh, S. Nair and D. S. Sholl, *Journal of the American Chemical Society*, 2015, **137**, 15760-15771.

220. E. Haldoupis, T. Watanabe, S. Nair and D. S. Sholl, *Chemphyschem*, 2012, **13**, 3449-3452.

221. Y. M. Vysochanskii, V. A. Stephanovich, A. A. Molnar, V. B. Cajipe and X. Bourdon, *Physical Review B*, 1998, **58**, 9119-9124.

222. R. Brec, *Solid State Ionics*, 1986, **22**, 3-30.

223. X. Bourdon, V. Maisonneuve, V. B. Cajipe, C. Payen and J. E. Fischer, *Journal of Alloys and Compounds*, 1999, **283**, 122-127.

224. R. Pfeiff and R. Kniep, *Journal of Alloys and Compounds*, 1992, **186**, 111-133.

225. M. A. Gave, D. Bilc, S. D. Mahanti, J. D. Breshears and M. G. Kanatzidis, *Inorganic Chemistry*, 2005, **44**, 5293-5303.

226. M. A. Susner, A. Belianinov, A. Borisevich, Q. He, M. Chyasnavichyus, H. Demir, D. S. Sholl, P. Ganesh, D. L. Abernathy, M. A. McGuire and P. Maksymovych, *ACS Nano*, 2015, **9**, 12365-12373.

227. A. Belianinov, Q. He, A. Dziaugys, P. Maksymovych, E. Eliseev, A. Borisevich, A. Morozovska, J. Banys, Y. Vysochanskii and S. V. Kalinin, *Nano Letters*, 2015, **15**, 3808-3814.

228. A. Grzechnik, V. B. Cajipe, C. Payen and P. F. McMillan, *Solid State Communications*, 1998, **108**, 43-47.

229. V. Maisonneuve, V. B. Cajipe, A. Simon, R. Von Der Muhll and J. Ravez, *Physical Review B*, 1997, **56**, 10860-10868.

230. Y. Fagot-Revurat, X. Bourdon, F. Bertran, V. B. Cajipe and D. Malterre, *Journal of Physics: Condensed Matter*, 2003, **15**, 595.

231. J. Macutkevic, J. Banys and Y. Vysochanskii, *Physica Status Solidi A*, 2009, **206**, 167-172.

232. X. Bourdon, A. R. Grimmer and V. B. Cajipe, *Chemistry of Materials*, 1999, **11**, 2680-2686.

233. J. Macutkevic, J. Banys, R. Grigalaitis and Y. Vysochanskii, *Physical Review B*, 2008, **78**, 064101.

234. A. Simon, J. Ravez, V. Maisonneuve, C. Payen and V. B. Cajipe, *Chemistry of Materials*, 1994, **6**, 1575-1580.

235. V. Maisonneuve, M. Evain, C. Payen, V. B. Cajipe and P. Molinié, *Journal of Alloys and Compounds*, 1995, **218**, 157-164.

236. P. Colombet, A. Leblanc, M. Danot and J. Rouxel, *Journal of Solid State Chemistry*, 1982, **41**, 174-184.

237. E. Durand, G. Ouvrard, M. Evain and R. Brec, *Inorganic Chemistry*, 1990, **29**, 4916-4920.

238. S. Lee, P. Colombet, G. Ouvrard and R. Brec, *Inorganic Chemistry*, 1988, **27**, 1291-1294.

239. F. Boucher, M. Evain and R. Brec, *Journal of Alloys and Compounds*, 1994, **215**, 63-70.

240. F. Boucher, M. Evain and R. Brec, *Acta Crystallographica Section B*, 1995, **51**, 952-961.

241. Y. M. Vysochanskii, A. A. Molnar, V. A. Stephanovich, V. B. Cajipe and X. Bourdon, *Ferroelectrics*, 1999, **226**, 243-261.

242. Y. M. Vysochanskii, A. A. Molnar, M. I. Gurzan, V. B. Cajipe and X. Bourdon, *Solid State Communications*, 2000, **115**, 13-17.

243. W. Kleemann, V. V. Shvartsman, P. Borisov, J. Banys and Y. M. Vysochanskii, *Physical Review B*, 2011, **84**, 094411.

244. A. Dziaugys, V. V. Shvartsman, J. Macutkevic, J. Banys, Y. Vysochanskii and W. Kleemann, *Physical Review B*, 2012, **85**, 134105.

245. M. M. Maior, V. T. Vrabel, I. P. Prits, N. F. Korda, M. I. Gurzan and Y. M. Vysochanskii, *Physics of the Solid State*, 2005, **47**, 1734-1739.

246. A. Togo and I. Tanaka, *Scripta Materialia*, 2015, **108**, 1-5.

247. R. M. Pick, M. H. Cohen and R. M. Martin, *Physical Review B*, 1970, **1**, 910-920.

248. X. Gonze and C. Lee, *Physical Review B*, 1997, **55**, 10355-10368.

249. R. D. King-Smith and D. Vanderbilt, *Physical Review B*, 1993, **47**, 1651-1654.

250. D. Vanderbilt and R. D. King-Smith, *Physical Review B*, 1993, **48**, 4442-4455.

251. T. Yoshimasa, S. Kazunori and K.-Y. Hiroshi, *Applied Physics Express*, 2010, **3**, 101201.

252. W. Tang, E. Sanville and G. Henkelman, *Journal of Physics: Condensed Matter*, 2009, **21**, 084204.

253. E. Sanville, S. D. Kenny, R. Smith and G. Henkelman, *Journal of computational chemistry*, 2007, **28**, 899-908.

254. M. P. Allen and D. J. Tildesley, *Computer simulation of liquids*, Clarendon Press, 1989.

255. D. L. Abernathy, M. B. Stone, M. J. Loguillo, M. S. Lucas, O. Delaire, X. Tang, J. Y. Y. Lin and B. Fultz, *Review of Scientific Instruments*, 2012, **83**, 015114.

256. A. Dhakshinamoorthy, M. Alvaro and H. Garcia, *Chemical communications*, 2012, **48**, 11275-11288.

257. A. Ö. Yazaydın, R. Q. Snurr, T.-H. Park, K. Koh, J. Liu, M. D. LeVan, A. I. Benin, P. Jakubczak, M. Lanuza, D. B. Galloway, J. J. Low and R. R. Willis, *Journal of the American Chemical Society*, 2009, **131**, 18198-18199.

258. A. Mallick, S. Saha, P. Pachfule, S. Roy and R. Banerjee, *Journal of Materials Chemistry*, 2010, **20**, 9073-9080.

259. D. Dubbeldam, K. S. Walton, D. E. Ellis and R. Q. Snurr, *Angewandte Chemie International Edition*, 2007, **46**, 4496-4499.

260. O. Bludský, M. Rubeš, P. Soldán and P. Nachtigall, *The Journal of chemical physics*, 2008, **128**, 114102.

261. M. Rubeš, P. Nachtigall, J. Vondrášek and O. Bludský, *The Journal of Physical Chemistry C*, 2009, **113**, 8412-8419.

262. H. Fang, P. Kamakoti, P. I. Ravikovitch, M. Aronson, C. Paur and D. S. Sholl, *Physical Chemistry Chemical Physics*, 2013, **15**, 12882-12894.

263. C. Serre, F. Millange, C. Thouvenot, M. Noguès, G. Marsolier, D. Louër and G. Férey, *Journal of the American Chemical Society*, 2002, **124**, 13519-13526.

264. R. V. Awati, P. I. Ravikovitch and D. S. Sholl, *The Journal of Physical Chemistry C*, 2013, **117**, 13462-13473.